Photoionization Studies of Highly Excited States of Zinc

By

Ghulam Aisha

(27-FBAS/PHDPHY/S14)

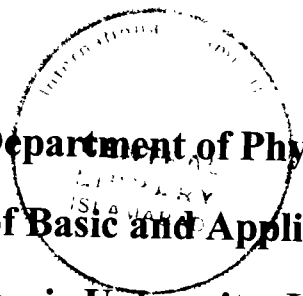

Department of Physics

Faculty of Basic and Applied Sciences

International Islamic University, Islamabad Pakistan

(2020)

Electron impact ionisation.

Rydberg states of Zinc.

Oscillator strengths.

Photoionization Studies of Highly Excited States of Zinc

By

Ghulam Aisha

(27-FBAS/PHDPHY/S14)

Supervisor:
Dr. Shaista Shahzada
Chairperson,
Associate Professor,
Department of Physics, FBAS, IIUI

Co-Supervisor:
Dr. Ali Nadeem
Deputy Chief Scientist,
National Institute of Laser and Optronics College,
Pakistan Institute of Engineering and Applied Sciences

Department of Physics

Faculty of Basic and Applied Sciences

International Islamic University, Islamabad Pakistan

(2020)

Photoionization Studies of Highly Excited States of Zinc

By

Ghulam Aisha

(27-FBAS/PHDPHY/S14)

A Thesis Submitted as the Partial Requirement for
the Award of Degree of Doctor of Philosophy in Physics at the
Department of Physic (FC) Faculty of Basic and applied Sciences,
International Islamic University, Islamabad

Supervisor:
Dr. Shaista Shahzada
Chairperson,
Associate Professor,
Department of Physics, FBAS, IIUI

Co-Supervisor:
Dr. Ali Nadeem
National Institute of Laser and Optronics College,
Pakistan Institute of Engineering and Applied Sciences

Department of Physics
Faculty of Basic and Applied Sciences
International Islamic University, Islamabad
(2020)

AUTHOR'S DECLARATION

I, **Ghulam Aisha** Reg. No. **27-FBAS/PHDPHY/S14** hereby state that my Ph.D. thesis titled: **"Photoionization Studies of Highly Excited States of Zinc"** is my own work and has not been submitted previously by me for taking any degree from this university, **International Islamic University, Sector H-10, Islamabad, Pakistan** or anywhere else in the country/world.

At any time if my statement is found to be incorrect even after my graduate the university has the right to withdraw my Ph.D degree.

Name of Student: **(Ghulam Aisha)**

Reg. No. **27-FBAS/PHDPHY/S14**

Dated:

International Islamic University, Islamabad
Faculty of Basic and Applied Sciences
Department of Physics

Photoionization Studies of Highly Excited States of Zinc

By

Ghulam Aisha
(27-FBAS/PHDPHY/S14)

Thesis submitted to

Department of Physics

International Islamic University Islamabad

for the award of the degree of

PhD Physics

Signature: _____

Dr. Shaista Shahzada
Chairperson
Department of Physics (FC FBAS)
International Islamic University
Islamabad

(Chairperson, Department of Physics)

Signature: _____

(Dean FBAS, IIU, Islamabad)

International Islamic University, Islamabad

CERTIFICATE OF APPROVAL

This is to certify that the research work presented in this thesis, entitled: **Photoionization Studies of Highly Excited States of Zinc** was conducted by **Ms. Ghulam Aisha,** Reg. No. **27-FBAS/PHDPHY/S14** under the supervision of **Associate Prof. Dr. Shaista Shahzada,** no part of this thesis has been submitted anywhere else for any other degree. This thesis is submitted to the **Department of Physics, FBAS, IIU, Islamabad** in partial fulfillment of the requirements for the degree of **Doctor of Philosophy in Physics, Department of Physics, Faculty of Basic & Applied Science, International Islamic University, Sector H-10, Islamabad, Pakistan.**

Student Name: Ghulam Aisha **Signatures:** _____

Examination Committee:

a) **External Examiner 1:**

Prof. Dr. Zafar Iqbal
Department of Physics
Riphah University, Islamabad

Signatures: _____

b) **External Examiner 2:**

Prof. Dr. Ishaq Ahmed
Department of Physics
COMSATS, Islamabad

Signatures: _____

c) **Internal Examiner:**

Dr. Imran Murtaza
Associate Professor, IIUI

Signatures: _____

Supervisor Name:

Dr. Shaista Shahzada
Associate Professor, IIUI

Signatures: _____

Co-Supervisor Name:

Dr. Ali Nadeem
Deputy Chief Scientist,
National Institute of Laser and Optronics College,
Pakistan Institute of Engineering and Applied Sciences

Signatures: _____

ACKNOWLEDGEMENT

I feel myself inept to regard the highness of **Almighty ALLAH**, my words have lost their expression, knowledge is lacking and lexis to express scarce to express gratitude in the rightful manner to the blessings and support of Allah. I present my humble gratitude from the deep sense of heart to the **Holly Prophet MUHAMMAD** (Peace Be Upon Him) that without him the life would have been worthless.

I have no words to express my deep gratitude to my honorable supervisor Dr. Shaista Shahzada, Associate Professor, International Islamic University, Islamabad, for her diligent cooperation and scrupulous support during the entire degree program. I expand my deepest appreciation and benedictions to my Co-Supervisor Dr. Ali Nadeem (Head of Laser Spectroscopy Laboratory, NILOP). He has taught me the methodology to carry out the research and to present research work as clearly as possible. I am thankful to them for their inspiration and encouragement in every field of life especially in education, teaching and research. Almighty Allah may bless them with long life, health, happiness and knowledge.

I want to especially thank to Director NILOP (National Institute of Lasers and Optronics) for providing me the chance to work under the great environment of laboratories, which were best for research purposes. I am thankful to Mr. Mehmood Shah Principal Scientist in NILOP for helping me in my experimental work. I also express my appreciation to Dr. Asma Nazir for her compassionate attitude and valued suggestions.

I extend my obligations to my loving parents and siblings for their love, care and support in my life which has been directly encouraging me for my study. Especially my mothers' prayers have always been a big support in solving my problems. Allah may bless my family health and happiness (Ameen).

Ghulam Aisha.
IIU Islamabad.

Dedicated to;

My beloved Parents, brothers, sisters and specially teachers.

Table of Contents

List of Figures

List of Tables

List of Publications

1. **Ghulam Aisha**, Mehmood Shah, Shaista Shahzada, Sami-ul-Haq, Hira Shakeel and Ali Nadeem, Investigation of the 4s*n*f $^1F_3$ Rydberg states of zinc and determination of dipole polarizability zinc ion, **Spectrochim. Acta Part B**: 142, 85–90 (2018).
2. **Ghulam Aisha,** M Shah, Ali Nadeem, S.U. Haq and Shaista Shahzada, Oscillator strength measurements of the 4s5s $^3S_1 \rightarrow$ 4s*n*p $^3P_2$ Rydberg transitions of zinc, **Spectrosc. Lett.** 52, 143-149 (2019).
3. Mehmood Shah, **Ghulam Aisha**, S. Shahzada and Ali Nadeem, Step-Wise Laser Excitation of the 4s*n*f ^{3}F Rydberg States of Neutral Zinc, **Spectrosc. Lett.** 51, 1–6 (2018).
4. Hira Shakeel, S. U. Haq, **Ghulam Aisha**, Ali Nadeem, Quantitative analysis of Al-Si alloy using calibration free laser induced breakdown spectroscopy (CF-LIBS), **Phys. Plasmas** 24, 063516 (2017).

*First three publications are included in this thesis.

List of Abbreviations

Ionization potential	**IP**
Ultra-violet	**UV**
Vacuum Ultra-violet	**VUV**
Full Width at Half Maximum	**FWHM**
Potassium Dideuterium Phosphate	**KDP**
Second Harmonic Generation	**SHG**
Beta Barium Borate	**BBO**
Free spectral range	**FSR**
Multi-Configuration Hartree Fock	**MCHF**
Configuration Interaction	**CI**
Quantum Defect Theory	**QDT**

Abstract

The present research work is devoted to the investigation of Rydberg states of zinc using multi-step laser excitation schemes. The experiments were carried out using the Nd: YAG pumped dye lasers. The first three step laser excitation experiment was perform to investigate the high orbital angular momentum ($\ell = 3$) states, in which the first excitation step was to populate the 4s4p $^1P_1$ resonance level at 213.92 nm using the frequency doubled dye laser. The second dye laser was fixed at 636.4 nm to excite the 4s4d $^1D_2$ level, the third dye laser was tuned up to the first ionization limit to investigate the 4s*n*f $^1F_3$ ($20 \leq n \leq 50$) Rydberg series. The term energies of 4s*n*f $^1F_3$ series were used for the determination of dipole polarizability of Zn^+ core as $\alpha_d = 18.33 \pm 0.95\, a_o^3$ using the core polarization model. In the second experiment, the inter-combination level 4s4p $^3P_1$ was populated at 307.38 nm using the frequency doubled dye lasers. The second dye laser was used to excite the 4s*n*d $^3D_2$ intermediate level. As the experiment was performed in a thermionic diode ion detector, therefore, the 4s*n*d $^3D_{1,3}$ states were also populated due to the thermal energy transfer. The new observations includes the 4s*n*f $^3F_3$ ($12 \leq n \leq 50$) series were observed from 4s*n*d $^3D_2$ intermediate levels. Whereas, the 4s*n*f $^3F_4$ ($12 \leq n \leq 33$) and 4s*n*f $^3F_2$ ($12 \leq n \leq 28$) Rydberg series were excited from 4s*n*d $^3D_3$ and 4s*n*d $^3D_1$ state respectively. In addition the ionization potential of zinc is determined as 75769.31±0.15 cm^{-1} using the term energies of 4s*n*f $^3F_3$ series. The third experiment was also carried out using the three step laser excitation scheme for the investigation of 4s*n*p $^3P_2$ ($18 \leq n \leq 53$) Rydberg series via 4s5s $^3S_1$ intermediate level. Oscillator strengths for the 4s5s $^3S_1 \rightarrow$ 4s*n*p $^3P_2$ Rydberg transitions of zinc from $n = 18$ to 53 have been determined. A relation has been established between the discrete *f*-values and the oscillator strengths distribution at the first ionization limit.

Chapter 1

Introduction

Zinc belongs to the group IIB elements of the Periodic Table along with cadmium and mercury, possessing s^2 ground state configuration. To excite one of the 4s electron from the 4s$n\ell$ Rydberg sequences, the main spectral appearance of zinc will be alkaline earth-like, consisting of singlet and triplet states. The alkaline earth elements have been extensively investigated using conventional as well as laser spectroscopic technique [1-5]. However, the lack of spectroscopic studies on the spectra of zinc is mainly due to their high ionization potential (9.39 eV) and secondly, the resonance 4s4p $^1P_1$ and inter-combination 4s4p $^3P_1$ levels lie in ultra-violet (UV) spectral region. The first systematic studies on the bound state of Zn I and Cd I was reported by Brown et al. [6] employing the conventional spectroscopic technique. The first ionization limit of zinc was determined using the much extended $4s^2\ ^1S_0 \rightarrow 4sn$p $^1P_1$ ($4 \leq n \leq 66$) Rydberg series as 75769.33 ± 0.18 cm^{-1}. Whereas, the first laser based work on zinc from the 4s4p $^{1,3}P_1$ intermediate states were reported by Kompitsas et al. [7] using the multi-step and multi-photon excitation. Their observations include 4snf $^{1,3}F_J$ ($8 \leq n \leq 26$), 4sns $^1S_0$ ($14 \leq n \leq 31$), 4snd $^1D_2$ ($12 \leq n \leq 35$) and 4snp ^3P ($10 \leq n \leq 40$) series. Subsequently, our laser spectroscopy group carried out detail investigation of the triplet 4sns, 4snp and 4snd states of zinc from the 4s4p ^3P and 4s5s $^3S_1$ intermediate states [8-13]. The objectives of the present research project was to investigate the high orbital angular momentum states ($\ell = 3$) of zinc that are still missing in literature, and extract the important atomic parameters. In order to probe the highly excited states step-wise laser excitation schemes were employed, in the following section step-wise laser excitation and selection rules are described.

1.1 Motivation

The motivation of the present research work was to investigate the highly excited singlet and triplet states of zinc using the multi-step or multi-photon laser excitation schemes. Energy levels, quantum defects, dipole polarizability and oscillator strength of high orbital angular momentum states have been presented. In atomic physics energy levels, oscillator strengths, lifetimes, transition probability, photoionization

cross-sections and dipole polarizability are important parameters in the fundamental research. The emission and absorption spectra of zinc are important in many research fields within astrophysical stellar atmosphere dynamics and in plasma physics. As the emission and absorption spectra of many astronomical bodies are comparable with the measured spectra in the laboratory, accurately measured transition probabilities (or f values) in the laboratory are required to study the dynamics of stellar atmosphere and plasma. Accurate measurement of energy levels or quantum defects of high orbital angular momentum states are important for the precise measurement of dipole polarizability. The atomic polarizability is used to determine the black body radiation shift which is largest frequency shift in atomic clocks. Oscillator strengths are also very important in thermonuclear research, where the atomic radiation is the major loss mechanism.

1.2 Step-wise Excitation

Photoionization spectroscopy is based on the multi-step or multi-photon excitation and subsequent ionization of excited atoms. The simplest way to perform step-wise excitation is to use different wavelength of lasers to successively excite the levels to probe the highly excited desired states. The high flux density attainable from the pulsed tunable lasers is mostly used to perform efficient step-wise excitation. In this way transition that lie in the ultra-violet region can be approached using the efficient narrow bandwidth dye lasers in the visible and ultra violet region. Figure 1.1 shows a step-wise laser excitation scheme. In the initial step, a resonant photon of energy $\hbar\omega_1$ excites the atom from the ground state. Then within the lifetime of the excited state another photon of energy $\hbar\omega_2$ further excites the atoms and so on the anticipated excited states can be investigated.

The transition probability per unit time is expressed as reported in [14]:

$$P_{if} = \frac{\pi\rho(\omega_{if})}{3\varepsilon_o\hbar^2}\left|\langle f|er|i\rangle\right|^2 \qquad (1.1)$$

Here, $\rho(\omega_{if})$ is the radiation density per unit interval of the angular frequency. The transition probability depends on the electric dipole matrix element $|\langle f|er|i\rangle|^2$. This term is non-zero only when the angular momentum between the initial and the final

levels changes as ± 1 (electric dipole transition is allowed only between the opposite parity). The single photon absorption follows the electric dipole selection rules:

$$\Delta \ell = \pm 1$$

$$\Delta J = 0, \pm 1 \text{ and } 0 \leftrightarrow 0 \text{ (not allowed)}$$

$$\Delta L = 0 \pm 1$$

$$\Delta S = 0$$

As the atomic number Z increases the $\Delta S = 0$, selection rule is relaxed and the inter-combination states can be populated.

1.2.1 Advantages of the Step-wise excitation

1. The step-wise excitation provides the maximum probability of exciting the atom to the high lying states.
2. Transitions in the vacuum ultra-violet region can be probed using dye lasers in visible and ultraviolet region.
3. The spectral resolution depends on the linewidth of the dye laser.
4. The time resolution on the order of the lifetime of the intermediate level can be achieved.

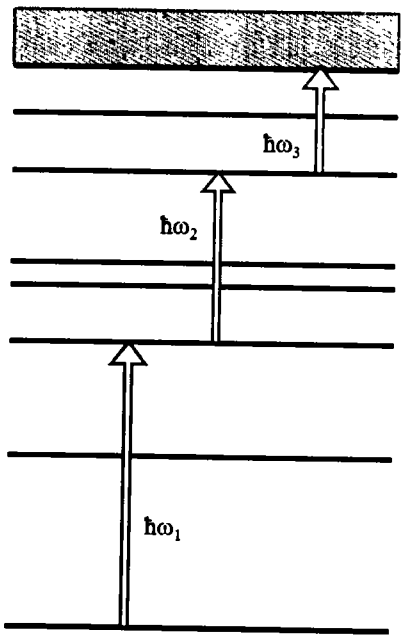

Figure 1.1 Step-wise excitation scheme to invesitigate the highly excited states.

The detection sensitivity of photoionization spectroscopy can be estimated using the following relation [15].

$$S = N_k P_{kI} \delta.\eta = n_a \frac{P_{kI}}{P_{kI} + R_k} \delta.\eta \tag{1.2}$$

Here, N_k is the density of excited state E_k of atoms or molecules, P_{kI} is the probability per second that excited atom will ionized from excited state, δ is the quantum efficiency for the ionized electron can reaches $\delta = 1$, and $n_k = \frac{P_{kI}}{P_{kI}+R_k}$ is the excited state quantum efficiency, it is proportional to the ratio of spontaneous transition rate to the total relaxation rate, that may also comprises radiation-less transition rate R_k. Therefore, if the probability of ionization P_{kI} is large enough than the relaxation rate R_k of the excited state $|k\rangle$, the ionization signal become $\delta = \eta = 1$ and becomes $S \sim n_a$. This implies that every photon absorbed in the transition $E_i \rightarrow E_k$ has been detected as ion or electron. It implies that single absorbed photon can be detected with an overall efficiency close to unity (or 100%). However, during the experimental work there are some additional losses and sources of noise, which limit the detection efficiency. Despite that ionization spectroscopy is the most sensitive detection technique and is superior to all other methods [15]. Since the research work is mainly based on the investigation of Rydberg states, therefore, in the following section the properties of the Rydberg atom are described.

1.3 Rydberg Atom

An atom in which the valence electron is excited far away from the ionic core to a state with high principal quantum number 'n' is called Rydberg atom. Rydberg atom sees the rest of the electrons and ionic core as positive charge and the system behaves like a hydrogen atom [14] as shown in Figure 1.2. The physical parameters such as fine structure splitting, binding energy, core polarizability, dipole moment, atomic size and life time depends on the principal quantum number n. The low orbital angular momentum states, which can penetrate the core, are described by the quantum defect theory. However, for the high orbital angular momentum states electrons are classically excluded from the core by the centrifugal potential, and as a result, core penetration does not occur in high ℓ states, but core polarization does and the

potential experienced by the excited electron is the sum of a polarized potential term and coulombic potential as reported by F. Gallagher [16].

$$V(r) = -\frac{e^2}{r} + V_{pol}(r) \tag{1.3}$$

The polarization potential $V_{pol}(r)$ is expressed as:

$$V_{pol}(r) = -\frac{1}{2}\left[\frac{\alpha_d}{r^4} + \frac{\alpha_Q}{r^6}\right] \tag{1.4}$$

α_d is dipole polarizability and α_Q is quadrupole polarizability of the core. Substituting the values of radial coordinate in the hydrogen like system $1/\langle r^4\rangle$ and $1/\langle r^6\rangle$, and considering that n is very large equation (1.4) will reduce to

$$V_{pol}(r) = -\left[\frac{3\alpha_d}{4n^3l^5} - \frac{35\alpha_Q}{16n^3l^9}\right] \tag{1.5}$$

Therefore, the binding energy is expressed as:

$$E_{n,\ell} = -\frac{R_{yd}}{n^2} + \frac{2R_{yd}\delta_\ell}{n^3} \cong \frac{R_{yd}}{(n-\delta_\ell)^2} \tag{1.6}$$

Where, $E_{n,l}$ is the nth level binding energy, R_{yd} is the Rydberg constant; n is the principal quantum number and δ_ℓ is the quantum defect.

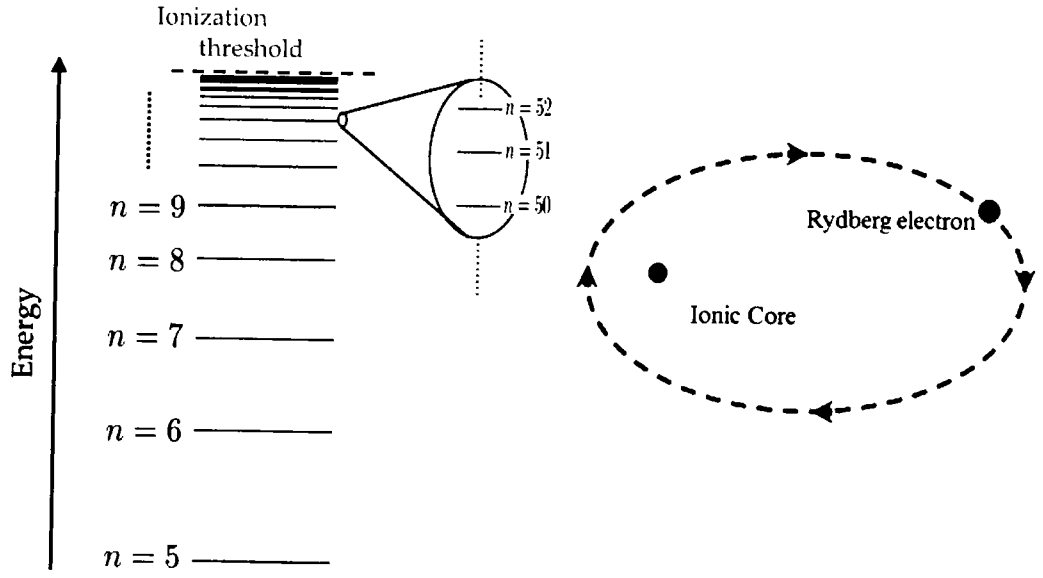

Figure 1.2 The classical picture of Rydberg atom. The nucleus located at one of the foci of ellipse is denoted by black dot and red dot is Rydberg electron.

The quantum defect is the measure of deviation from the hydrogenlike behavior. For low orbital angular momentum states quantum defects are large, and decreases with the increasing orbital angular momentum ℓ, and are independent on the principal quantum number n. The study of Rydberg atom has attracted much attention due to its importance in real physical systems [16-19]. In laboratory, the Rydberg atoms are created using the multi-step and multi-photon laser excitation. Rydberg atoms play vital role in astrophysical and laboratory plasma as it might be found in interstellar space, where the density is very low. Rydberg atoms are created by radiative recombination of low energy ions, electrons and dielectric recombination of higher energy ions and electrons. The highly exaggerated properties of Rydberg atoms make them distinctive from the other atoms.

1.4 Line Broadening Mechanisms

The line broadening mechanisms are divided into homogenous and inhomogeneous. All the broadening mechanisms are homogeneous except Doppler broadening. Broadening mechanism is homogeneous if it broadens the line of each atom in identical manner whereas; in inhomogeneous broadening the broadening is not identical for all atoms [20, 21]. In the following sections some important mechanisms are briefly described.

1.4.1 Natural Broadening

The line-broadening mechanism has its origin in the phenomenon of spontaneous emission. Since spontaneous emission is an inevitable process of any transition, the corresponding broadening is called natural or intrinsic. Every excited state has an intrinsic lifetime before it spontaneously decays to a lower energy state without any external influences. The natural broadening is the consequence of Heisenberg's uncertainty principal, which states that there is an uncertainty in the energy ΔE of the state, due to an uncertainty in the excited state lifetime Δt, such that $\Delta E \Delta t \approx \frac{h}{2\pi}$, the shape of frequency or power spectrum of exponentially decaying amplitude is a Lorentzian for the intensity as a function of frequency [14].

$$I(\omega) \approx \frac{1}{(\omega - \omega_o)^2 + (1/\tau)^2} \tag{1.7}$$

1.4.2 Doppler Broadening

The Doppler broadening is the broadening of spectral lines due to the thermal motion of atoms or molecules, the different velocities of the emitting species result different Doppler shifts, the collective effect of which is the line broadening. This resulting line profile is known as Doppler profile.

The Doppler line broadening depends only on the frequency of the spectral line, the mass of the emitting particles, and temperature. In order to estimate the full width half maximum (FWHM) for Doppler broadened line profile the following relation is used [22]:

$$\Delta\omega_D(Doppler) = 2\omega_o \upsilon_p (\ln 2)^{1/2} / c = 2\frac{\omega_o}{c}\left[\frac{2kT}{m}\ln 2\right]^{1/2}$$

$$= 7.16\times10^{-7}\omega_o\left[\frac{T}{M}\right]^{1/2} \qquad (1.8)$$

Where 'M' is molar mass of radiating particle, and 'T' is the temperature in kelvin. It can be reduced or eliminated by several techniques such as Doppler free spectroscopy. In ultra violet and visible region the Doppler broadening exceeds the natural line width by the two orders of magnitudes.

1.4.3 Collisional or Pressure Broadening

The line width broadening due to the collision of an atom with other atoms, ions, free electrons, etc. or with the walls of the container is known as collision broadening. Most importantly a considerable pressure of the buffer gas brings about a collisional broadening of spectral lines. Collision of emitting particle with other particles shortened the lifetime and increases the uncertainty in the energy (as occurs in natural broadening). This broadening is often greater than the natural broadening. The line width increase as a function of density of perturbing species. The collision-induced broadening of spectral line is also called pressure broadening [22]. From pressure broadening and pressure shifts of spectral lines, information about collision processes and interatomic potentials can be extracted. As a rough estimate we can say that, for any atom, collisions in a gas contribute to the line broadening by an amount $\Delta\nu \cong 1\text{MHz/Torr}$ [23].

According to the above description, the shape of a homogeneous line is always Lorentzian while that of an inhomogeneous line is always Gaussian. When these two mechanisms contribute to line broadening, the overall line shape become the convolution of the Lorentzian and Gaussian line profile functions which is called the Voigt profile.

1.5 Penetrating and non-penetrating orbits

Although there is no sharp line exists between penetrating and non-penetrating orbits. However, the low orbital angular momentum states ($\ell = 1,2$) are elliptical and this leads the orbits getting into the core and experience greater penetration and energy levels are different from those of hydrogen. Moreover, quantum defects δ_ℓ of the low orbital angular momentum states that penetrate the core are large, quantum defect may be considered as a measure of penetrating or non-penetrating orbit.

According to the quantum mechanical model the low orbital angular momentum orbit of lithium, s and p orbit of sodium and potassium and s, p, d orbits of rubidium and caesium are penetrating. The orbit $\ell = 3$ has maximum penetration. Whereas, for high orbital angular momentum states $\ell \geq 3$ the centrifugal barrier prevents core penetration. For these states the core penetration is negligible and the quantum defects are typically ≤ 0.1. Therefore, energies of the non-penetrating states are very nearly equal to the hydrogen.

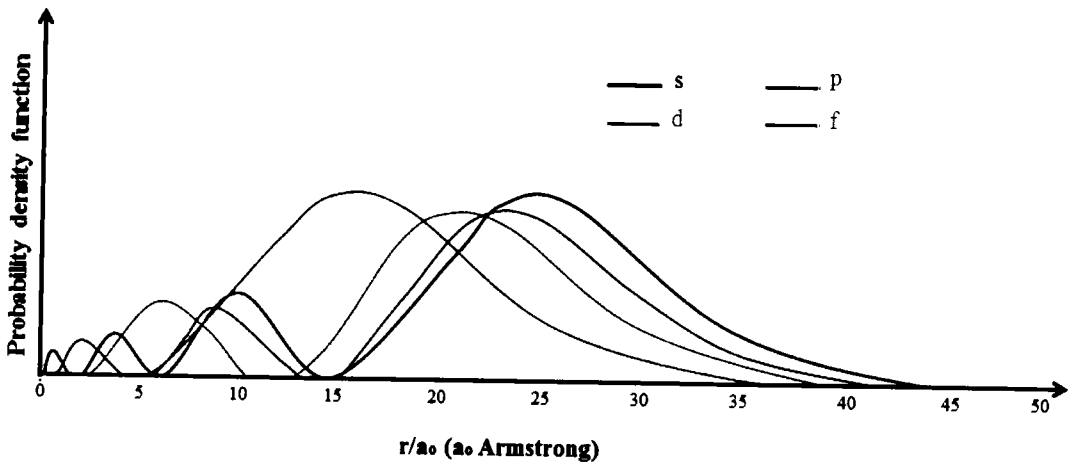

Figure 1.3 The probability density functions of penetrating and non-penetrating orbits of zinc.

The f-orbits of the alkali metals and most of the elements are good example of non-penetrating orbits [24]. It is also evident from the of probability density distribution curves as shown in Figure 1.3 that low orbital angular momentum states have small loops close to the core or nucleus. Whereas, as the orbital angular momentum increases the small loops shifted away from the core and the core penetration is almost negligible. In such cases, due to the central electrostatic interactions the active electron and passive core are coupled, and can be described by the "core polarization model". In this model [25], the core is denoted by a point nucleus which is surrounded by a deformable cloud of negative charge.

1.6 Dipole Polarizability

The dipole polarizability of an atom or ions defines the response in the lowest order of field strength of electrons to an external electric field. There are various experimental and theoretical ways for the determination of dipole polarizability [26]. The most important methods used in the field of spectroscopy are from the quantum defect, term energies of the Rydberg states and from the life times of the excited states of the non-penetrating Rydberg series [25, 27].

In the present research work, the dipole polarizability was determined using the term energies of the high principal and orbital angular momentum states using the core polarization model as introduced by [25]. According to the core polarization model, when an atom or molecule interacts with an external electric field the atom is polarized and the resulting charge distribution is characterized by induced electric multipole moments [28]. In this model the excited electron and the positive core are merely coupled by the central electrostatic potential. This has been applied by several researchers for the estimation of the dipole polarizability [29 - 31], under certain approximation i.e., that core penetration is almost negligible and in the absence of quadrupole polarizability α_q. For high orbital angular momentum $\ell \geq 3$ states the core penetration is almost negligible whereas, it can polarize the core which leads to non-zero quantum defects. In the absence of core penetration for high orbital angular momentum states, we can write term energy and ionization potential of the hydrogenlike system as:

$$IP - E(n,\ell) = T(n,\ell) + W_{pol}(n,\ell) \tag{1.9}$$

Where, IP is the ionization potential, $E(n,\ell)$ is the term energies of non-penetrating states, $\Delta W_{pol}(n,\ell)$ is the perturbation in energy due to the core polarization and $T(n,\ell)$ is the energy of the hydrogenlike system:

$$T(n,\ell)=\frac{Z^2R_{yd}}{n^2}\left[1+\left(\frac{\alpha Z}{n}\right)^2\left(\frac{n}{\ell+(1/2)}\right)-\left(\frac{3}{4}\right)\right], \tag{1.10}$$

Z is the net charge of the nucleus and core electrons, α is the fine structure constant, R_{yd} is the Rydberg constant, n is the principal quantum number and ℓ is the orbital angular momentum. The $\Delta W_{pol}(n,\ell)$ is the perturbation energy due to the core polarization:

$$\Delta W_{pol}(n,\ell)=R_{yd}a_o\left[\alpha_d\left\langle r^{(-4)}\right\rangle_{(n,\ell)}+\alpha_q\left\langle r^{(-6)}\right\rangle_{(n,\ell)}\right] \tag{1.11}$$

Where $\langle r^{-4}\rangle$ and $\langle r^{-6}\rangle$ are radial coordinate of the hydrogenlike system [32]:

$$\left\langle r^{-4}\right\rangle_{n,\ell}=\frac{3-\dfrac{\ell(\ell+1)}{n^2}}{2n^3\left(\ell-\dfrac{1}{2}\right)\ell\left(\ell+\dfrac{1}{2}\right)(\ell+1)\left(\ell+\dfrac{3}{2}\right)}$$

$$\left\langle r^{-6}\right\rangle_{n,\ell}=\frac{35-5\left[\dfrac{6\ell(\ell+1)-5}{n^2}\right]+\left[\dfrac{3(\ell-1)\ell(\ell+1)(\ell+2)}{n^4}\right]}{8n^3\left(\ell-\dfrac{3}{2}\right)(\ell-1)\left(\ell+\dfrac{1}{2}\right)\ell(\ell+1)\left(\ell+\dfrac{3}{2}\right)(\ell+2)\left(\ell+\dfrac{5}{2}\right)}$$

By substituting equation (1.11) in equation (1.9) and rearranging:

$$\frac{IP-E(n,\ell)-T(n,\ell)}{R_{yd}a_o\left\langle r^{-4}\right\rangle_{n,\ell}}=\alpha_d+\alpha_q\left(\frac{\left\langle r^{-6}\right\rangle_{n,\ell}}{\left\langle r^{-4}\right\rangle_{n,\ell}}\right), \tag{1.12}$$

The plot of the left hand side of the equation (1.12) versus $\langle r^{-6}\rangle/\langle r^{-4}\rangle$ is the polarization graph. In the absence of core penetration for the high orbital angular momentum states, the polarization graph is linear. Its y-intercept gives the value of the dipole polarizability α_d, and from its slop the quadrupole polarizability can be determined as described in [31].

1.7 Oscillator Strength

Oscillator strength is the measure of relative strength of electronic transitions, that how much a transition is strong in comparison to other transitions which originate from the same energy level. It is a dimensionless quantity and plays a vital role in study of atomic studies. Oscillator strengths have many applications in plasma physics and astrophysical studies for determination of atomic abundance. A comprehensive review on the oscillator strengths measurement techniques have been complied by Huber and Sandeman [33].

In the present work, the oscillator strengths of the Rydberg transitions were determined using the technique introduced by Mende and Kock [34], with the assumption that the ionization probability of levels should be unity if the energy difference ΔE lie within $k_B T$, where k_B is the Boltzmann constant and T is the temperature (kelvin). This technique has been used by many researchers for the calibration of oscillator strength of Rydberg transitions [35 - 39]. In the following section the technique has been described in detail.

In photoionization laser pulses are used to study the Rydberg states of atoms using step-wise excitation. The first laser ℓ_1 is used to excite the atoms from ground state to intermediate excited state and then the second laser ℓ_2 is tuned to investigate the Rydberg states. The first laser ℓ_1 excites the atomic vapor and generate a column of atoms. The density of excited atoms can be adjusted by the mode of operation of the thermionic diode ion detector. So, the integrated number density $\tilde{N}_{ex}$ is written as follows:

$$\tilde{N}_{ex} = \int_0^d N_{ex} ds \tag{1.13}$$

Here, the excited vapor column length is represented as d and, when the second laser ℓ_2 is scanned through the excited vapor column, it ionized the excited atoms. The number of ions n_{ion} detected per pulse as a result of photoionization is given by,

$$n_{ion} = \int_{pulse} \sigma^{+}(\nu)\phi(\nu) N_{ex}\, d\nu \tag{1.14}$$

Here, σ^+ is the photoionization cross section at the first ionization threshold, the number of photon is written in frequency range (ν, dν) is $\phi(\nu)$dν and its averaged value is constant over the linewidth of the laser pulse. The equation (1.14) can be written in terms of total number of photons as:

$$n_{ion}(\nu) = \Phi_o N_{ex} \int_{Pulse} \sigma^+(\nu')P(\nu-\nu')d\nu' \tag{1.15}$$

Here, $P(\nu)$ is the normalized profile of the laser pulse and Φ_o is the total number of photons, which is defined as,

$$\Phi_o = \frac{E_i}{h\nu^+} \tag{1.16}$$

E_i is the energy of all the ionizing photons within a single laser pulse and $h\nu^+$ is the energy of a ionizing photon.

By substituting the value of Φ_o and $\int_{pulse} \sigma^+(\nu')P(\nu-\nu')d\nu = \overline{\sigma^+(\nu)}$ in expression (1.15) we have:

$$n_{ion}(\nu) = \frac{E_i}{h\nu^+} N_{ex} \overline{\sigma^+(\nu)} \tag{1.17}$$

The voltage drop over the thermionic diode is related with the number of ions detected, if thermionic diode is operated in linear mode:

$$U^+(\nu) = \beta n_{ion}(\nu) \tag{1.18}$$

Here, n_{ion} is the number of ions detected and β is the yield of the detector. The energy of ionizing laser E_i is checked at each step and the corresponding photo ion signal $S^+(\nu)$ is given as:

$$S^+(\nu) = \frac{U^+(\nu')}{E_i} = \frac{\beta n_{ion}}{E_i} \tag{1.19}$$

Substituting the value of n_{ion} from equation (1.17) we have:

$$S^{+}(v)=\frac{\beta n_{ion}}{E_{i}}=\beta\frac{E_{i}}{hv^{+}}\overline{\sigma^{+}(v)}\frac{1}{E_{i}}N_{ex}$$

$$S^{+}(v)=\beta\frac{1}{hv^{+}}\overline{\sigma^{+}(v)}N_{ex} \tag{1.20}$$

The expression (1.20) shows the signal strength at the continuum. The Rydberg states with quantum number n are excited by photo-excitation and consequently ionized by collisions with the probability P_n as:

$$n_{ion}^{R_{yd}}=P_{n}n^{R_{yd}} \tag{1.21}$$

If the ionization probability of the Rydberg transitions is unity i.e., $P_n \cong 1$, then the photo-absorption can be determined as:

$$n_{ion}^{R_{yd}}(v)=n^{R_{yd}}(v)=\int_{Pulse}\sigma^{n}(v)\phi(v)N_{ex}\,dv$$

$$n^{R_{yd}}(v)=N_{ex}\Phi_{o}\int_{Pulse}\sigma^{n}(v')P(v-v')dv' \tag{1.22}$$

By substituting $\Phi_{o}=\frac{E_{i}}{hv_{n}}$ in equation (1.22) we have,

$$n^{R_{yd}}=\frac{E_{i}}{hv_{n}}N_{ex}\int_{Pulse}\sigma^{n}(v')P(v-v')dv' \tag{1.23}$$

The total ion signal $S^{R_{yd}}$ produced due to photo-absorption into Rydberg state is given as:

$$S^{R_{yd}}=\frac{U^{R_{yd}}}{E_{i}} \tag{1.24}$$

$$S^{R_{yd}}=\beta\frac{n_{ion}^{R_{yd}}}{E_{i}} \tag{1.25}$$

$$S^{R_{yd}}=\beta\frac{E_{i}}{hv_{n}}N_{ex}\int_{Pulse}\sigma^{n}(v')P(v-v')dv'\frac{1}{E_{i}}$$

$$S^{R_{yd}} = \beta \frac{N_{ex}}{h\nu_n} \int_{Pulse} \sigma^n(\nu') P(\nu - \nu') d\nu' \tag{1.26}$$

The total line absorption is obtained by integration over the entire absorption profile

$$S^{R_{yd}} = \beta \frac{N_{ex}}{h\nu_n} \int_{line} \int_{Pulse} \sigma^n(\nu') P(\nu - \nu') d\nu' d\nu$$

$$S^{R_{yd}} = \beta \frac{N_{ex}}{h\nu_n} \int_{line} \sigma^n(\nu') d\nu' \int_{Pulse} P(\nu - \nu') d\nu$$

Since $\int_{line} \sigma^n(\nu') d\nu' = \frac{1}{4\pi\varepsilon_o} \frac{\pi e^2}{mc} f_n$ (for optically thin transitions)

$$\int_{Pulse} P(\nu - \nu') d\nu = 1$$

$$S^{R_{yd}} = \beta \frac{1}{4\pi\varepsilon_o} \frac{\pi e^2}{mc} \frac{f_n}{h\nu_n} N_{ex} \tag{1.27}$$

Taking the ratio of equation (1.27) and equation (1.20) we have:

$$\frac{S^{R_{yd}}}{S^+(\nu)} = \frac{\beta \frac{1}{4\pi\varepsilon_o} \frac{\pi e^2}{mc} \frac{f_n}{h\nu_n} N_{ex}}{\beta \frac{1}{h\nu^+} \overline{\sigma^+(\nu)} N_{ex}}$$

$$\frac{S^{R_{yd}}}{S^+(\nu)} = \frac{1}{4\pi\varepsilon_o} \frac{\pi e^2}{mc} f_n \frac{V^+}{V_n \overline{\sigma^+(\nu)}}$$

$$f_n = \frac{4\pi\varepsilon_o mc}{\pi e^2} \left(\frac{S^{R_{yd}}}{S^+} \right) \left(\frac{\nu_n}{\nu^+} \right) \overline{\sigma^+(\nu)} \tag{1.28}$$

Here, the oscillator strength f_n for Rydberg transition has direct relation to the photoionization cross section $\overline{\sigma^+(\nu)}$ determined at a frequency ν^+. If λ^+ is the ionizing laser wavelength of the corresponding to the threshold value and wavelength for the n^{th} transition of Rydberg series is λ_n then the expression can be written as:

$$f_n = \frac{4\varepsilon_o mcS^{R_{yd}}\lambda^+}{e^2 S^+ \lambda_n}\sigma^+ \tag{1.29}$$

Hence if the value of photoionization cross section for intermediate excited state at first ionization limit is known, then the oscillator strengths of all highly excited Rydberg transitions for which ionization probability is unity ($p_n \cong 1$) can be determined.

1.7.1 Differential Oscillator Strength

The concept of oscillator strength (*f*-value) is appropriate for discrete states over which an integration can be performed, but not for a continuum extending over a wide energy range. In this case, the differential oscillator strength or *f*-value per unit energy interval is measured in the units of energy. The connection between the oscillator strengths distribution in the bound region and oscillator strength density dE/df at the ionization threshold is represented as [40];

$$\lim_{n\to\infty} \frac{(n^*)^3}{2R_{yd}} f_n = \left.\frac{df}{dE}\right]_{E=E_{ion}} \tag{1.30}$$

Here, n^* is the effective quantum number, R_{yd} is the mass corrected Rydberg constant and E is the photon energy. The cross-section at the threshold is related to the oscillator strength density df/dE as:

$$\frac{df}{dE} = 9.11\times10^{15}\,\sigma(E) \quad (\text{eV})^{-1} \tag{1.31}$$

The plot between df/dE and excess energy (eV) demonstrate that how the *f*-values in the discrete region related with the oscillator strength density at threshold. This continuity across the threshold is a fundamental principle of the quantum defect theory, which originates from the continuity in the wave function across the threshold.

1.8 Thesis Layout

In present research work we applied the multi-step laser excitation schemes in order to investigate the Rydberg states of zinc. In a series of experiments a Q-switched Nd: YAG laser (Spectra Physics DCR-3), at 10 Hz was used to pump the dye lasers, and

thermionic diode ion detector and atomic beam set-up was used for ion detection. First chapter deals with theoretical background of multi-step excitation, Rydberg atom, line broadening mechanisms, dipole polarizability and oscillator strength. The second chapter contains the brief description of instruments used in experimental work.

Chapter three described the detail investigation of 4s*n*f $^1F_3$ Rydberg series of zinc from n = 20 to 50 using three-step laser excitation scheme, the experiment was performed in atomic beam set-up. The intermediate level 4s4d $^1D_2$ was populated and 4s*n*f $^1F_3$ Rydberg series was extended up to n = 50. The term energies and quantum defects of high orbital angular momentum were determined. In addition the dipole polarizability of the Zn^+ core was determined as $\alpha_d = 18.33 \pm 0.95\, a_o^3$ using core polarization model which is in good agreement with the reported result.

In chapter four the experimental studies were further extended to investigate the 4s*n*f ^3F states of zinc from the 4s*n*d $^3D_2$ multiplet. Since the experiment was performed in thermionic diode and because of the thermal energy collision the 4s*n*d $^3D_{1,3}$ level was also get populated as result 4s*n*f $^3F_3$ ($12 \le n \le 50$), 4s*n*f $^3F_2$ ($12 \le n \le 28$) and 4s*n*f $^3F_4$ ($12 \le n \le 33$) Rydberg series were observed. The ionization limit of zinc has also been measured as 75769.31 ± 0.15 cm^{-1} using extended Rydberg-Ritz relation.

In chapter five the 4s4p $^3P_2$ ($18 \le n \le 53$) Rydberg series was investigated from intermediate 4s5s $^3S_1$ level. In addition oscillator strengths of the 4s5s $^3S_1 \rightarrow$ 4s*n*p $^3P_2$ ($18 \ge n \ge 53$) have been determined. A connection between discrete oscillator strengths and oscillator strength density at the limit has been verified.

Chapter 2

Experimental Details

The schematic diagram of our experimental set-up based on atomic beam apparatus is shown in Figure 2.1 whereas; experiments performed on the thermionic diode detector were explained in the succeeding section. A Q-switched Nd: YAG laser system was used as pump source for the dye lasers. All the experimental works were carried out by three step excitation scheme. The three dye lasers were pumped by the second or third harmonic of the Nd: YAG laser. The wavelength of first two dye lasers were fixed to pump the intermediate levels and third laser was scanned across a wavelength range to investigate the Rydberg series. During the experiments we have used various instruments which are briefly described in the following sections.

2.1 Laser System

We have used Spectra Physics Nd: YAG laser (model DCR-III) operating in the Q-switch mode as the pumping source. The unstable type laser resonator with the output coupler of a high reflectivity dot in the center, creating a donut shape spatial profile. The primary wavelength of the laser is 1064 nm, which was frequency doubled and triple with the help of a non-linear Potassium Dideuterium Phosphate (KD*P) crystal. Dichroic mirrors are used to separate the harmonics. The repetition rate of the laser can be varied from 10 to 15Hz; however, in our experiments we have operated the laser at 10Hz. Some significant properties of the Nd: YAG laser system at its fundamental wavelength and its second third and fourth harmonics are given in the Table 2.1.

Table 2.1 Properties of Nd: YAG laser system at fundamental wavelength and its SHG and THG and FHG.

Properties	1064 nm	532 nm	355 nm	266 nm
Energy per pulse (mJ)	850	360	160	80
Pulse Width (ns)	12-10	9 – 7	7 – 5	5 – 4
Beam Diameter	7 mm			
Beam Divergence	< 0.5 m rad			

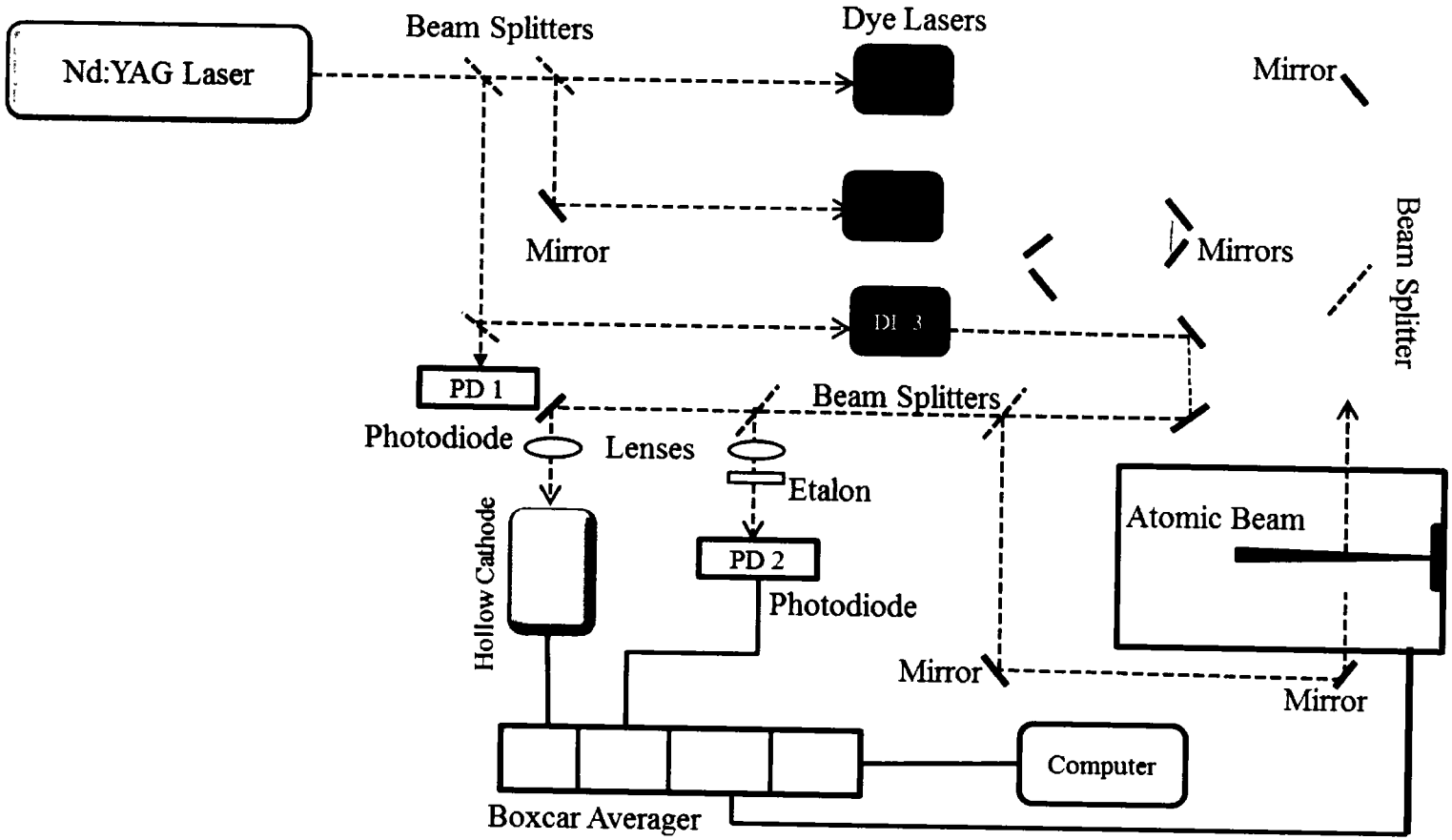

Figure 2.1 Schematic diagram of experimental setup.

Dye lasers are coherent tunable light source, covering the spectral region from ultra-violet (UV) to near infrared. Dye laser action was achieved in an optically pumped dilute solution of an organic dye in methanol, ethanol and DMSO etc. Since the fluorescence of a dye laser is approximately 100-200 cm^{-1} wide, therefore laser wavelength can be tuned using a diffraction grating. Dye lasers were discovered by Sorokin et al. [41] and Schafer et al. [42] in 1966. Initially, tunability of the dye laser was considered as the most important property. Later, dye laser development using various configurations has proceeded very rapidly for better resolution and line-width [43]. The first very successful and widely used design for narrow linewidth pulsed dye laser was introduced by Hänsch et al. [44]. The important feature of the cavity was the inverted telescope as beam expander to illuminate the high dispersion echelle grating as wavelength selector. Although this design was very successful, however, the telescope has few drawbacks such as exact alignment of the telescope cavity on the cavity axis produces undesirable feedback reflection at the lens. Since the beam expansion is essentially required for the narrow bandwidth dye laser cavity, therefore the numbers of alternative designs have been tried using single and multiple prisms as beam expender [45 - 47].

In the present experimental work, we have used the Hanna et al. [48] type single prism dye laser cavity in which prism is used beam expander and reflection grating for wavelength selectivity. As shown in Figure 2.2 a cylindrical lens of 10 cm focal length focus the second harmonic (532 nm) or third harmonic (355 nm) of the Nd:YAG laser in the dye cell.

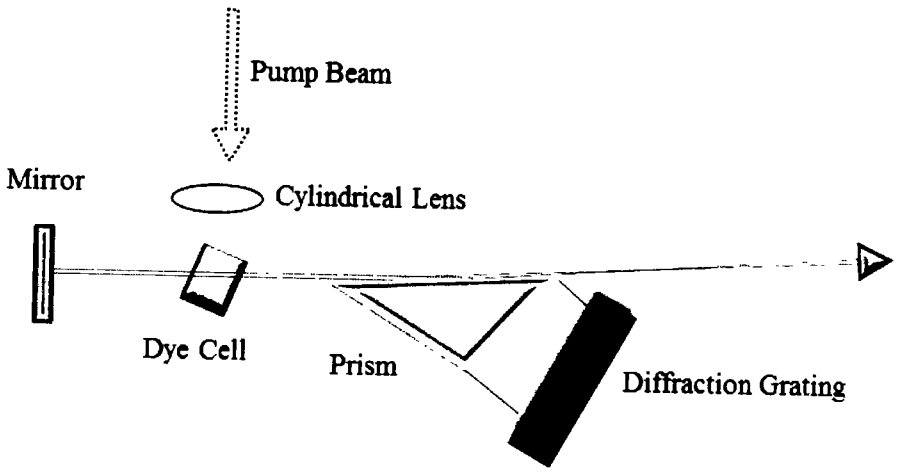

Figure 2.2 Schematic diagram of the Hanna type dye laser cavity.

A high reflecting mirror is placed on one side of the dye cell in order to reflect back the fluorescence in the dye cell, a right angle prism is used as a beam expander and diffraction grating used for wavelength selectivity. The prism is placed at an angle of incidence for beam expansion to illuminate the maximum number of lines of the grating which increases the resolution. Since the resolution is proportional to the grating grove number times the grating diffraction order. The grating was mounted on the rotational stage for tuning of the dye laser connected with a stepper motor. The linewidth of the dye laser was 0.3 cm^{-1}. The wavelengths of the dye lasers were measured with a spectrometer (Ocean Optics, HR-4000, 200–1100 nm and 0.75 nm resolution) equipped with a 600 lines/mm grating. The energy of the dye lasers were measured using an energy meter (Top Max II, Coherent) using a compatible sensor.

2.2 Second Harmonic Generation

The resonance 4s4p $^1P_1$ and inter-combination 4s4p $^3P_1$ levels of zinc lie in the ultraviolet region, therefore to excite these levels the frequency doubling (also known as second harmonic generation SHG) of the dye lasers were performed using the non-linear beta barium borate (BBO) crystals.

The second harmonic generation, first time observed by Franken et al. [49], is probably the most commonly known non-linear optical effect. The phenomenon of the SHG has been described in detail in several books [50, 51]. Nowadays, non-linear optical mixing techniques have extended the range of a coherent light source from vacuum ultra-violet to far infra-red. The efficiency of the harmonics generation depends upon the intensity of the incident laser radiation and also on its direction of propagation in crystal. In the following section the basic principles of second harmonic generation has been briefly described.

When the short laser pulses of 10^{12} W/cm^2, corresponding to an electric field of the order of 10^5–10^8 V/cm, generated by pulsed laser is interacting with a non-linear optical crystal. Then the polarization of the medium is no longer linearly dependent on E and can be expanded in a power series.

$$P = \varepsilon_o(\chi^1 E + \chi^2 E^2 + \chi^3 E^3 + \cdots) \qquad (2.1)$$

Here, the coefficients χ^2, χ^3 ... are second and third order susceptibilities. The optical characteristics, such as dielectric permittivity, refractive index, of a medium also become functions of the field strength E. The nonlinear phenomena of the second order are described by the second term of the equation (2.1). This term is also responsible for the frequency mixing and parametric conversion.

Consider a plane wave of frequency ω and wave vector k propagating in the z direction through a non-linear crystal. For a plane wave of uniform intensity we can write the following expression for the electric field.

$$E_\omega(z,t) = [E(\omega)\exp(i\omega t - i\,k_\omega z)] + complex\ conjugate \qquad (2.2)$$

$$k_\omega = \frac{\omega}{c} = n_\omega \omega / c_o \qquad (2.3)$$

Where k_ω is the frequency dependent wave vector, c_ω is the velocity of light in the crystal, c_o is the velocity of light in vacuum and n_ω refractive index at frequency ω. Then the induced nonlinear polarization produced by the electric field E of the electromagnetic wave can be written as:

$$P(2\omega) = \varepsilon_o \frac{d}{2}\{E^2(\omega)\exp(i2\omega t - 2k_\omega z)\} + complex\ congugate \qquad (2.4)$$

The electromagnetic wave of the 2ω may be expressed as:

$$E(z,t) = \{E(2\omega)\exp(i2\omega t - 2ik_{2\omega} z) + complex\ congugate \qquad (2.5)$$

Where,
$$k_{2\omega} = \frac{2\omega}{c_{2\omega}} = \frac{2n_{2\omega}}{c_o}\omega \qquad (2.6)$$

The above condition must be satisfied for the second harmonic generation i.e., the phase velocity $v_{ph}(\omega) = {}^{\omega}/_{k_\omega}$ of the incident wave must be equal to the phase velocity of the second harmonic wave $v_{ph}(2\omega) = {}^{2\omega}/_{k_{2\omega}}$. Therefore, the phase matching condition can be written as: $k_{2\omega} = 2k_\omega$. The phase matching condition in terms of refractive index. $n_{2\omega} = n_\omega$. That is the phase matching condition can be achieved in birefringence optical crystal in certain direction θ against the optical axis where the refractive index for the ordinary wave $n_o(\omega)$ is equal to the extraordinary

wave $n_e(2\omega, \theta)$. It is important that polarization direction of the second harmonic wave is orthogonal to that of the fundamental wave.

In the present experimental work, the frequency doubling of the dye lasers were achieved using the β-Barium Borate Type-I crystal (CASTECH Inc. China). Figure 2.3 shows that the dye laser beam was focused into the BBO crystal using a positive lens focal length of 10 cm; the BBO crystal was mounted on a rotationary stage to adjust the angle for phase matching.

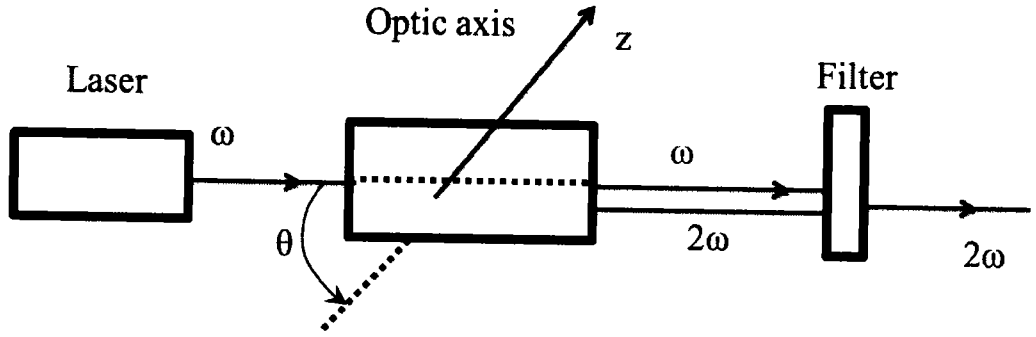

Figure 2.3 Schematic diagram for second harmonic generation (SHG)

The phase matching conditions for second harmonic generation can be achieved by angle tuning. This crystal is placed inside a mount which can be rotated in all dimensions in order to get all required phase matching angles. The fundamental and frequency doubled dye laser beams were separated using a quartz prism or filter.

2.3 Thermionic diode ion detector

Over the last few decades, thermionic diode ion detector, also known as the hot-wire detector, has been extensively used for the laser spectroscopy of atoms and molecules using the pulsed and CW lasers [52 - 55]. Niemex [56] and Beigang et al. [57], have discussed in detail the basic principle, different configurations and history of the thermionic diode detectors. The reasons for its popularity are several, it is linear, has a large dynamic range and a very high gain of 10^6, excluding the need of any electron multiplier or an external amplifier. Due to this high gain the detector offers a better signal-to-noise ratio, making the spectroscopic studies of very high Rydberg states very convenient. In spite of these advantages, it is cheap and easily design and fabricated for laser spectroscopic studies.

2.3.1 Construction and Operation

The thermionic diode detector used in the present experimental work is similar as described by Niemax [56] and Griesmann et al. [58]. The design has been used by number of research groups [59 - 61]. The design and construction of the thermionic diode developed in our laboratory is briefly described here, it mainly consists of stainless steel cylindrical tube. The stainless steel tube serves as an anode (35 cm long, inner diameter of 3 cm and 1 mm wall thickness) as shown in Figure 2.4. The tube was connected with the rotary pump to reduce the pressure down to 0.01 mbar. A thermos-coax wire was wrapped in a bifilar manner in the middle of the tube for heating using the dc power supply up to 1000 °C. The center region was further shielded by the glass wool to reduce the heating losses. The both ends of cell are water cooled to protect windows from heating. The cathode is a long thin wire of tungsten or molybdenum stretch axially slightly off centered along the tube. The work function of the cathode wire is low having diameter of about 0.25 mm. Cathode wire was heated using the separate power supply 4-5 A current at ~ 10V. A small boat filled with 2 to 4 g of target material placed nearby the central region. Both ends of thermionic diode detector are sealed by quartz windows and rotary pump is used to pump down to 10^{-3} mbar. In order to produce constant/uniform column density of vapor and to shield the quartz windows from the chemical attack of the hot vapor a buffer gas is inserted (or flowing) into the thermionic ion detector. The temperature is monitored by a thermocouple. In the central heating region the temperature profile almost remains constant, which confirmed the uniform column density.

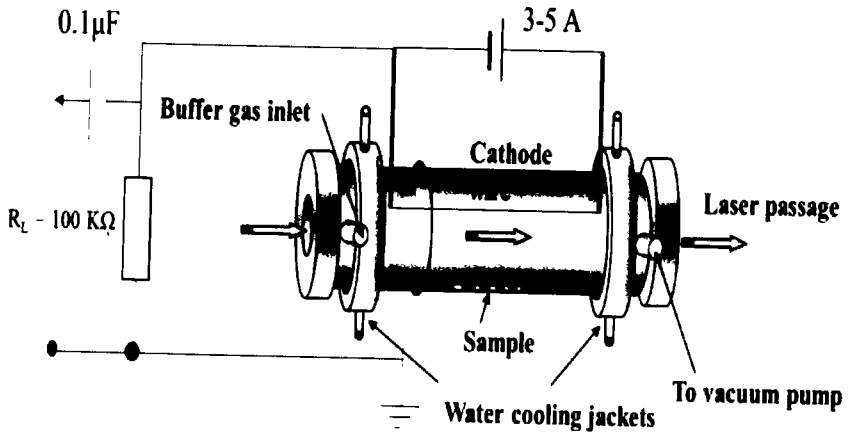

Figure 2.4 The schematic diagram of thermionic diode.

In thermionic diode the electrons are thermionically emitted from the cathode wire, but due to the small bias voltage on the cathode wire the current is limited by the electron space charge close the wire. When an atom is excited to high Rydberg states by laser excitation, it is collisionally ionized. The ions are confined in space charge and get depleted; therefore, more electrons are able to reach the anode and the electron current increases. This change in current can be observed across the 100 kΩ load resistor.

2.4 Atomic beam system

The design and fabrication of the resistively heated source used in the present experiments is similar as described by Nisar et al. [62]. The resistively heated atomic beam oven was inserted into the cylindrical vacuum chamber from one port as shown in Figure 2.1. This vacuum chamber was pumped down to $\approx 2 \times 10^{-6}$ mbar using the combination of rotary and diffusion pump. The chamber consists of five ports of different sizes; two ports were used to feed the dye laser beams in the direction transverse to the atomic beam. The additional ports are used for the electrical connection of power supplies to the electron multiplier channeltron and oven assembly. The design of the oven assembly is shown in Figure 2.5.

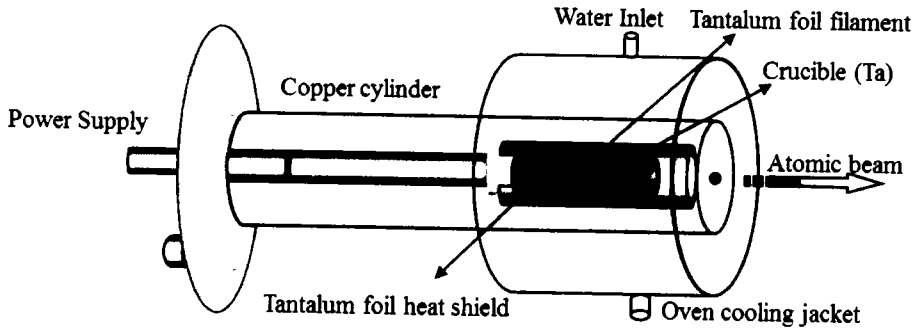

Figure 2.5 The cross section of oven assembly.

The main part of the oven assembly is the tantalum crucible 25 mm long, 8 mm inner diameter and thickness of 1-mm having a 0.2 mm hole. The crucible is coupled with a tantalum coupling rod and then fed into the high current copper feedthrough. The filament is made of tantalum foil of 0.05 mm thickness surrounded by the crucible and the crucible is heated by radiation. The high current feedthrough is adjusted on the assembly flange (see Figure 2.5) having two electrodes, two copper braids are

used for electrical connection from a dc power supply (500 A, 20V). A cathode cylinder of 5 cm diameter provides the return path for current flow. The beam source is placed horizontal and is fixed in a water cooled casing and to make sure the safe operation the cooling of the electrodes. The beam is collimated by means of diaphragm which is mounted in front of the atomic beam oven. The beam divergence is 56 mrad for full angle and atomic beam density in the interaction region is $\approx 10^8$ to 10^{10} atoms/cm^3. The maximum attainable operating temperature is $\approx$ 2000 °C, temperature measurements are made with a pyrometer. A thin tantalum foil is wrapped around the oven assembly acts as a radiation shield for the radiative heat losses.

In the center of the chamber two parallel plates with cross section of 5 x 5 cm^2 were mounted separated 1-cm as shown in Figure 2.6. When the dye lasers enters in the interaction region from both sides of the chamber they interact with the atomic beam orthogonally, the photoions produce are detected by channeltron electron multiplier mounted orthogonal to the atomic beam and dye lasers.

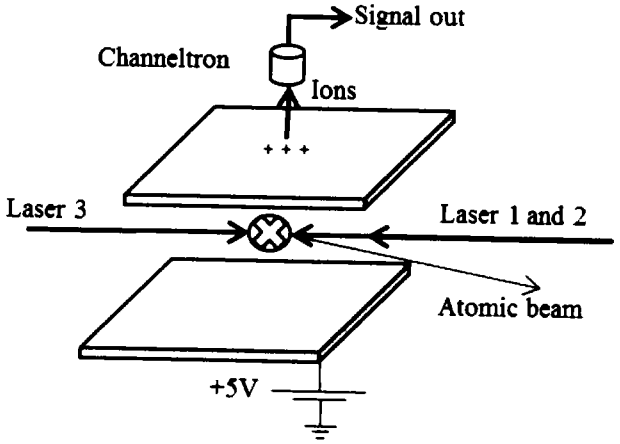

Figure 2.6 The schematic diagram of detection system.

At the lower plate a small positive voltage of 5 V is applied to push the ions towards the channeltron. In the center of the upper plate a 2 cm diameter hole with mesh allows the access of the electrons.

2.5 Data Acquisition System

In order to recover the signals from the noisy background of the atomic beam set-up and from thermionic diode ion detector the data acquisition system consisting of

SR280 Boxcar Averager mainframe and display. The mainframe is NIM (Nuclear Instrumentation Module) module compatible with the SR250 gated integrator NIM module which was fixed in the mainframe, the SR250 have versatile, high-speed, designed to recover fast analog signals from noisy backgrounds. It consists of a gate generator, a fast gated integrator, and exponential averaging circuitry. The gate generator, triggered internally or externally, provides an adjustable delay from a few nanoseconds to 100 ms before it generates a continuously adjustable gate with a width between 1 ns and 15 μs. The maximum signal to noise (S/N) ratio depends on the accurate position of the gate.

The pulse laser through a photodiode triggered both the Boxcar Averager and oscilloscope. The SR250 module has signal and gate outputs, which were fed in the oscilloscope (Agilent Technologies DS06104A) to adjust the position of gate and signal. Finally, the outputs from the SR250 were fed into the SR245 computer interface module for the data acquisition; it provides both an analog and a digital interface. Data were stored on a personal computer using a GPIB PCIIA card (IEEE 488.2) of National Instruments, using a computer code developed in our laboratory.

2.6 Wavelength Calibration

The wavelength calibration was achieved by simultaneously recording the three signals of the scanning dye laser. A small fraction (≈10%) is fed into the hollow cathode lamp to record the optogalvanic spectra of neon or argon which provide the wavelength references. Hollow cathode lamp consists of a glass tube which contains electrodes (anode and cathode) and buffer gas. A large voltage across the electrodes causes the buffer gas to ionize which create the plasma. When laser light pass through this discharge volume and tuned to the transition between two levels of atoms and ions in the discharge the population densities are changed by optical densities. So with the change in population density of ions and free-electrons a variation in discharge current appeared and then sensed across the load resistor of 10KΩ as a voltage drop. Even with low laser power large optogalvanic signals from μV to mV can be observed. Another fraction of the dye laser was used to record the etalon fringes of 1-mm thick solid etalon using photodiode which serve as relative frequency markers. The three output signals were fed into three boxcar averagers (SR-250),

whose outputs were stored on a PC. A typical spectrum recorded during the experiment is shown in Figure 2.7.

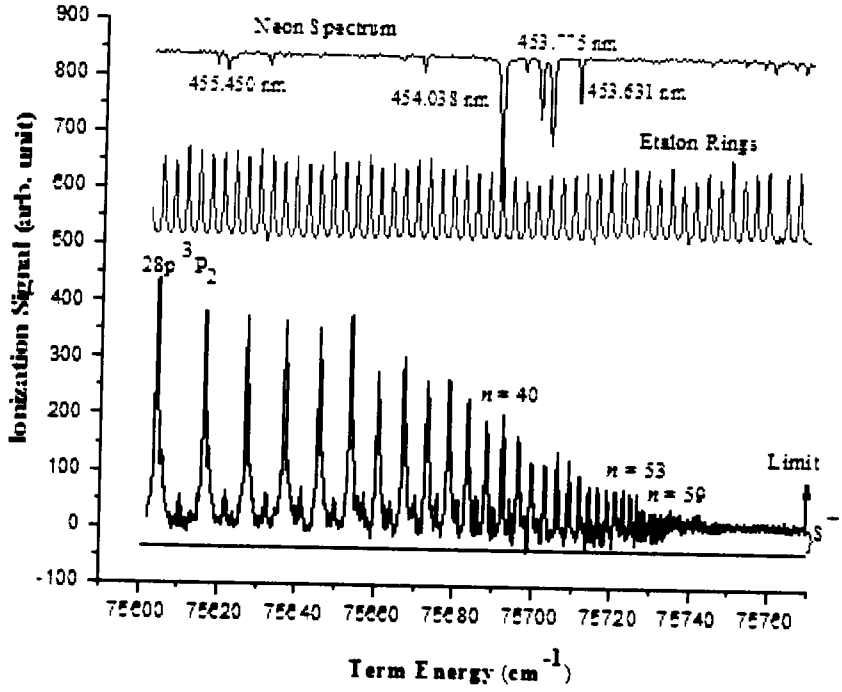

Figure 2.7 The bottom trace is the photoionization signals of zinc from the thermionic diode ion detector as a result of scanning the dye laser in the 75580-75720 cm^{-1} energy range. The middle trace is the etalon rings which serve as frequency marker at each data point and the top trace is the optogalvanic signal from neon filled hollow cathode lamp showing the reference lines for wavelength calibration.

In Figure 2.7 the trace at the top is the optogalvanic spectra of neon, the middle trace is the interference fringes from a 1mm thick solid etalon and the trace at the bottom of the figure is the ionization signal of zinc either from the atomic beam or thermionic diode ion detector.

The level energies of zinc were determined using a computer code that takes into account the neon reference wavelengths and the interference fringes, and yields energies of all the unknown levels.

Chapter 3

Laser excitation studies of 4s*n*f $^1F_3$ Rydberg states of zinc

In this chapter, we present term energies and effective quantum numbers of the odd-parity 4s*n*f $^1F_3$ Rydberg series of zinc from 75480 to 75750 cm^{-1} energy range. The experiment was performed using three dye lasers simultaneously pumped by the second (532 nm) and third harmonic (355 nm) of a Q-switched Nd-YAG laser in conjunction with atomic beam set-up. The new observation include the 4s*n*f $^1F_3$ ($20 \leq n \leq 50$) series excited from the 4s4d $^1D_2$ intermediate level. In addition, the dipole polarizability of the zinc core has been determined as $\alpha_d = 18.33 \pm 0.95\ a_o^3$ using the core polarization model, which is in consistence with the earlier reported experimental and theoretical results.

3.1 Introduction

Zinc is the lightest group II-B element, having atomic number 30. The electronic configuration of zinc consists of completely filled 4s sub shell, similar in configuration with alkaline earth atom calcium. The resonance level 4s4p $^1P_1$ of zinc lie at 46745.413 cm^{-1}, the ultraviolet laser at 213.9 nm is required to populate the level. However, the inter-combination 4s4p$^3P_1$ level at 32501.421 cm^{-1} (λ = 307.68 nm) can be populated comparatively easily by frequency doubling the dye laser for the investigation of highly excited states. Therefore, most of the laser based work on the highly excited states of zinc is reported from the 4s4p $^3P_1$ inter-combination level. Because the 4s4p $^3P_1$ level, located at 32501.399 cm^{-1}[63], can be populated comparatively easily using the frequency doubled dye laser at 307.67 nm.

According to the literature review, the first laser based work on zinc from the 4s4p $^{1,3}P_1$ intermediate states were reported by Kompitsas et al. [7], their observations include 4s*n*f $^{1,3}F_J$ ($8 \leq n \leq 26$), 4s*n*s $^1S_0$ ($14 \leq n \leq 31$), 4s*n*d $^1D_2$ ($12 \leq n \leq 35$) and 4s*n*p ^3P ($10 \leq n \leq 40$) series, using the multi-step and multi photon laser excitation. In addition, the dipole polarizability of zinc core was determined as $\alpha_d = 15.54\ a_o^3$ from the quantum defects of 4s*n*f $^{1,3}F_J$ series using the core polarization model. Later, Nadeem et al. [8] reported the term energies and quantum defects of the 4s*n*p $^3P_2$ ($12 \leq$

$n \leq 60$), 4s*n*p $^1P_1$ ($16 \leq n \leq 30$) and 4s*n*s $^3S_1$ ($19 \leq n \leq 44$) series and the first ionization potential of zinc as 75769.31 ± 0.05 cm^{-1}. Nawaz et al. [9] observed the even parity 4s*n*d $^3D_{1,2,3}$ ($14 \leq n \leq 55$) and 4s*n*s $^3S_1$ ($15 \leq n \leq 35$) series from the 4s4p $^3P_{0,1,2}$ intermediate level using the two-step laser excitation scheme. Eshkobilov [64] reported the term energies and quantum defects of the $^3P_{0,1,2}$ series of Zn, Cd and Hg along with the first ionization potentials. Tukhlibaev and Alimov [65] used the three-step laser excitation scheme for the investigation of the 4s*n*p $^3P_1$ ($5 \leq n \leq 50$) Rydberg states of zinc using the pulsed electric field and determined the first ionization potential as 75769.328 ± 0.018 cm^{-1}.

In the present experimental work, the three step laser excitation scheme was used for the investigation of odd parity 4s*n*f $^1F_3$ ($20 \leq n \leq 50$) Rydberg states of zinc. In addition, the dipole polarizability of the zinc core has been measured as α_d = 18.33 ± 0.95 a_o^3 using the core polarization model.

3.2 Experimental Detail

The experimental set-up is described in chapter-2 Figure 2.1. Since a three-step laser excitation experiment was designed for the investigation of 4s*n*f $^1F_3$ series of zinc. A Q-switched Nd-YAG laser operating at a 10 Hz repetition rate having pulse duration of 7 ns was used as a pump source for dye lasers. The first dye laser was pumped by the third harmonic (355 nm) of the Nd-YAG laser using the Stilbene 420 dye and the beam was focused into a BBO type-II crystal (6 mm long, cut 40° with respect to the optic axis) for the second harmonic generation to excite the 4s4p $^1P_1$ level of zinc at 213.9 nm. The second and third dye lasers were pumped by the second harmonic (532 nm) of the Nd-YAG laser, the second dye laser was fixed at 636.4 nm to populate the 4s4d $^1D_2$ level Gulberg and Litzen [63]. The third dye laser was charged with LDS 750 dye and scanned up to the first ionization threshold. The laser energy of the first dye laser was 0.5 mJ and the energy of the second and third dye laser was ~2 mJ.

The collimated atomic beam of zinc was produced by an oven heated to about 460 °C. The atomic beam of neutral zinc was then crossed between two stainless steel plates 50 × 50 mm^2 in dimension and 10 mm apart, a small voltage of +5V is applied at the lower plate to push the electrons upward. An electron multiplier (channeltron),

configured to collect the ions, was mounted on the upper plate. The three Nd-YAG pumped dye laser beams intersect the atomic beam and the photoelectrons produced in an ionization process were detected orthogonal to the atomic and laser beams. For wavelength calibration three signals from channeltron, hollow cathode and photodiode were simultaneously sampled using three gated integrator boxcar (SR-250) averagers. The SR-245 computer interface module was used for data acquisition. The spectra were recorded and stored on a personal computer using a computer code developed in laboratory.

3.3 Results and Discussion

A three step laser excitation scheme for the investigation of highly excited states is shown in Figure 3.1.

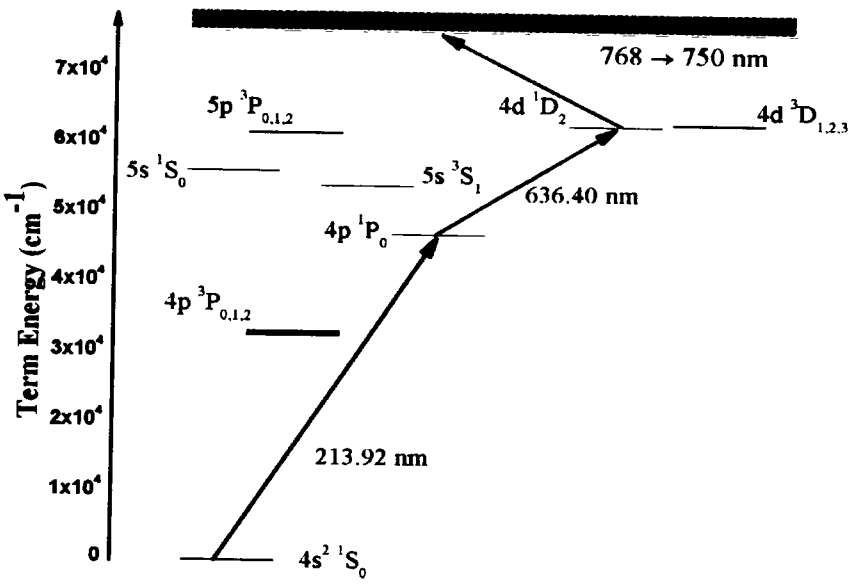

Figure 3.1 Three step laser excitation schemes for the investigation of 4s*n*f $^1F_{2,3,4}$ series.

The first frequency doubled dye laser was fixed at 213.9 nm and the second dye was at 636.4 nm to populate the 4s4p $^1P_1$ and the 4s4d $^1D_2$ state respectively. The third dye laser was scanned from 768 to 750 nm to investigate the highly excited states of zinc. The lifetime of the 4s4d $^1D_2$ level is 20.5 ± 1.5 ns as reported by Martinson et al. [66]. Therefore, the time delay between the dye lasers pulses was not very critical. An

optimum signal was registered when the third dye laser was delayed with respect to the second dye laser by a few ns. The selective excitation process at each step was verified by blocking anyone of the excitation dye laser beams and observing the photo-ionization signal.

$$4s^2\ {}^1S_0 \xrightarrow{213.9nm} 4s4p\ {}^1P_1 \xrightarrow{636.4nm} 4s4d\ {}^1D_2 \xrightarrow{768\text{–}750nm} 4snf\ {}^1F_3$$

The photo-ionization signals excited from the 4s4d $^1D_2$ level observed using the three-step laser excitation scheme is shown in Figure 3.2 for 75480 -75750 cm^{-1} energy range.

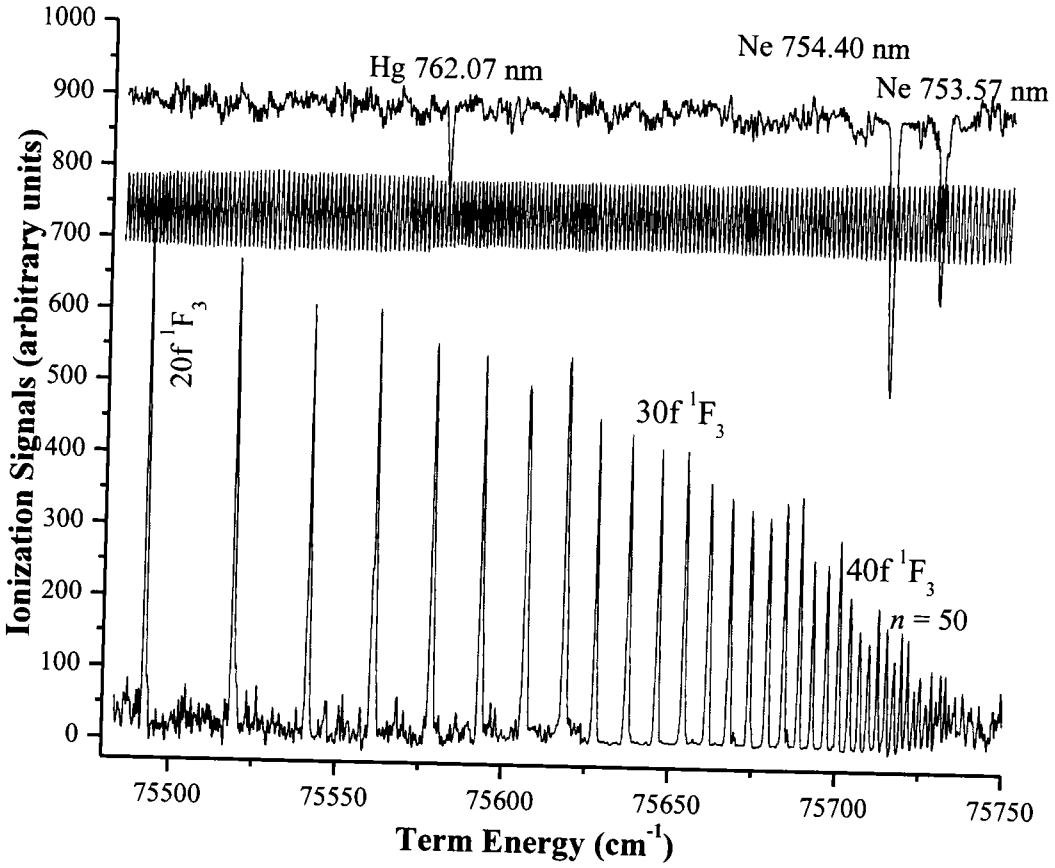

Figure 3.2 The photoionization spectrum of zinc showing the 4s4d $^1D_1 \rightarrow 4snf\ ^1F_3$ Rydberg series from n = 20 to 50.

The upper trace shows the optogalvanic spectra of neon, the middle trace is the interference pattern observed with the etalon and the lowest trace are the photoionization signals of zinc. The accessible series from the 4s4d $^1D_2$ intermediate-state are 4snp $^1P_1$ and 4snf $^1F_3$, according to the LS-coupling scheme. However, in the current experimental studies only one series was detected that is assign as 4snf $^1F_3$ and

the *n*p transition remain too weak to be detected. The 4s*n*f $^1F_3$ series have been recorded from n = 20 to 50 as shown in Figure 3.2. The accurate identification of the 4s*n*f $^1F_3$ series is based on effective quantum numbers extrapolated from lower member of the series for n = 8 - 26 [7] and NIST atomic database [67].

Further, according to the electric dipole selection rules, a transition is more favorable if $\Delta\ell = \Delta L = \Delta J = +1$ therefore, from the 4s4d $^1D_2$ level the most probable transitions are 4s*n*f $^1F_3$. The quantum defect of the 4s*n*f $^1F_3$ series was calculated using the following Rydberg relation:

$$n^* = n - \delta_\ell = \sqrt{\frac{R_{Ryd}}{IP - E_n}} \tag{3.1}$$

here E_n is the transition energy, *IP* is first ionization limit of zinc 75769.31 ± 0.05 cm^{-1} [8], R_{yd} is the mass corrected Rydberg constant for zinc 109736.404 cm^{-1}, and δ_l is the quantum defect. The Table 3.1 consists of the term energies, principal quantum number n and effective quantum number n^* of the 4s*n*f $^1F_3$ Rydberg series. It also contains the term energies of the previously reported work [6, 7]. The term energies determined in the present work are in good agreement with Kompitsas et al. [7] from n = 20 to 26 within reported uncertainty. The line widths of the Rydberg resonances were almost three times larger (~ 1 cm^{-1}) than the line width of our dye laser, ≈ 0.3 cm^{-1} and, it remain almost constant throughout the spectrum. This enhanced line widths of the observed series may be attributed to the Doppler, power and collision broadening. The intermediate level is known to 0.005 cm^{-1} [63], the laser line width is 0.3 cm^{-1}, a single step in the dye laser stepper motor is 0.1 cm^{-1}, the neon reference wavelengths are known within 0.0007 cm^{-1} [67] and the FSR of etalon 3.5 ± 0.05 cm^{-1}. Therefore, the combined uncertainty of the level energies is estimated as 0.25 cm^{-1}.

Figure 3.3 is a plot of principal quantum number n versus the quantum defects δ_l of the 4s*n*f $^1F_3$, series. The quantum defects determined from the higher member series are also consistent with those calculated from the lower members n = 26-32 of the series [6, 7].

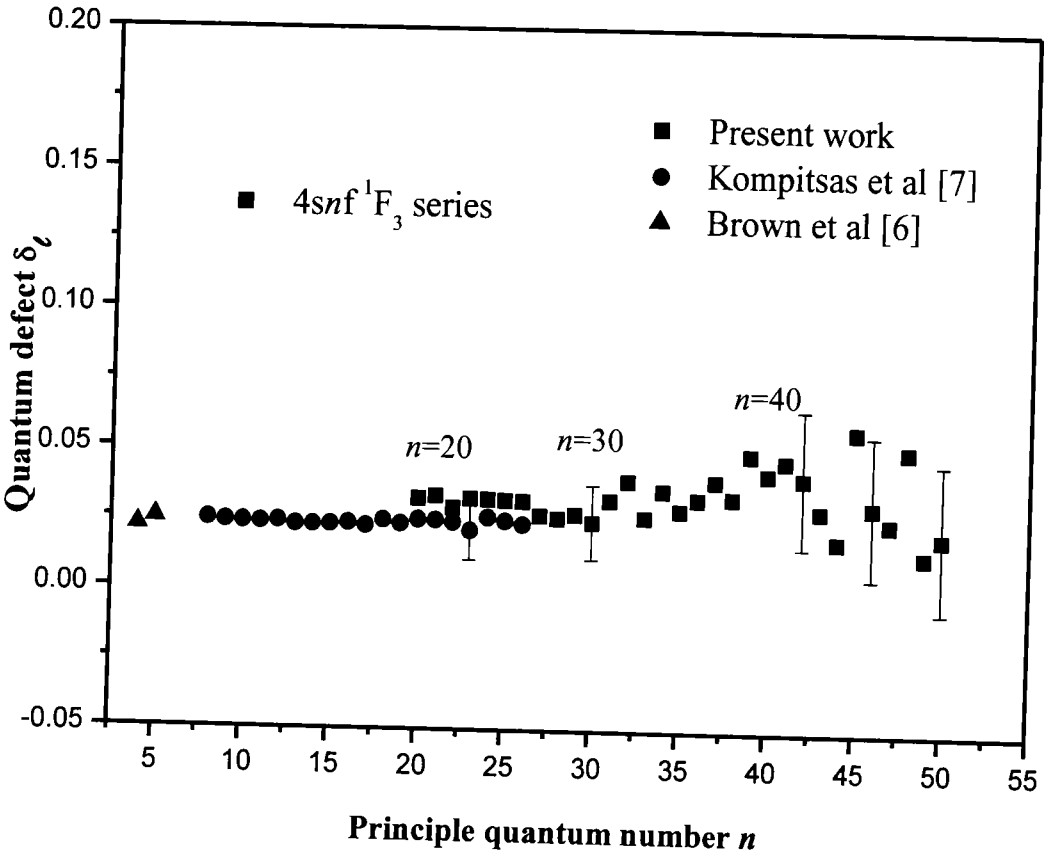

Figure 3.3 The quantum defect δ_ℓ against the principal quantum number n.

However, at higher $n \geq 45$ the small variations in quantum defect is due to the fluctuations in the photoionization spectrum and in the determination of the term energies. The error bars are the experimental uncertainty in the determination of term energies i.e., 0.25 cm^{-1}. Furthermore, for the high Rydberg states, the relative accuracy of the small difference IP-E_n decreases markedly with increasing n and this is reflected in the increase errors in quantum defect δ_l. The quantum defects of the 4snf $^1F_3$ Rydberg series of zinc do not show any strong variations as a function of the principal quantum number. The levels that might perturb this series are either attached to double excitation or inner-shell excitations.

Finally, the dipole polarizability α_d of the zinc core is determined using the core polarization model as described in section 1.5. In the core polarization model the excited electron and the positive core are coupled by the central electrostatic potential for the high principal quantum number n and high orbital angular momentum $\ell \geq 3$. This model has been applied by several authors [29 - 31] for the determination of dipole polarizability under certain approximation i.e., in the absence of quadruple

polarizability α_q and the core penetration effects, the term energy $E_{(n,\ell)}$ and the ionization potential (IP) of the non-penetrating hydrogenlike system can be written as,

$$IP - E_{(n,\ell)} = T_{(n,\ell)} + \Delta W_{pol(n,\ell)} \tag{3.2}$$

where $T_{(n,\ell)}$ is the term energy in hydrogenic form:

$$T_{(n,\ell)} = \frac{Z^2 R_{yd}}{n^2}\left[1 + \left(\frac{\alpha Z}{n}\right)^2\left(\frac{n}{\ell+\left(\frac{1}{2}\right)} - \left(\frac{3}{4}\right)\right)\right] \tag{3.3}$$

here, Z is the net charge of the nucleus and core electrons, R_{yd} is the Rydberg constant, n is the principal quantum number, ℓ is the orbital angular momentum, α is the fine structure constant and a_o = 0.529 Å is the Bohr radius. The $\Delta W_{pol\,(n,l)}$ is the perturbation in energy due to the core polarization.

$$\Delta W_{\,pol\,(n,\ell)} = R_{yd}\, a_o\left[\alpha_d \langle r^{-4}\rangle_{n,\ell} + \alpha_q \langle r^{-6}\rangle_{n,\ell}\right], \tag{3.4}$$

where $\langle r^{-4}\rangle_{(n,\ell)}$ and $\langle r^{-6}\rangle_{(n,\ell)}$ are radial coordinate in the hydrogen like system [32]. The α_d and α_q are the dipole and quadruple polarizabilities in units of a_o^3 and a_o^5 respectively, substituting equation (3.4) in equation (3.2) and re-arranging, we obtain the following relation;

$$\frac{IP - E_{(n,\ell)} - T_{(n,\ell)}}{R_{yd} a_o \langle r^{-4}\rangle_{(n,\ell)}} = \alpha_d + \alpha_q\left(\frac{\langle r^{-6}\rangle_{(n,\ell)}}{\langle r^{-4}\rangle_{(n,\ell)}}\right), \tag{3.5}$$

The accurate values of the term energies of the non-penetrating $n\,{}^1F_3$ series (present work) and incorporating the $n{}^1G_4$ values as reported in [31] were used for the measurement of the dipole polarizability of Zn^+. The plot of the left side of equation (3.5) versus $\langle r^{-6}\rangle_{(n,\ell)}/\langle r^{-4}\rangle_{(n,\ell)}$ is a polarization graph as shown in Figure 3.4. The y-intercept gives the value of dipole polarizability as α_d = 18.33 ± 0.95 a_o^3. The uncertainty in the dipole polarizability is due to the uncertainty in term energies and in the ionization potential. The inset in Figure 3.4 represents our data of the 4s*n*f ${}^1F$ series from n = 20-50.

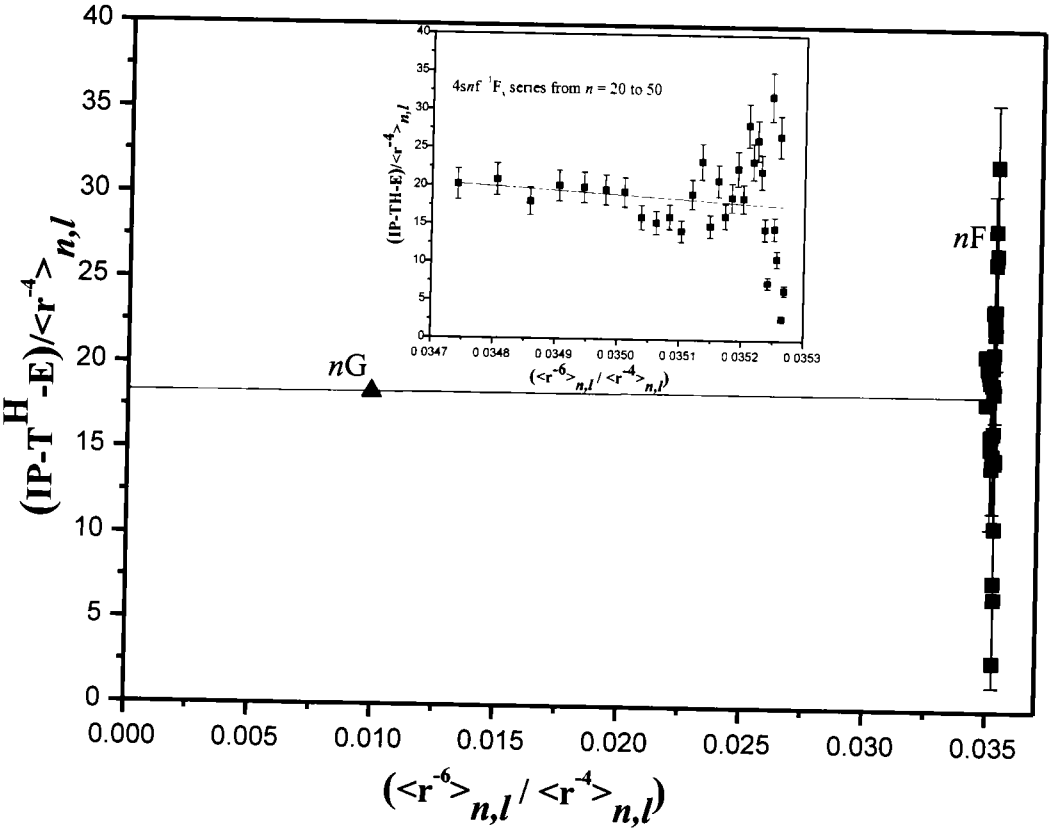

Figure 3.4 The plot of the left side of equation (3.5) versus the $\langle r^{-6}\rangle_{(n,\ell)}/\langle r^{-4}\rangle_{(n,\ell)}$ for the F (squares) and G states (triangles).

Recently, Kutsenko et al. [31] estimated the dipole polarizability using the quantum defects of the F and G states of zinc as 18.36 ± 0.4 a_o^3. Ilias and Neogrady [30] reported the dipolepolarizability of Zn^+ core as 18.84 a_o^3 using the correlation model and relativistic effects. Laughlin [29] developed a ℓ-electron model of Zn^+ to evaluate the long-range asymptotic form of the polarization potential for the electron interacting with Zn^+ core, and deduce the dipole polarizability as 16.7 a_o^3 and 20.8 a_o^3. Our value of the dipole polarizability is in good agreement with above mentioned experimental and computational values within uncertainty. Whereas, Kompitsas et al. [7] estimated the dipole polarizability as α_d = 15.54 ± 0.81 a_o^3 from the quantum defect of the 4s*n*f series, using the Vleck and Whitelaw [68] model. In this model all the polarizability arises due to the 4s electron, neglecting the contribution from the $3d^{10}$ closed shell. Subsequently, Curtis and Theodosiou [25] used the results of Kompitsas et al. [7] for the 4s*n*f series and theoretically deduced the dipole polarizability as α_d = 15.5 ± 0.5 a_o^3 with reduced uncertainty incorporating the quadruple polarization. The detail spectroscopic data of the 4s*n*g states is still not

available; therefore, it is not possible to precisely determine the dipole polarizability of zinc.

In conclusion, we report new experimental results on the term energies and effective quantum numbers of the 4s*n*f $^1F_3$ Rydberg states of zinc from n = 20 to 50 using the three step laser excitation scheme, excited from the 4s4d $^1D_2$ intermediate level. The dipole polarizability of the Zn^+ core has been determined as $\alpha_d = 18.33 \pm 0.95\ a_o^3$ using the core polarization model which is in good agreement with previously reported experimental and theoretical values.

n	Term energy (cm^{-1})	n^*
29	75638.6	28.975
30	75647.2	29.978
31	75654.9	30.970
32	75661.9	31.963
33	75668.4	32.977
34	75674.2	33.967
35	75679.6	34.975
36	75684.5	35.971
37	75689.0	36.965
38	75693.2	37.971
39	75697.0	38.956
40	75700.6	39.964
41	75703.9	40.959
42	75707.0	41.966
43	75709.9	42.978
44	75712.6	43.989
45	75715.0	44.951
46	75717.4	45.978
47	75719.6	46.984
48	75721.6	47.959
49	75723.6	48.997
50	75725.4	49.991

Chapter 4

Three-step-wise laser excitation of the 4snf ^{3}F highly excited states of zinc

In this chapter, effective quantum number and term energies of the highly excited odd-parity 4s4d $^3D_{1,2,3}$→ 4s*n*f $^3F_{2,3,4}$ Rydberg states of zinc have been presented. The experiment was performed using the three dye lasers simultaneously pumped by the second harmonic (532 nm) of the Q-switched Nd: YAG laser. The new observation include the 4s*n*f $^3F_3$ ($12 \leq n \leq 50$) series excited from the 4s4d $^3D_2$ intermediate level. In addition, the 4s*n*f $^3F_2$ ($12 \leq n \leq 28$) and 4s*n*f $^3F_4$ ($12 \leq n \leq 33$) series were also observed from the thermally populated 4s4d $^3D_{1,3}$ fine structure components. The ionization potential of zinc has been determined from the unperturbed 4s*n*f $^3F_3$ series as 75769.31 ± 0.15 cm^{-1}, which is in excellent agreement with the previously reported value.

4.1 Introduction

The aim of the present investigation was to investigate the high orbital angular momentum (ℓ = 3) states of zinc using multi-step laser excitation scheme from the 4s4p^{3}D multiplet. To our knowledge, the only laser based work on the bound states 4s*n*f $^{1,3}F_J$ of zinc was reported by Kompitsas et al. [7] from n = 8 to n = 26 using the multi-photon laser excitation scheme. Subsequently, most of the laser based work on the triplet 4s*n*p and 4s*n*d states of zinc was reported by [8, 9].

Although the first systematic studies on the bound state of Zn I and Cd I were reported by Brown et al. [6]. In zinc they reported the principal series 4s^2 $^1S_0$→ 4s*n*p $^1P_1$ ($4 \leq n \leq 66$), the electric quadrupole transitions 4s^2 $^1S_0$ → 4s*n*d $^1D_2$ ($4 \leq n \leq 20$) and the inter-combination transitions 4s^2 $^1S_0$ → 4s*n*p $^3P_1$ ($4 \leq n \leq 12$). The first ionization limit of zinc was reported as 75769.33 ± 0.18 cm^{-1} from the much extended 4s*n*p $^1P_1$ Rydberg series. Martinson et al. [66] reported the lifetimes for the low-lying levels of Zn I and Zn II using the beam-foil technique. Sugar and Musgrove [69] have compiled all the available data of the atomic energy levels of zinc form Zn I through Zn XXX. Gullberg and Litzen [63] reported the accurately measured wavelengths of Zn I and Zn II lines of astrophysical interest with a Fourier transform spectrometer using a hollow cathode as a light source. On the basis of the solar data and multi-configuration Hartree Fock

(MCHF) calculation the abundance of zinc has been determined for astrophysical interest [70].

In this paper, the detail investigation of the 4s*nf* $^3F_3$ ($12 \leq n \leq 50$), 4s*nf* $^3F_2$ ($12 \leq n \leq 28$) and 4s*nf* $^3F_4$ ($12 \leq n \leq 33$) Rydberg states have been presented. The first ionization potential of zinc has been determined from the much extended 4s*nf* $^3F_3$ Rydberg series as 75769.31 ± 0.15 cm^{-1} using the Rydberg-Ritz relation.

4.2 Experimental Detail

A schematic diagram of the experimental set-up is shown in Figure 4.1. The first frequency doubled dye laser was fixed at 307.38 nm, operated with Rhodamine-610 dye dissolved in methanol to populate the 4s4p $^3P_1$ level.

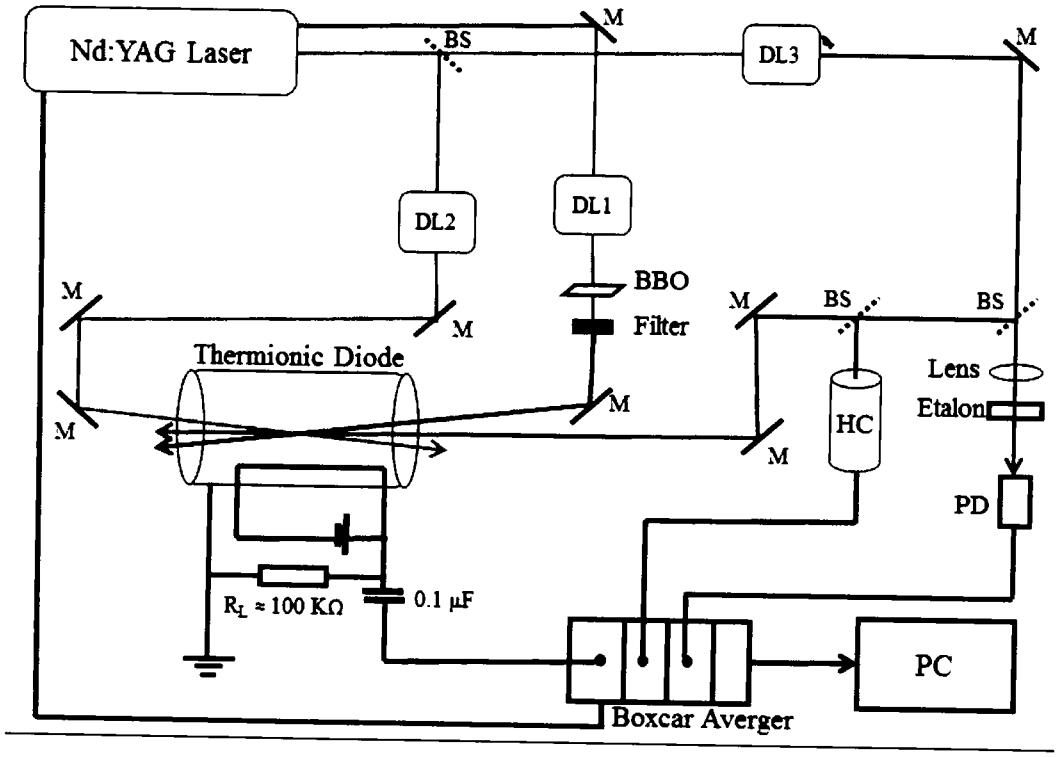

Figure 4.1 Schematic diagram of the three-step experimental set up.

The second dye laser was charged with DCM dye dissolved in methanol and frequency doubled to populate the 4s4d $^3D_2$ level at 330.35 nm. Frequency doubling of both the dye lasers were achieved by focusing the laser into Beta Barium Borate (BBO) type-I crystals (6 mm long, cut at 40° with respect to optic axis).

The third dye laser was operated with LDS-798 dye dissolved in methanol and was scanned from 867 - 825 nm range. The pulse energies of the dye lasers are ≈ 10-50 μJ depending on the wavelength. All the three dye laser beams were linearly polarized and spatially overlapped in the middle of the thermionic diode ion detector. The zinc vapors were confined in a thermionic diode ion detector working in the space charge limited mode as described in chapter 2. The temperature was kept at about 820 ± 2% Kelvin and it was maintained through a nickel-chromium-nickel (Ni-Cr-Ni) thermocouple. About 5 grams of zinc along with a small amount of potassium (to reduce the work function of the cathode) was placed in the middle, the argon pressure was varied from 3 and 10 mbar.

4.3 Result and Discussion

Three-step laser excitation scheme to investigate the odd-parity states of zinc is shown in Figure 4.1.

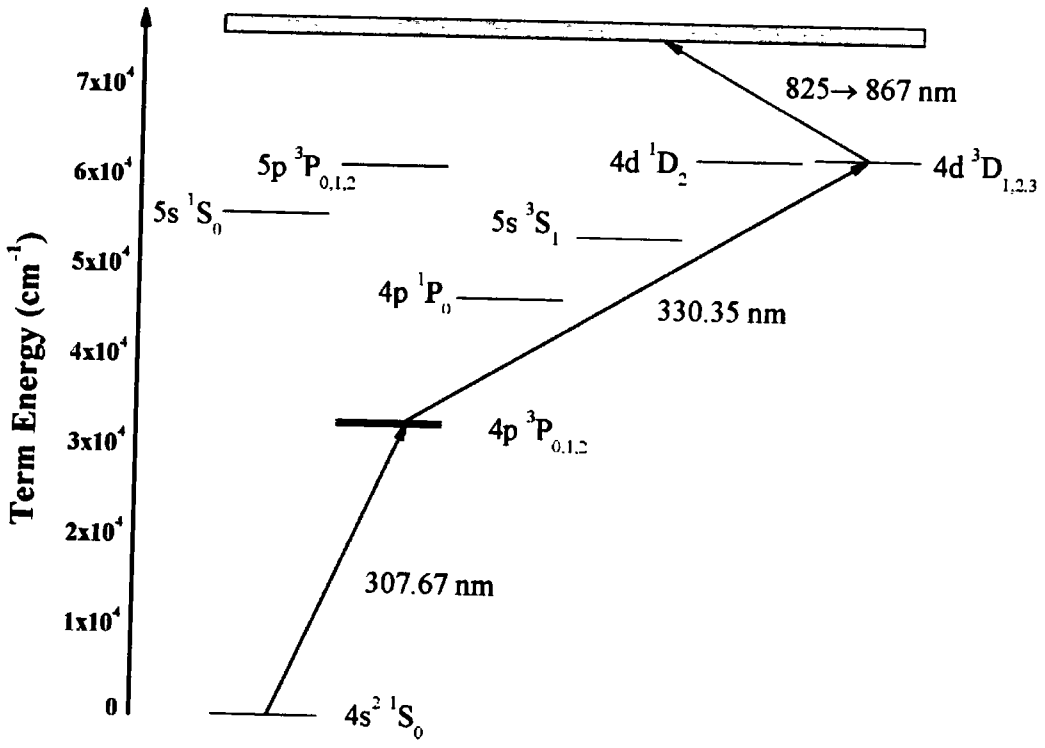

Figure 4.2 The three-step laser excitation scheme used to investigate the odd-parity states of zinc.

The first dye laser was fixed at 32501. 399 cm^{-1} to populate the 4s4p $^3P_1$ intermediate level, the second dye laser was fixed at 62772. 014 cm^{-1} to populate the 4s4d $^3D_2$ level

and the third laser was scanned from 867 nm to 825 nm ranges up to the first ionization threshold. The life time of the 4s4d $^3D_2$ level is 5.4 ± 0.6 ns [66] therefore; the third dye laser was fed into the thermionic diode without any delay. The selective excitation process at each step was ensured by blocking any of the excitation beams and monitoring the corresponding ion signal.

$$4s^{2\,1}S_0 \xrightarrow{307.38nm} 4s4p^3P_1 \xrightarrow{330.35nm} 4s4d^3D \xrightarrow{867\text{-}825nm} 4snf^3F$$

Since the first dye laser is linearly polarized, the populated state in the 4s4p $^3P_1$ level is $m_j = 0$. The second dye laser is also linearly polarized with the polarization vector parallel to the first step laser and it was tuned to populate the 4s4d ^3D triplet were $m_j = 0$. In the third excitation step, the atoms from the 4s4d $^3D_{1,2,3}$ levels have been promoted to the 4s*n*f $^3F_{2,3,4}$ levels. The transitions were observed from all the three fine structure components; 4s4d $^3D_{1,2,3}$ despite the third laser was tuned from the 4s4d $^3D_2$ level. In Figure 4.3, a portion of zinc spectrum is shown covering the term energy range from 75240-75506 cm^{-1} excited from the 4s4d^{3}D multiplet.

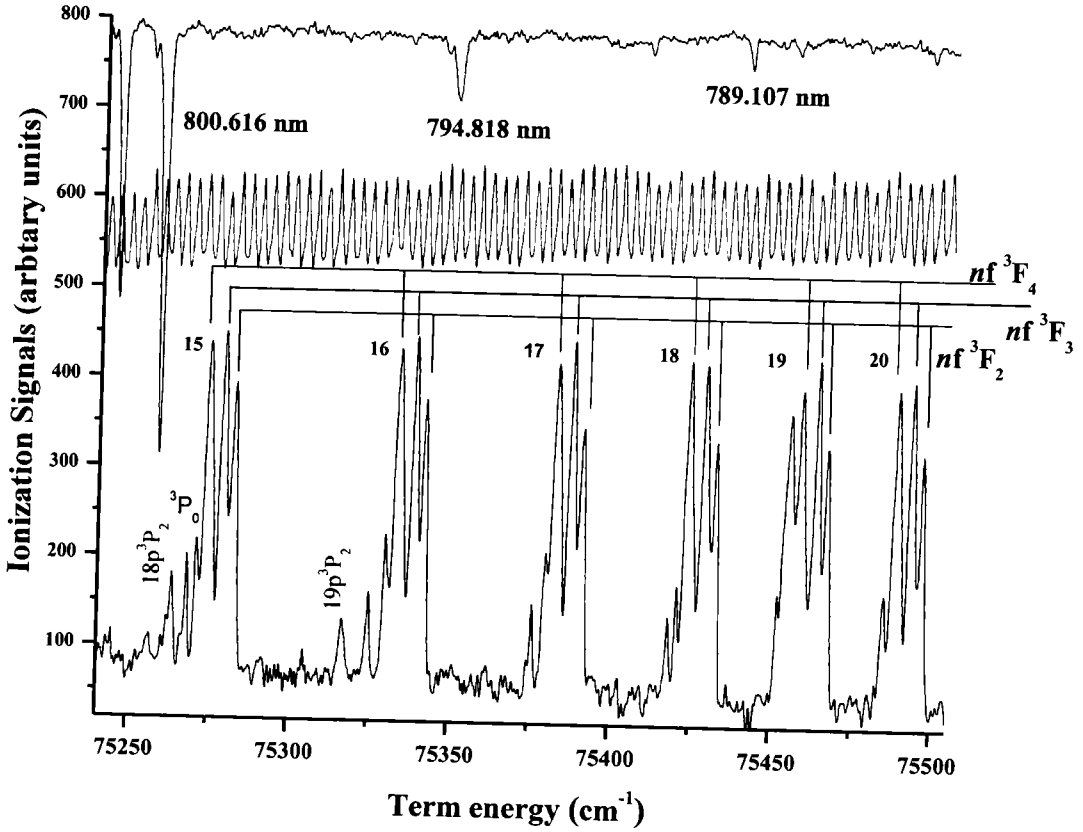

Figure 4.3 The 4s*n*f $^3F_{2,3,4}$ Rydberg states of zinc from n = 15 to 20.

The top trace is the optogalvanic spectra of argon for wavelength calibration and the middle are the interference fringes from a 1-mm thick solid etalon and the bottom trace is the ionization signals of zinc. This portion of the spectrum looks a bit complicated due to the presence of all the possible excitations from the 4s4d $^3D_{1,2,3}$ intermediate levels. The thermal energy of the zinc atoms in the thermionic diode is ~ 570 cm^{-1} corresponding to the 820 K temperature, therefore, all the fine structure components 4s4d $^3D_{1,2,3}$ also got populated due to the thermal energy collision. Consequently, we observed all the allowed transitions from the 4s4d ^3D multiplet to the 4s*n*f $^3F_{2,3,4}$ levels in the present work. The accessible series from the 4s4d $^3D_{1,2,3}$ intermediate levels are 4s*n*f $^3F_{2,3,4}$ and 4s*n*p $^3P_{0,1,2}$ according to the electric dipole selection rules ($\Delta\ell = \pm 1$, $\Delta J = 0 \pm 1$, $0 \leftrightarrow 0$ forbidden). The 4s*n*f $^3F_{2,3,4}$ Rydberg levels were observed with good intensity, whereas, a few lines of the 4s*n*p $^3P_{0,1,2}$ series have also been detected. The relatively high intensity series is assigned as 4s*n*f $^3F_3$ ($15 \leq n \leq 20$) excited from the 4s4d $^3D_2$ intermediate level. The adjacent series at the lower energy side of the main series is identified as 4s*n*f $^3F_4$ ($15 \leq n \leq 20$) excited from the 4s4d $^3D_3$ level and the lines on the higher energy side are identified as 4s*n*f $^3F_2$ series ($15 \leq n \leq 20$) excited from the 4s4d $^3D_1$ level.

The assignments of these series are in accordance to the electric dipole selection rules, following the electric dipole intensity selection rules the more favorable transitions are which follow the $\Delta\ell = \Delta L = \Delta J = +1$ selection rules. Therefore, from the 4s4d $^3D_2$ intermediate level the most probable transitions are 4s*n*f $^3F_3$. Similar arguments are valid for the 4s*n*f $^3F_4$ and 4s*n*f $^3F_2$ series. The relative intensities of the 4snf $^3F_{2,4}$ series also reflect the relative populations of the 4s4d $^3D_3$ and 4s4d $^3D_1$ intermediate levels as these were thermally or collisionally populated. Furthermore, it is noticed that the energy separation among the main 4s*n*f $^3F_3$ series and the adjacent series on the lower as well as higher energy side remain constant. These spacing are in accordance with the energy separation between the fine structure components of the 4s4d ^3D multiplets; $^3D_3$ - $^3D_2$ = 4.967 cm^{-1} and $^3D_2$ - $^3D_1$ = 3.267 cm^{-1} as reported by Gullberg and Litzen [63]. The constant energy separations among the observed series enabled us to assign these series unambiguously. The other adjacent Rydberg series possessing lower intensity are assign as 4s*n*p $^3P_{0,1,2}$ which are excited from the

4s4d $^3D_{1,2,3}$ multiplets. The 4s18p $^3P_{1,2}$ and 19p levels are resolved and the 4s4p $^3P_0$ series appears as shoulder to the main 4s15f $^3F_4$ series and almost merge at 17f.

In Figure 4.4 the higher members of the Rydberg series of zinc observed in the 75450 - 75800 cm^{-1} energy range up to the first ionization threshold. The upper spectra were recorded at a relatively higher pressure ≈ 10 mbar of the buffer gas, in this case all the fine structure components of 4s*n*d $^3D_{1,2,3}$ got populated due to the collisional energy transfer. The bottom trace was recorded at a reduced pressure ≈ 3 mbar, in this case the excitation spectra are observed only from the 4s*n*d $^3D_2$ intermediate state. The 4s*n*f $^3F_3$ series has been followed up to n = 50. The 4s*n*f $^3F_4$ and 4s*n*f $^3F_2$ series appears as shoulders to the dominating 4s*n*f $^3F_3$ series and have been resolved up to n = 28 and n = 32 respectively.

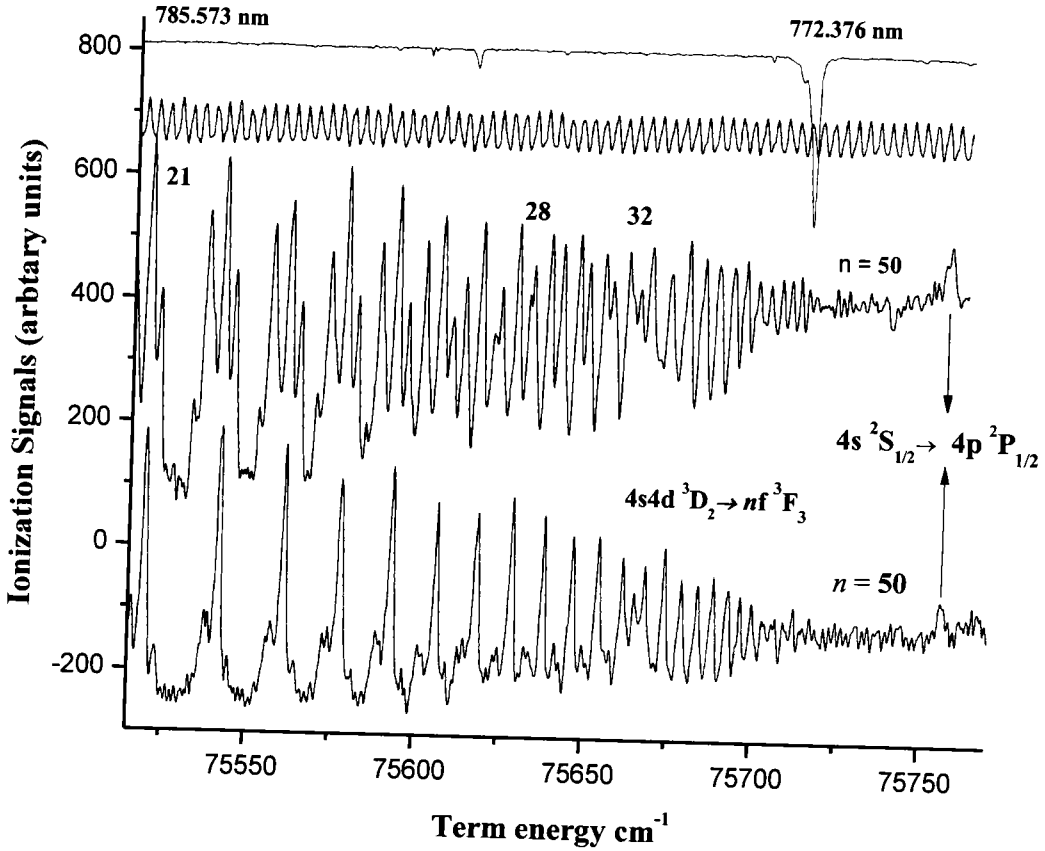

Figure 4.4 The photoionization spectrum of zinc covering the energy range 75450–75800 cm^{-1} at different pressures.

The term energies of all these observed Rydberg series have been determined by adding the excitation laser energies to the energies of the intermediate 4s4d $^3D_{1,2,3}$

levels as listed in [69]. In the present study the 4s*n*f ^{3}F series are extended up to a much higher *n*-value. The 4s*n*f $^3F_3$ series has been observed up to $n = 50$, therefore Rydberg-Ritz formula was used on the experimentally determined term energies to determine the first ionization potential of zinc and the corresponding quantum defects:

$$E_n = E_i - \frac{R_{yd}}{\left[n - a\frac{b}{(n-a)^2} - \frac{c}{(n-a)^4} - .....\right]^2} \qquad (4.1)$$

The mass corrected Rydberg constant R_{yd} is determined as:

$$R_{yd} = R_\infty (1 + m / M_{Zn})^{-1} = 109736.404\ cm^{-1}$$

The δ_ℓ is the quantum defect and a, b, and c are the Rydberg-Ritz coefficients:

$$\delta_\ell = a + \frac{b}{(n-a)^2}. + \frac{c}{(n-a)^4} ..... \qquad (4.2)$$

A least square fit on the transition energies of the 4s*n*f $^3F_3$ series yields the binding energies as 12997.29 ± 0.02 cm^{-1}, and the Ritz coefficients a = 0.0317, b = 1.3324 and c = -290.4811. By adding the binding energy 12997.29 ± 0.02 cm^{-1} in the energy of the 4s4d $^3D_2$ level 62772.014 cm^{-1} [69], the first ionization potential of zinc is determined as 75769.31 ± 0.15 cm^{-1}, this is in excellent agreement with the previously reported value [9]. The Ritz coefficients a, b and c were substituted in equation 4.2 and quantum defect was determined as 0.029 ± 0.005. For the verification of the experimentally determined term energies, the term energies were also calculated using the Rydberg-Ritz coefficients using equation 4.1 as listed in the 12th column of Table-4.1. The Table-4.1 consists of the term energies, principal quantum number *n* and effective quantum number *n** of the 4s*n*f $^3F_{2,3,4}$ Rydberg series. It also contains the term energies of the previously reported work [7, 69], and the difference in $E_{(experimental)} - E_{(calculated)}$ term energies of the 4s*n*f $^3F_3$ series. Figure 4.5 shows the plot of the $E_{(experimental)} - E_{(calculated)}$ versus the principle quantum number *n*, the energy difference is well within the quoted uncertainty in the present work. The last member of the 4s*n*f $^3F_3$ series was observed up to $n = 50$, and lies only 30 cm^{-1} below the ionization limit. The Rydberg states can be further extended close to the ionization limit by minimizing the electric field in the detector and by using a narrow line width

dye laser. Furthermore, it is observed that the line widths of the 4s4d $^3D_2 \rightarrow$ 4snf $^3F_3$ transitions of zinc are approximately 1.8 (2) cm^{-1}, which is larger than the line width of our dye laser, ≈ 0.3 cm^{-1}.

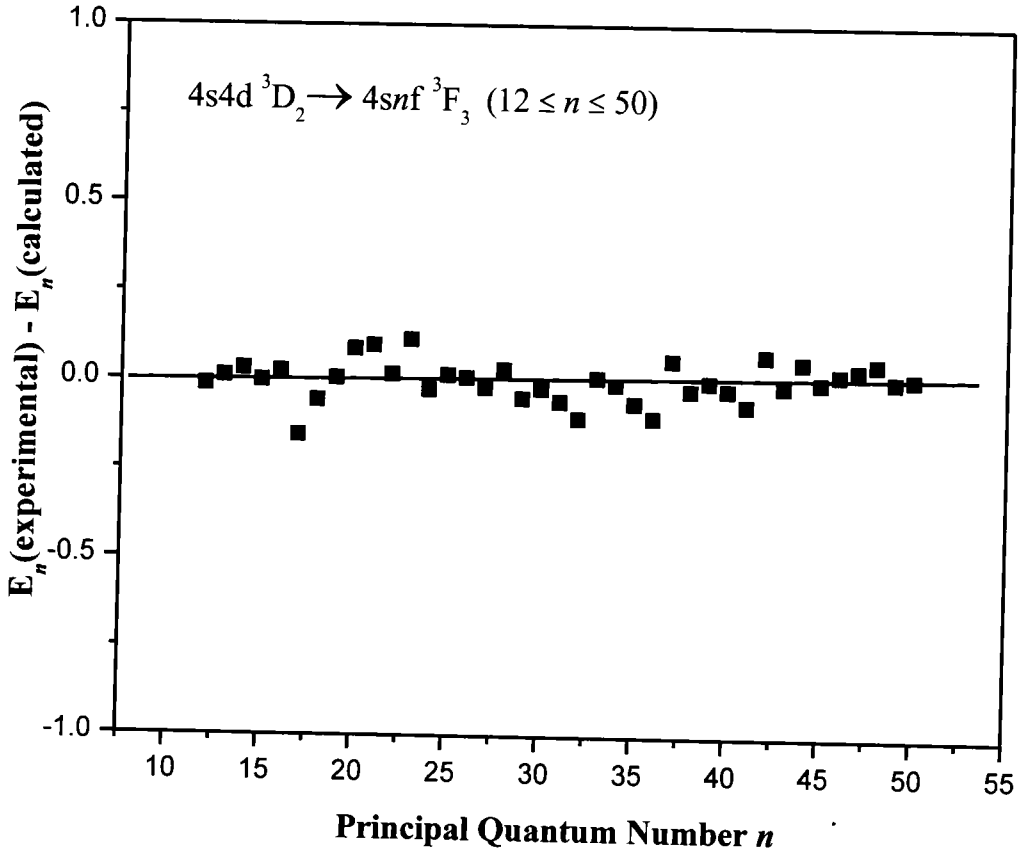

Figure 4.5 The plot of difference in term energies E_n(experimental) – E_n(calculated) (within the quoted uncertainty in term energy ± 0.25 cm^{-1}) versus principal quantum number n.

This enhanced line widths are due to many factors in the experimental work, such as the Doppler, collisional, pressure and Stark broadening. In addition, at higher n all the components of 4snf $^3F_{2,3,4}$ multiplet starts merging and consequently the transitions are broadened. The analysis of the observed 4snf $^3F_{2,3,4}$ series reveals that the quantum defects are almost constant as a function of principal quantum number n. Since the levels that might perturb the triplet discrete structure are either attached to the double excitation or inner-shell excitations. In zinc all the doubly excited states based on the $4p^2$ configuration or due to the 3d-subshell excitation that lie above the first ionization threshold consequently, the series perturbations are negligible. Whereas, in the homologous element calcium the doubly excited configurations 3d5s and $3d^2$ $^1D_2$ lie below the threshold which perturb the principle series Esherick et al. [71]. Therefore,

it is suggested that the unperturbed *n*f-series in zinc, cadmium and mercury are the best candidates for the determination of the first ionization potential of these elements.

The estimated uncertainties in the term energies are ± 0.25 cm^{-1} over the whole spectral range. The intermediate level is known to 0.02 cm^{-1} [69], the laser line width is ≤ 0.3 cm^{-1}, and the reference wavelengths are known within 0.0001 nm [67] and in the measurement of FSR 100 ± 0.01 GHz and a single step in the scanning dye laser stepper motor is 0.04 cm^{-1} therefore from the location of the peak signal positions the term energies have been determined within the above mentioned accuracy. The term energies were determined using a subroutine that takes into account the neon reference wavelengths and the interference fringes from the etalon and yields energies of all the unknown levels.

In conclusion, the high orbital angular momentum ($\ell = 3$) states of zinc 4s*n*f $^3F_3$ have been investigated for the first time up to much higher principal quantum number n = 50. Furthermore, the 4s*n*f $^3F_2$ and 4s*n*f $^3F_4$ series were observed up to n = 28 and n = 33 respectively from the 4s*n*d $^3D_{1,3}$ thermally populated states in thermionic diode ion detector. Having observed the transitions from all the fine structure components of the 4s4d ^3D multiplet the *J*-values assignment has been made explicitly. Prior to this studies the only available data on the high orbital angular momentum studies ($\ell = 3$) states of 4s*n*f $^{1,3}F_3$ states from the n = 8 to n = 26. Therefore, the present experimental work has extended the previous investigations of the 4s*n*f $^3F_{2,3,4}$ states of zinc. The accurate wavelengths of the above mentioned results of zinc are valuable for the investigation of dynamics of stellar atmosphere. Moreover, using the accurate laboratory scale data of zinc the signature of zinc in solar and stellar atmosphere can be determined.

Table 4.1 The term energies (± 0.25 cm^{-1}) and effective quantum number (n^*) of the 4snf $^3F_{2,3,4}$ Rydberg series observed in the current work. The data of the term energies and the effective quantum number n^* from n = 8-26 reported by Kompitsas et al. [7] and by Sugur and Musgore [69] from n = 4-7 are also listed. The term energy calculated using Rydberg-Ritz relation and in the last column difference between calculated and experimental values.

	$4s4d^3D_2 \rightarrow 4snf^3F_3$		$4s4d^3D_2 \rightarrow 4snf^3F_4$		$4s4d^3D_2 \rightarrow 4snf^3F_2$		Kompitsas et al. [7]		Sugur and Musgore [69]		$4s4d^3D_2 \rightarrow 4snf^3F_3$	$4s4d^3D_2 \rightarrow 4snf^3F_3$
n	Term energy	n^*	Term energy	n^*	Term energy	n^*	Term energy	n^*	Term energy	n^*	Term energy $E_{calc.}$	$E_{Expt.}-E_{calc.}$
4	-	-	-	-	-	-	-	-	68833.93	3.978	-	-
5	-	-	-	-	-	-	-	-	71335.6	4.975	-	-
6	-	-	-	-	-	-	-	-	72690.8	5.970	-	-
7	-	-	-	-	-	-	-	-	73499.5	6.953	-	-
8	-	-	-	-	-	-	74044.1	7.975	-	-	-	-
9	-	-	-	-	-	-	74407.3	8.976	-	-	-	-
10	-	-	-	-	-	-	74666.7	9.976	-	-	-	-
11	-	-	-	-	-	-	74858.5	10.976	-	-	-	-
12	75003.84	11.973	75003.73	11.972	75003.84	11.973	75004.2	11.976	-	-	75003.85	-0.01
13	75117.07	12.971	75117.1	12.971	75117.06	12.971	75117.7	12.977	-	-	75117.06	0.01
14	75207.00	13.969	75206.98	13.969	75206.97	13.969	75207.6	13.977	-	-	75206.97	0.03
15	75279.53	14.968	75279.83	14.973	75279.73	14.971	75280.1	14.977	-	-	75279.53	-0.00
16	75338.95	15.968	75339.08	15.970	75338.9	15.967	75339.4	15.976	-	-	75338.92	0.03
17	75387.99	16.964	75388.18	16.968	75388.06	16.965	75388.6	16.977	-	-	75388.14	-0.15
18	75429.33	17.965	75429.44	17.968	75429.48	17.969	75429.7	17.975	-	-	75429.39	-0.06
19	75464.29	18.967	75464.27	18.966	75464.19	18.964	75464.6	18.977	-	-	75464.28	0.01
20	75494.16	19.970	75494.21	19.972	75494.25	19.973	75494.3	19.975	-	-	75494.07	0.09
21	75519.80	20.971	75519.72	20.967	75519.69	20.966	75519.9	20.975	-	-	75519.70	0.10
22	75541.93	21.968	75542.05	21.973	75541.82	21.962	75542.1	21.976	-	-	75541.91	0.02
23	75561.40	22.973	75561.39	22.972	75561.34	22.970	75561.5	22.978	-	-	75561.29	0.11

n	$4s4d^3D_2 \rightarrow 4snf^3F_3$		$4s4d^3D_2 \rightarrow 4snf^3F_4$		$4s4d^3D_2 \rightarrow 4snf^3F_2$		Kompitsas et al. [7]		Sugur and Musgore [69]		$4s4d^3D_2 \rightarrow 4snf^3F_3$	$4s4d^3D_2 \rightarrow 4snf^3F_3$
	Term energy	n^*	Term energy	n^*	Term energy	n^*	Term energy	n^*	Term energy	n^*	Term energy $E_{calc.}$	$E_{Expt.}-E_{calc.}$
24	75578.26	23.965	75578.39	23.973	75578.31	23.968	75578.4	23.974	-	-	75578.28	-0.02
25	75593.30	24.968	75593.23	24.963	75593.29	24.967	75593.4	24.975	-	-	75593.28	0.02
26	75606.59	25.968	75606.53	25.963	75606.59	25.967	75606.7	25.976	-	-	75606.58	0.01
27	75618.41	26.965	75618.48	26.971	75618.64	26.986	-	-	-	-	75618.43	-0.02
28	75629.06	27.970	75629.06	27.970	75629.06	27.970	-	-	-	-	75629.03	0.03
29	75638.50	28.962	75638.57	28.969	-	-	-	-	-	-	75638.55	-0.05
30	75647.11	29.965	75647.1	29.963	-	-	-	-	-	-	75647.13	-0.02
32	75661.84	31.952	75661.96	31.969	-	-	-	-	-	-	75661.94	-0.10
33	75668.37	32.969	75668.24	32.947	-	-	-	-	-	-	75668.36	0.01
34	75674.21	33.966	-	-	-	-	-	-	-	-	75674.22	-0.01
35	75679.52	34.956	-	-	-	-	-	-	-	-	75679.58	-0.06
36	75684.40	35.946	-	-	-	-	-	-	-	-	75684.50	-0.10
37	75689.09	36.982	-	-	-	-	-	-	-	-	75689.03	0.06
38	75693.18	37.962	-	-	-	-	-	-	-	-	75693.20	-0.02
39	75697.06	38.967	-	-	-	-	-	-	-	-	75697.06	0.00
40	75700.6	39.96	-	-	-	-	-	-	-	-	75700.63	-0.02
41	75703.8	40.95	-	-	-	-	-	-	-	-	75703.94	-0.06
42	75707.1	41.99	-	-	-	-	-	-	-	-	75707.02	0.08
43	75709.8	42.96	-	-	-	-	-	-	-	-	75709.89	-0.01
44	75712.6	43.99	-	-	-	-	-	-	-	-	75712.56	0.06
45	75715.1	44.96	-	-	-	-	-	-	-	-	75715.06	0.00
46	75717.4	45.97	-	-	-	-	-	-	-	-	75717.39	0.03
47	75719.6	46.99	-	-	-	-	-	-	-	-	75719.58	0.04
48	75721.7	47.99	-	-	-	-	-	-	-	-	75721.64	0.05
49	75723.6	48.97	-	-	-	-	-	-	-	-	75723.56	0.01
50	75725.4	49.98	-	-	-	-	-	-	-	-	75725.38	0.01

Chapter 5

Oscillator strength measurements of the 4s5s $^3S_1$ → 4s*n*p $^3P_2$ Rydberg transitions of zinc

In this chapter, we have measured the oscillator strengths of the 4s5s $^3S_1 \rightarrow$ 4s*n*p $^3P_2$ ($18 \leq n \leq 53$) Rydberg transitions of zinc. The step-wise laser excitation from the ground state $4s^2\ ^1S_0$ was achieved using three dye lasers simultaneously pumped by the second (532 nm) and third (355 nm) harmonics of a Q-switched Nd: YAG laser. The vapour containment and detection system was a single wire thermionic diode ion detector operating in space charge limited mode. A trend of the above-mentioned *f* - values from $n = 18$ to 53 have been presented. The measured *f*-values of the observed Rydberg series decreases smoothly with the increase in the principal quantum number as $n^{-2.24 \pm 0.06}$. Furthermore, continuity has been verified between the discrete *f*-values and the oscillator strength density at the threshold.

5.1 Introduction

In atomic physics energy levels, oscillator strengths, lifetimes and photoionization cross-sections are the fundamental parameters. These atomic parameters are very important not only in the fundamental research such as verifying the quantum defect theory, and studying the atomic dynamics, but also in various applied applications, such as plasma physics and astrophysical studies, in which they are used for the determination of atomic abundance. Oscillator strengths are also very important in thermonuclear research, where the atomic radiation is the major loss mechanism. The energy levels of zinc were investigated extensively using the conventional as well as laser excitation schemes [63, 69]. However, the detail investigations of the oscillator strength of the Rydberg transitions of zinc are still missing in the literature. Therefore, the objective of the present investigation was to experimentally determine the oscillator strengths of the 4s5s $^3S_1 \rightarrow$ 4s*n*p $^3P_2$ Rydberg transitions of zinc.

Over the past few decades, almost all the theoretical as well as experimental investigation on the oscillator strengths of zinc were based on the low lying principal series of zinc using the several techniques [72, 73]. The experimentally determined oscillator strengths were reported by few groups such as Kerkhoff et al. [74] measured the radiative lifetimes of the triplet states of Zn for the 4s*n*s $^3S_1$ (n = 5-7) and 4s*n*d

$^3D_3$, $^3D_2$ and $^3D_1$ (n = 4–6) transitions excited from the 4s4p^{3}P states and reported the oscillator strengths of the 4*sns* $^3S_1 \rightarrow$ 4pmp ^{3}P and 4*snd* ^{3}D $\rightarrow$ 4pmp ^{3}P few low lying transitions. Ueda et al. [75] applied hook method to measure the oscillator strengths for the three lines among the 4s4p $^3P_{0,1,2} \rightarrow 4p^2\ ^3P_{0,1,2}$ auto-ionizing resonances. Subsequently, Ueda et al. [76] reported the absorption and dispersion studies of the 4s4p $^3P \rightarrow 4p^2\ ^3P$ multiplet of Zn. Afanaseva [77, 78] reported the oscillator strengths of the 4s4p $^1P_1 \rightarrow$ 4s*n*d $^1D_2$ ($4 \leq n \leq 20$) transitions and the 4s4p $^1P_1 \rightarrow 4p^2\ ^1D_2$ auto-ionizing resonance using the two channel quantum defect theory. Recently, Sami et al. [11] reported the oscillator strengths for the 4s4p $^3P_1 \rightarrow$ 4s*n*d $^3D_2$ Rydberg transitions of zinc from n = 23 to 55 and a smooth connection between discrete oscillator strengths and oscillator strength density at threefold has been established. Theoretically, Brian Warner [79] first time determined the oscillator strengths of the few elements including zinc for the $s^2 \rightarrow$sp and ss$\rightarrow$ sp transitions using the Thomas-Fermi-Dirac wavefunctions. Zilitis [80] computed the oscillator strengths of the resonance transitions of group-II elements using Hartree-Fock wavefunctions. Luc-Kŏcnig [81] calculated the transition probabilities of the $^3P_1 \rightarrow\ ^1S_0$ transitions of group II elements. Glowacki and Migdalek [82, 83] reported the oscillator strength of the spin-allowed and spin forbidden $ns^2\ ^1S_0 \rightarrow nsnp\ ^{1,3}P_1$ transitions of (Zn, Sr, Ba, Cd, Hg and Yb) using the relativistic configuration interaction method. Brage and Fischer [84] reported the core polarization effects on the oscillator strength of the resonance transitions of Zn using the multi-configuration Hartree-Fock approach. Later, Chen & Cheng [85] computed the excitation energies of the $4s^2 \rightarrow$ 4s4p transitions using the relativistic configuration interaction (CI) calculations. The above literature survey shows that, the oscillator strengths of zinc mostly limited to the few low lying transitions of the principal series. Therefore, in the present contribution, we have experimentally determined the oscillator strengths of the 4s5s $^3S_1 \rightarrow$ 4s*n*p $^3P_2$ Rydberg transitions from n = 18 to 53. A smooth connection has been studied between the oscillator strengths of the discrete region and the oscillator strengths density at threshold.

5.2 Experimental Detail

The experimental set-up is almost same as in Figure 4.1. Three-step laser excitation scheme for the investigation of 4s*n*p $^3P_2$ Rydberg states is shown in Figure 5.1. The

first step dye laser was pumped by the second harmonic of the Nd: YAG laser using the R-610 dye and its output was frequency doubled using BBO type-I crystal to excite the 4s4p $^3P_1$ level of zinc at 307.9 nm [63].

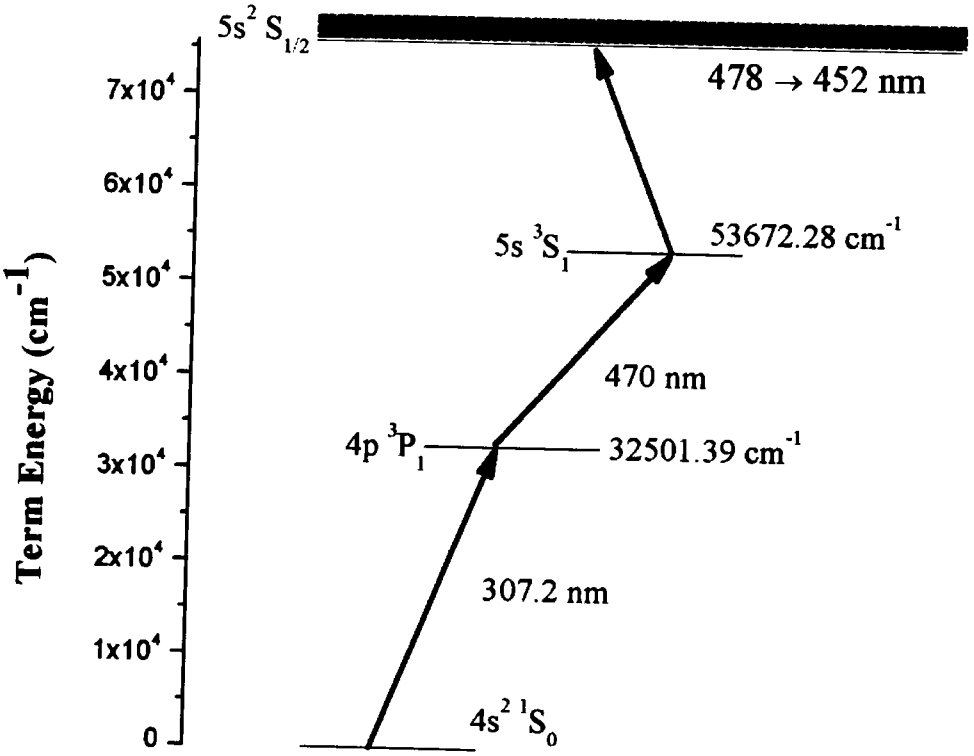

Figure 5.1 Three step laser excitation scheme for the investigation of highly excited states.

The second step dye laser was operated with LD-466 dye and was pumped by the third harmonic of the same Nd: YAG laser to populate 4s5s $^3S_1$ level at 472.4 nm [63]. The third dye laser was scanned up to the first ionization threshold to acquire the highly excited states of zinc. Three dye lasers were spatially overlapped in the central heating region of the thermionic diode ion detector. The experimental procedure adopted in this experiment is almost similar as described in chapter 4 and 2.

5.3 Results and Discussion

The photo-excitation spectrum of Zn from 75590– 75770 cm^{-1} energy range is shown in Figure 5.2 excited from the 4s5s $^3S_1$ intermediate state. According to the Russell-Saunders or LS Coupling scheme, the accessible series from the 4s5s $^3S_1$ level are 4s4p $^3P_{0,1,2}$. However, if the $\Delta S = 0$ selection rule is relaxed, the spin forbidden 4s4p

$^1P_1$ transition can be observed confirming the departure from LS coupling for high Z elements. In the observed spectrum, the dominating series is assigned as 4s*n*p $^3P_2$ based on the electric dipole selection rules, a transition is more favorable if $\Delta\ell = \Delta L = \Delta J = +1$, therefore, from the 4s5s $^3S_1$ level, the most probable transitions will be 4s*n*p $^3P_2$.

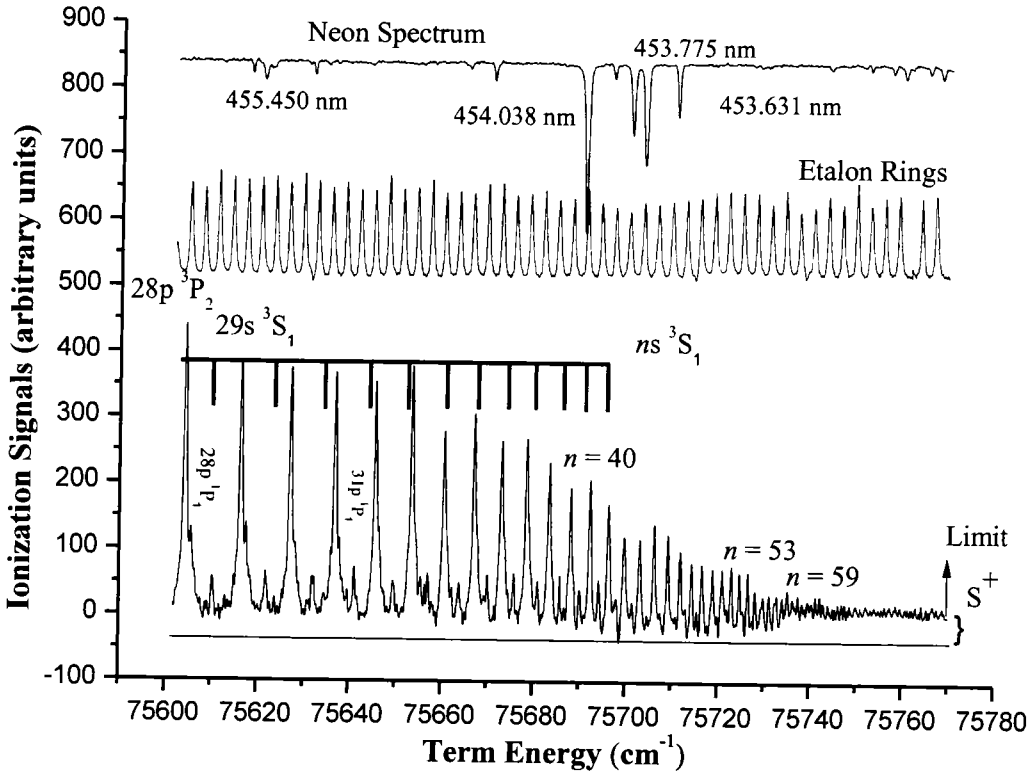

Figure 5.2 A portion of the zinc spectrum which shows the 4s5s $^3S_1 \rightarrow$ 4s*n*p $^3P^o_2$ Rydberg series from n = 28 to 59.

Furthermore, the 4s4p ^3P multiplet cannot be resolved in the present work due to the line width of the dye lasers ≈ 0.3 cm^{-1}. As the energy separation between the 4s16p $^3P_{0,1,2}$ fine structure multiplets is 4s16p $^3P_2 \rightarrow$ 4s16p$^3P_1$ is 0.4 cm^{-1} and for 4s16p $^3P_3 \rightarrow$ 4s16p $^3P_2$ is 0.3 cm^{-1} as reported by Kompitsas et al. [7] and the fine structure splitting decreases as $1/n^3$. In addition, few lines of the 4s*n*p $^3P_2$ series, appearance of the 4s*n*p $^1P^o_1$ series is due to the relaxation of $\Delta S = 0$ selection rule. The term energies and quantum defects of the 4s*n*p $^1P_1$ series are in good agreement with the reported results of Brown et al. [6] up to n = 66.

The weakest series is identified as 4s*n*s $^3S_1$, the emergence of this series is due to the collisional induced angular momentum mixing or 'ℓ' mixing induced by the bias

voltage of the thermionic detector which breaks down the electric dipole selection rules $\Delta\ell = \pm 1$: The 4s*n*s $^3S_1$ parity forbidden transitions were observed from $n = 29$ to 40 and after that it loses its signal intensity. Similar, parity forbidden transitions were reported by Vidolova-Angelova et al. [86] in the spectra of cadmium. They reported the 5s*n*s $^3S_1$ ($31 \leq n \leq 39$) and 5s*n*d $^3D_3$ ($17 \leq n \leq 22$) series emerging due to the 'ℓ' mixing from the DC Stark effect. The identification of these series were further supplemented by calculating the quantum defects using the following Rydberg relation:

$$n^* = n - \delta_\ell = \sqrt{\frac{R_{yd}}{IP - E_n}} \tag{5.1}$$

Here, E_n are the term energies, IP is the ionization energy of zinc 75769.31 ± 0.05 cm^{-1} NIST atomic database [67] and R_{yd} = 109736.404 cm^{-1} is the mass corrected Rydberg constant of zinc. The n, n^*, and δ_ℓ are the principal quantum number, effective quantum number, and quantum defect, respectively.

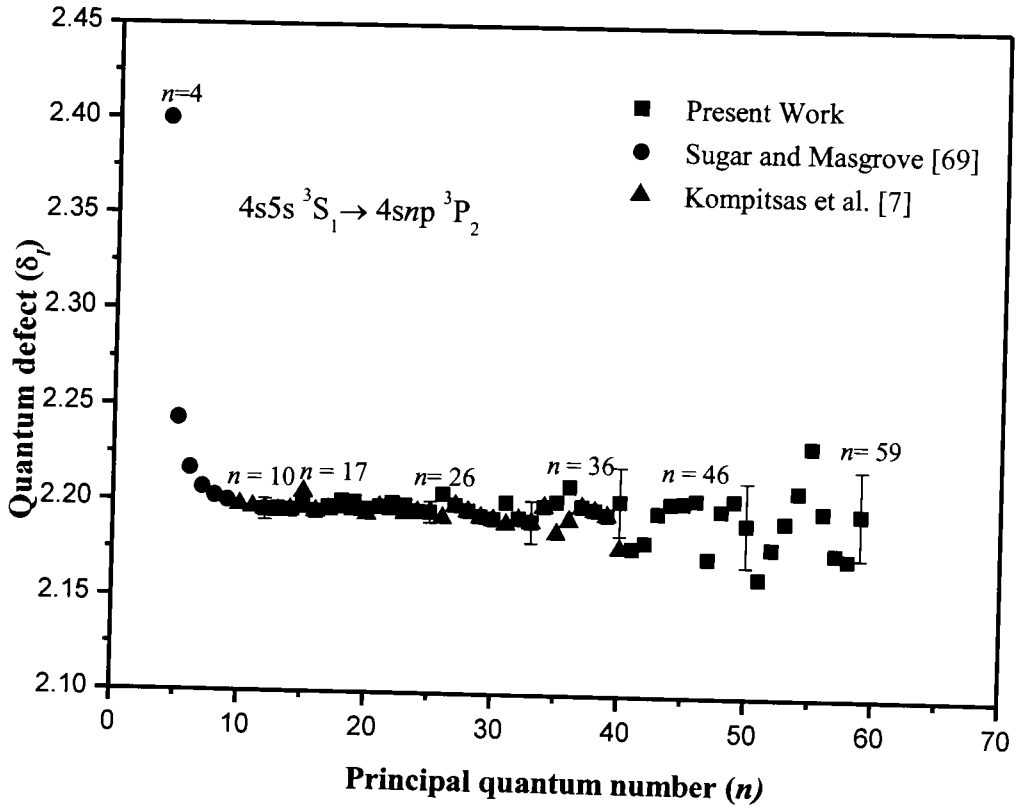

Figure 5.3 The plot of principal quantum number and quantum defect. The errors bars are according to the experimental uncertainty 0.3 cm^{-1} in term energies.

The quantum defects of the 4s*n*p^{3}P$_2$, 4s*n*p ^{1}P$_1$, and 5s*n*s ^{3}S$_1$ series are determined as δ_ℓ = 2.198, 2.101, and 2.715, respectively, the quantum defects are in good agreement with the previously reported work [6, 7]. Figure 5.3 shows the plot of the quantum defects (δ_ℓ) versus the principal quantum number n of the 4s*n*p ^{3}P$_2$, series. The quantum defects determined in the present work are represented as squares, triangles (n = 10 – 40) and circles (n = 4 – 9) represents the previously reported work of Kompitsas et al. [7] and Sugar and Masgrove [69], respectively. The quantum defects at lower n values are almost consistent up to n = 40 within reported uncertainty. However, at higher n = 40, the uncertainty in the quantum defects increases as the relative accuracy of the small energy difference $IP - E_n$ decreases for the high Rydberg states and this is represented as larger error bars in the determination of δ_ℓ.

Finally, oscillator strengths of the 4s5s ^{3}S$_1$ → 4s*n*p ^{3}P$^o_2$ Rydberg transitions were determined using the technique described by Mende and Kock, [87] with the assumption that ionization probability of the transitions that lie within k_BT is unity (i.e. $\Delta E \leq k_BT$). Where, k_B is the Boltzmann constant, T the temperature in Kelvin, and ΔE is the energy difference between the ionizing potential and the energy of the Rydberg level. As long as the above condition is fulfilled, the oscillator strengths of the Rydberg transitions can be determined from the following relation: [40]

$$f_n = \frac{4\pi\varepsilon_o mc}{\pi e^2}\left(\frac{S^{Ryd}}{S^+}\right)\left(\frac{\lambda^+}{\lambda^n}\right)\sigma(\lambda^+) \qquad (5.2)$$

Here f_n is the oscillator strength of the n^{th} transition of Rydberg series which is directly proportional to the photoionization cross-section $\sigma(\lambda^+)$ at ionization threshold. The S^+ is the ion signal at the ionization threshold (as shown in Figure 5.2) and S^{Ryd} is the integrated ion signal intensity for the n^{th} transition at a wavelength λ^n. The integrated signal intensity is equal to the peak value times the half-width, that is S^{Ryd} = signal intensity x $c\Delta k$, where c is the speed of light and k is the wave number in cm^{-1}. The constants e, m, c and ε_o are the charge of electron, the mass of the electron, speed of light and the permittivity of free space respectively.

Oscillator strengths of the 4s5s ^{3}S$_1$ → 4s*n*p ^{3}P$_2$ Rydberg transitions from n = 18 to 53 have been determined using the equation (5.2). The parameters λ^n, λ^+, S^+; and S^n were

extracted from the photoionization spectrum (see Figure 5.2). The value of the photoionization cross-section of the 4s5s $^3S_1$ intermediate state at the first ionization threshold $\sigma(\lambda^+)$ was reported as 0.724 ± 0.087 Mb by Liu et al. [88] computed using a close coupling R-matrix method. The lower limit on the principal quantum number $n \geq 18$ is due to the condition that ionization probabilities of the Rydberg transitions must be unity. In the present work, the energy difference between the $n \geq 18$ states and the first ionization threshold is 439 cm^{-1}, which is clearly less than the thermal energy in the present experimental work $k_BT \approx 521\ cm^{-1}$. Therefore, it is assumed that all the transitions higher than $n \geq 18$ are thermally ionized and their ionization probabilities are assumed to be unity. In a thermionic diode ion detector, this condition can be achieved comparatively easily by optimizing the temperature and buffer gas pressures. Although in the present experimental work, we have not performed any systematic studies on the ionization probabilities of the highly excited transitions at different temperatures and buffer gas pressures. However, Niemax [89] reported the ionization probabilities of the principal series of rubidium as unity for $n \geq 25$ in a thermionic diode ion detector at ≈16 mbar. On the higher side, we have limit to the $n \leq 53$, since beyond this, it was not possible to accurately determine the integrated signal intensity and full width and half maximum (FWHM). Although the Rydberg series have been observed up to n =59.

In Figure 5.4, oscillator strengths of the Rydberg transitions are plotted versus the principal quantum number n. The solid line is the fit of $f_n = K/n^m$ to the experimental data point indicating a smooth decreasing trend in f-values as m = 2.24 ± 0.06 for the 4s5s $^3S_1 \rightarrow$ 4snp $^3P_2$ series. Ideally, f-values decreases as $1/n^3$, however, the lower exponent value is due to the intensity variation in the photoionization spectra, due to experimental conditions such as temperature, pressure, and pulse to pulse variation in the energy.

Table 5.1 consists of oscillator strengths of the 4s5s $^3S_1 \rightarrow$ 4snp $^3P_2$ Rydberg transitions, principal quantum number n, wavelengths, and term energies. The error bar in the oscillator strengths are due to uncertainty in the measurement of the photoionization cross section which is ≈ 12%. Additional uncertainties are in the measurement of the signal height and width (FWHM) of the spectral lines. Therefore, the overall uncertainty in the calibration of the oscillator strength is less than 20%, for

the lower $n \leq 28$ values and >25% for the higher members of the Rydberg series due to the fluctuation in the photoionization spectrum

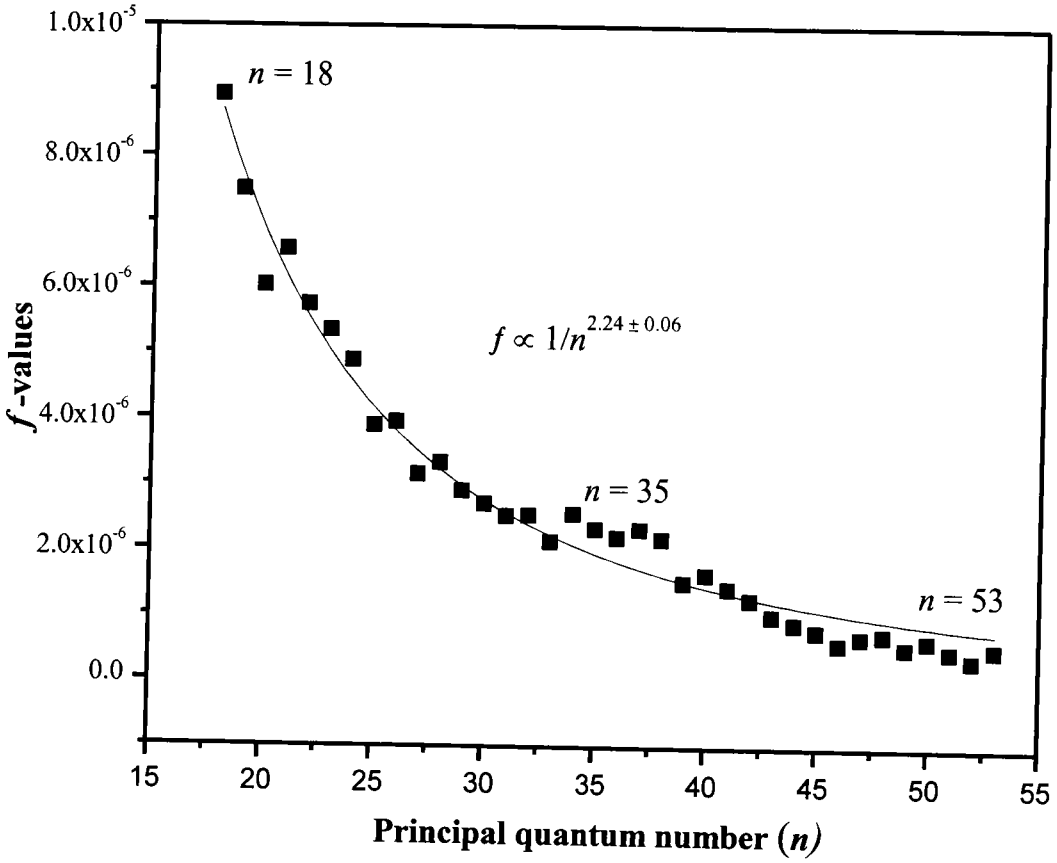

Figure 5.4 Oscillator strengths and the principal quantum number n of the 4s5s $^3S_1 \rightarrow 4snp\ ^3P_2$ ($18 \leq n \leq 53$) Rydberg transitions of zinc.

In order to investigate the connection between the oscillator strengths distribution in the bound region and oscillator strength density df/dE at threshold, the following relations are used [40];

$$\lim_{n\to\infty} \frac{(n^*)^3}{2R_{yd}} f_n = \frac{df}{dE}\Big]_{E=E_{ion}} \tag{5.3}$$

Here, n^* is the effective quantum number, R_{yd} is the mass corrected Rydberg constant of zinc and E is the photon energy. The total cross-section at the threshold is related to the oscillator strength density df/dE as:

$$\frac{df}{dE} = 9.11 \times 10^{15} \sigma(E)\ \text{cm}^{-2}\,(\text{eV})^{-1} \tag{5.4}$$

Figure 5.5 is a plot of the $(n^{*3}f_n) / 2R_{yd}$ versus the photon energy (eV). The solid line is the linear fit to the data points indicating that the discrete oscillator strength coincides with the oscillator strength density at the threshold. It is obvious from this figure that the oscillator strength distribution in the discrete region, corresponding to the 4s4p $^3S_1$ $\rightarrow$ 4s*n*p $^3P_2$ ($18 \leq n \leq 53$) transitions and the density of oscillator strength at threshold connects each other within experimental uncertainty. However, if the *f*-values of the highly excited transitions beyond $n \geq 53$ are known, a connection can be confirmed at the first ionization. This continuity across the threshold is a fundamental principle of the quantum defect theory, which originates from the continuity in the wave function across the threshold [40].

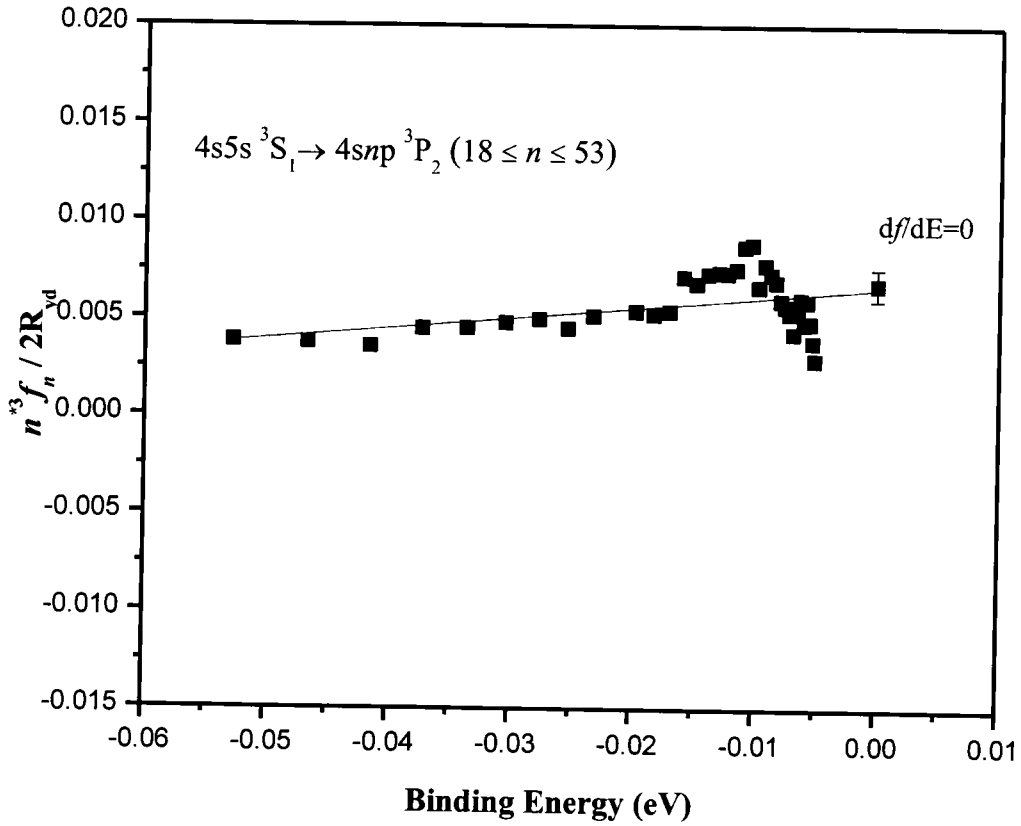

Figure 5.5 Plot of the $(n^{*3}f_n)/2R_{yd}$ and the binding energy (eV) corresponding to the 4s5s $^3S_1 \rightarrow$ 4s*n*p $^3P_2$ ($18 \leq n \leq 53$) transitions of zinc.

In conclusion, oscillator strengths for the 4s5s $^3S_1 \rightarrow$ 4s*n*p $^3P_2$ Rydberg transitions of zinc from n = 18 to 53 have been determined. A good agreement between the discrete *f*-values and the oscillator strengths distribution at threshold has been established to verify the fundamental condition of quantum defect theory which satisfies the continuity of the wavefunctions across the threshold. These studies provide useful

information in various fields of science, such as astrophysics, plasma physics, radiation physics, in the dynamics of stellar atmosphere for the determination of atomic abundance and it is also important in thermonuclear research.

Table 5.1 The principal quantum number n, wavelengths (nm), term energies (0.3 cm^{-1}) of the 4snp $^3P_2$ Rydberg series from n = 18 - 59 have been presented along with the previously reported data. In the fourth column oscillator strengths of the 4s5s $^3S_1 \rightarrow$ 4snp $^3P_2$ ($18 \leq n \leq 53$) Rydberg transitions are listed.

n	Wavelength (nm)	Term Energies (cm^{-1}) ± 0.3	Term Energies (cm^{-1}) Kompitsas et al. [7]	f-values ($x10^{-6}$)
18	461.736	75329.7	75329.9	8.94 ± 1.79
19	460.655	75380.5	75380.7	7.48 ± 1.50
20	459.753	75423.1	75423.2	6.02 ± 1.20
21	458.997	75458.9	75458.9	6.58 ± 1.32
22	458.356	75489.4	75489.5	5.74 ± 1.15
23	457.804	75515.7	75515.8	5.35 ± 1.07
24	457.326	75538.5	75538.5	4.89 ± 0.98
25	456.913	75558.3	75558.3	3.90 ± 0.78
26	456.554	75575.5	75575.7	3.96 ± 0.79
27	456.233	75590.9	75590.9	3.16 ± 0.63
28	455.950	75604.5	75604.5	3.34 ± 0.67
29	455.699	75616.6	75616.6	2.91 ± 0.73
30	455.475	75627.4	75627.4	2.72 ± 0.68
31	455.276	75637	75637.1	2.53 ± 0.63
32	455.093	75645.8	75645.8	2.54 ± 0.64
33	454.930	75653.7	75653.7	2.15 ± 0.54
34	454.783	75660.8	75660.8	2.57 ± 0.64
35	454.648	75667.3	75667.4	2.34 ± 0.59
36	454.526	75673.2	75673.3	2.21 ± 0.55
37	454.413	75678.7	75678.7	2.34 ± 0.59
38	454.310	75683.7	75683.7	2.19 ± 0.55
39	454.215	75688.3	75688.3	1.53 ± 0.38
40	454.128	75692.5	75629.6	1.66 ± 0.42
41	454.046	75696.5		1.44 ± 0.36
42	453.971	75700.1		1.27 ± 0.32
43	453.903	75703.4		1.02 ± 0.26
44	453.840	75706.5		0.904 ± 0.23
45	453.780	75709.4		0.793 ± 0.20
46	453.724	75712.1		0.598 ± 0.15
47	453.671	75714.7		0.707 ± 0.18
48	453.623	75717		0.741 ± 0.19
49	453.578	75719.2		0.549 ± 0.14
50	453.535	75721.3		0.653 ± 0.16
51	453.494	75723.3		0.494 ± 0.12
52	453.457	75725.1		0.369 ± 0.09
53	453.422	75726.8		0.532 ± 0.13
54	453.3889	75728.4		
55	453.35807	75729.9		
56	453.32724	75731.4		
57	453.29847	75732.8		
58	453.27176	75734.1		
59	453.24711	75735.3		

Chapter 6

Conclusions and Future Works

In the present work highly excited states of zinc have been investigated using three step laser excitation techniques. A thermionic diode and atomic beam set-up have been used in combination with the Nd: YAG pumped dye lasers. In the first experiment we have observed the 4s*n*f $^1F_3$ Rydberg series of zinc from n = 20 to 50 through the 4s4d $^1D_2$ intermediate level the experiment was performed in atomic beam setup. The 4s*n*f $^1F_3$ Rydberg series has been extended up to n = 50. The term energies and quantum defects of the high orbital angular momentum ($\ell = 3$) series is less penetrating with the core electron. Therefore, core polarization model is used to determine the Zn^+ core dipole polarizability as $\alpha_d = 18.33 \pm 0.95\, a_o^3$, which is in excellent agreement with the previously reported results. The next experiment was carried out to investigate the 4s*n*f ^3F states of zinc from the 4s*n*d $^3D_2$ multiplet. Since the experiment was performed in thermionic diode and because of the thermal energy collision the 4s*n*d $^3D_{1,3}$ level was also get populated as result we have observed 4s*n*f $^3F_3$ ($12 \le n \le 50$), 4s*n*f $^3F_2$ ($12 \le n \le 28$) and 4s*n*f $^3F_4$ ($12 \le n \le 33$) Rydberg series. Besides, the first ionization potential of zinc has also been measured as 75769.31 ± 0.02 cm^{-1}, which is more reliable and in good agreement with the previously reported value. In the next experiment 4s5s $^3S_1$ intermediate level was populated from the 4s4p $^3P_1$ level to investigate the 4s4p $^3P_2$ Rydberg series. The 4s*n*p $^3P_2$ series has been observed from n = 4 to 53. In addition oscillator strengths of the 4s5s $^3S_1 \rightarrow$ 4s*n*p $^3P_2$ ($18 \le n \le 53$) have been determined. A connection between discrete oscillator strengths and oscillator strength density at the limit has been verified, while in the basic principle of QDT.

In future, to extract the scope of this research work the Rydberg series of zinc can be further extended up to high principal quantum number n by using narrow bandwidth dye lasers or by minimizing the electric field in the thermionic diode. The autoionizing spectra can be investigated by using appropriate laser excitation scheme.

References

[1] M.E. Koch and C.B. Collins, "Space-charge ion detection of multiphoton absorption phenomena in lithium vapor", Phys. Rev. A **19**, 1098 (1979).

[2] W.A. Young, M.Y. Mirza and W.W. Duley, "Multiphoton ionization spectra in lithium vapour", Opt. Commun. **31**, 157 (1979).

[3] I. Labazan and S. Milosevic, "Lithium vapour excitation at 2S→3D two-photon resonance", Eur. Phys. J. D **8**, 41 (2000).

[4] F.B. Dunning, T.C. Killian, S. Yoshida and J. Burgdörfer, "Recent advances in Rydberg physics using alkaline-earth atoms", J. Phys. B: At. Mol. Opt. Phys. **49**, 2003 (2016).

[5] L.W. He, C.E. Burkhardt, M. Ciocca, and J.J. Leventhal and S. T. Manson, "Absolute Cross Section for the Photoionization of the 6s6p ^{1}P Excited State of Barium", Phys. Rev. Lett. **67**, 2131 (1991).

[6] C. M. Brown, S. G. Tilford, M. L. Ginter, "Absorption spectra of Zn I and Cd I in the 1300–1750 Å region", J. Opt. Soc. Am. **65**, 1404 (1975).

[7] M. Kompitsas, C. Baharis, Z. Pan, "Rydberg states of zinc and measurement of the dipole polarizability of the Zn^+ ion" J. Opt. Soc. Am. B **11**, 697 (1994).

[8] A. Nadeem, M. Nawaz, S.A Bhatti, M.A. Baig, "Multi-step laser excitation of the highly excited states of zinc", Opt. Commun. **259**, 2, 834 (2006).

[9] M. Nawaz, A. Nadeem, S.A. Bhatti and M.A. Baig, "Two-step laser excitation of 4s*n*d $^3D_{1,2,3}$ and 4s*n*s $^3S_1$ states from the 4s4p ^{3}P levels in zinc", J. Phys. B: At. Mol. Opt. Phys. **39**, 871 (2006).

[10] M. Shah, G. Aisha, S. Shahzada and A. Nadeem, "Step-Wise Laser Excitation of the 4s*n* f ^{3}F Rydberg States of Neutral Zinc", Spectrosc. Lett. **51**, 1 (2018).

[11] S.U. Haq, A. Nadeem, M. Nawaz, M.A. Baig, "Oscillator strength measurements of the highly excited 4s4p $^3P^o_1$→4s*n*d $^3D_2$ transitions of zinc" J. Opt. Soc. Am. B **27**, 402 (2010).

[12] G. Aisha, M. Shah, S. Shahzada, S.U. Haq, H. Shakeel and A. Nadeem, "Investigation of the 4s*n*f $^1F_3$ Rydberg states of zinc and determination of dipole polarizability zinc ion", Spectrochim. Acta, Part B, **142**, 85 (2018).

[13] G. Aisha, M Shah, A. Nadeem, S.U. Haq and S. Shahzada, "Oscillator strength measurements of the 4s5s $^3S_1 \rightarrow 4snp\ ^3P_2$ Rydberg transitions of zinc", Spectrosc. Lett. **52**, 143 (2019).

[14] A.P. Thorne, "Spectrophysics", 2nd edition, New York (1988).

[15] W. Demtröder, "Laser Spectroscopy", Volume 2, Berlin: Springer (2008)

[16] T. F. Gallagher, "Rydberg Atoms", Cambridge University Press (1994).

[17] H. Friedrich, "Theoretical Atomic Physics", Springer (2005).

[18] C.S. Adams, J.D. Pritchard, J.P. Shaffer, "Rydberg atom quantum technologies", J. Phys. B: At. Mol. Opt. Phys. **53**, 1 (2019).

[19] M. Saffman, T.G. Walker, and K. Mølmer, "Quantum information with Rydberg atoms", Rev. Mod. Phys. **82**, 2313 (2010).

[20] H. Haken and H.C. Wolf, "The Physics of Atoms and Quanta", Springer Berlin New York (2004).

[21] C.J. Foot, "Atomic Physics", Oxford Master Series in Physics (2004).

[22] W. Demtröder, "Atoms, Molecules and Photons", Berlin: Springer (2005).

[23] O. Svelto, "Principles of Lasers" 5th edition, Springer New York (2010).

[24] H.E. White, "Introduction to Atomic Spectra" New York (1934).

[25] L.J. Curtis and C.E. Theodosiou, "Comment on the dipole polarizability of the Zn^+ ion", J. Opt. Soc. Am. **12**, 175 (1995).

[26] J. Mitroy, M.S. Safronova, C.W. Clark, "Theory and applications of atomic and ionic polarizabilities", J. Phys. B: At. Mol. Opt. Phys, **43**, 202001 (2010).

[27] C.J. Sansonetti, K.L. Andrew, J. Verges, "Polarization, penetration, and exchange effects in the hydrogenlike *n*f and *n*g term of cesium" J. Opt. Soc. Am. **71**, 4, 423 (1981).

[28] K.D. Bonin, V.V. Kresin, "Electric-Dipole Poalrizabilities of atoms, Molecule and Clusters", World Scientific (1997).

[29] C. Laughlin, "The dipole polarizability of Zn^+ and the high-ℓ Rydberg levels of Zn", Z. Phys. D **39**, 201 (1997).

[30] M. Ilias, P. Neogrady, "Ionization potentials of Zn, Cd, Hg a dipole polarizabilities of Zn^+, Cd^+, Hg^+: correlation and relativistic effects", Chem. Phys. Lett. **309**, 441 (1999).

[31] A.S. Kutsenko, K.B. MacAdam, S.F. Dyubko and N.L. Pogrebnyak, "Millimeter-wave spectroscopy of Zn I in $^1D_2$, $^1F_3$ and $^1G_4$ Rydberg states", J. Phys. B: At. Mol. Opt. Phys. **48**, 245005 (2015).

[32] R.R. Freeman, D. Kleppner, "Core polarization and quantum defects in high-angular-momentum states of alkali atoms", Phys. Rev. A **14**, 1614 (1975).

[33] M.C.E. Hubber and R.J. Sandeman, "The measurement of Oscillator Strengths", Rep. Prog. Phys. **49**, 397 (1986).

[34] W. Mende and M. Koch, "Oscillator strengths of Ba I and Sr I Rydberg transitions" J. Phys. B: At. Mol. Opt. Phys. **29**, 655 (1995).

[35] A. Nadeem and S.U. Haq, "Oscillator strength measurements of the 5s5p $^3P_1$ $\rightarrow$5s*n*d $^3D_2$ Rydberg transitions of cadmium", Spectrochim. Acta Part B **65**, 842 (2010).

[36] S. U. Haq and A. Nadeem, "Photoionization from the 6p $^2P_{3/2}$ state of neutral cesium", Phys. Rev. A **81**, 063432 (2010).

[37] A. Nadeem, S. U. Haq, M. Nawaz, M. Shah and M. A. Baig, "Measurement of the oscillator strength for the 6s7p (1/2,1/2)1 $\rightarrow$ 6p*n*p (1/2,3/2)2 Rydberg transitions of lead" Spectrochim. Acta Part B **66**, 841 (2011).

[38] S.U. Haq, A. Nadeem and M. Nawaz, "Photoionization cross section and oscillator strengths of neutral cesium" J. Quant. Spectrosc. Radiat. Transf. **113**, 2058 (2012).

[39] S. Shahzada, P. Ijaz, M. Shah, S.U. Haq, M. Ahmed, and A. Nadeem, "Photoionization studies from the 3p ^2P excited state of neutral lithium", J. Opt. Soc. Am. B **29**, 12, 3386 (2012).

[40] J. P. Connerade, "Highly Excited Atoms", Cambridge University Press (1998)

[41] P.P. Sorokin, J.R. Lankard, V.L. Moruzzi, and E.C. Hammond, "Flashlamp-Pumped Organic Dye Lasers", J. Chem. Phys. **48**, 4726 (1968)

[42] F.P. Schäfer (Ed.), "Dye Lasers", Springer-Verlag, Berlin (1990).

[43] K. Shimoda, "High-Resolution Laser Spectroscopy" Springer-Verlag Berlin (1976).

[44] T.W. Hansch, "Repetitively Pulsed Tunable Dye Laser for High Resolution Spectroscopy", Appl. Opt. **11**, 4, 895 (1972).

[45] F.J. Durate and J.A. Piper, "A Double-Prism Beam Expander for Pulsed Dye Lasers", Opt. Com. **35**, 1, 100 (1980).

[46] K. Pasandideh, M. Rahbari, R.S. Bonabi, "Narrow linewidth, tunable dye laser by multiple-prism beam expander", Opt. Quan. Elect. **49**, 306 (2017).

[47] F.J. Duarte and L.W. Hillman (Eds.), "Dye Laser Principles", Academic, New York, (1990).

[48] D.C. Hanna, P. Karkainen and R.A. Wyatt, "Simple beam expander for frequency narrowing of dye lasers", Opt. Quan. Elect. **7**, 115 (1975).

[49] P.A. Franken, A. E. Hill, C.W. Peters and G. Weinreich, "Generation of Optical Harmonics", Phys. Rev. Lett. **7**, 118 (1961).

[50] H. Abramczyk, "Introduction to Laser", Elsevier, Netherland (2005).

[51] G. Drake, Atomic, Molecular & Optical Physics Handbook, New York, AIP Press (1996).

[52] S. Shahzada, M. Shah, S.U. Haq, M. Nawaz, M. Ahmed, A. Nadeem, "Spectroscopic investigation of the 3d ^{2}D→*n*f ^{2}F transitions in lithium", Spectrochim. Acta Part B: At. Spectrosc. **119**, 83 (2016)

[53] A. Nadeem, S.U. Haq, "Photoionization from the 5p $^2P_{3/2}$ state of robidium" Phys. Rev. A **83**, 063404 (2011).

[54] A. Nadeem, M. Shah, S.U. Haq, S. Shahzada, M. Mumtaz, A. Waheed, M. Nawaz, M. Ahmed, M. A. Baig, "Three-step laserexcitation of odd-parity 5s5d ^{3}D→5d*n*f ^{3}F states of cadmium", Eur. Phys. J. D **68**, 192 (2014).

[55] A. Nadeem, M. Shah, S. Shahzada, N. Ahmed, S. U. Haq, "Spectroscopic investigation of the odd-parity 3d ^{2}D→*n*f ^{2}F transitions of neutral sodium", J. Appl. Spectrosc. **82**, 5, 719 (2015).

[56] K. Niemax, "Spectroscopy using thermionic diode detectors", Appl. Phys. B **38**, 147 (1985).

[57] R. Beigang, D. Schmidt and A. Timmermann, "Doppler-free three-photon spectroscopy of 3s*n*f Rydberg states of Mg", Phys. Rev. A **29**, 2581 (1984).

[58] U. Griesmann, B. Esser, M.A. Baig, "Photoionization cross section of lead near the 6s26p $^2P_{3/2}$ threshold", Phys. Rev. A **44**, 11, 6977(1991).

[59] A. Nadeem, A. Ahad, S.A. Bhatti, N. Ahmad, R. Ali and M A Baig, "Two-step laser spectroscopy of the even-parity Rydberg levels of neutral tin", J. Phys. B: At. Mol. Opt. Phys. **32** 5669 (1999).

[60] M.A. Baig, M. Yaseen, R. Ali, A. Nadeem, S.A. Bhatti, "Near-threshold photoionization spectra of strontium", Chem. Phys. Lett. **296**, 403 (1998).

[61] M.A. Baig, M. Yaseen, A. Nadeem , R. Ali, S.A. Bhatti, "Three-photon excitation of strontium Rydberg levels" Opt. Com. **156**, 279 (1998)

[62] N. Ahmed, A. Nadeem, M. Nawaz, S.A. Bhatti, M. Iqbal, M.A. Baig, "Resistively heated high temperature atomic beam source", Rev. Sci. Instrum. **76**, 063105 (2005).

[63] D. Gullberg and U. Litzen, "Accurately Measured Wavelengths of Zn I and Zn II Lines of Astrophysical Interest", Phys. Scr. **61**, 652 (2000).

[64] N. B. Eshkobilov, "Laser spectroscopy of the Rydberg states of atoms group II B (Zn, Cd, Hg)", J. Appl. Spectrosc., **67**, 343 (2000).

[65] O. Tukhlibaev and U.Z. Alimov, "Laser photoionization spectroscopy of the zinc atom and the study of zinc sulfide evaporation", Opt. Spectrosc. **88**, 506 (2000).

[66] I. Martinson, L.J. Curtis, S. Huldt, U. Litzen, L. Lileby, S. Mannervik and B. Jelenkovic, "Lifetimes for Low-lying Levels in Zn I and Zn II", Phys. Scr. **19**, 17 (1979).

[67] NIST Atomic Spectra Database, Version 3.0, http:\\www.physics.nist.gov. .

[68] J.H.V. Vleck and N.G. Whtelaw, "The quantum defect of non-penetration orbits, with special application to Al II", Phys. Rev. **44**, 551 (1933).

[69] J. Sugar and A. Musgrove, "Energy Levels of Zinc, ZnI through ZnXXX", J. Phys. Chem. Ref. Data **24**, 1803 (1995).

[70] E. Biemont and M. Godefroid, "A reassessment of the zinc solar abundance", Astron. Astrophys. **84**, 361 (1980).

[71] P. Esherick, J.A. Armstrong, R.W Dreyfus and J.J. Wynne, "Multiphoton Ionization Spectroscopy of High-Lying", Even-Parity states of calcium, Phys. Rev. Lett. **36**, 1296 (1976).

[72] L.J. Curtis, "Precision Oscillator Strength and Lifetime Measurements". In Handbook Springer of Atomic", Molecular, and Optical Physics; G. W. F. Drake, Ed; AIP Press: New York, 262 (2005).

[73] J. Richter, "Measurements of lifetimes and oscillator strengths of neutral and singly ionized atoms. Experimental results of the last five years", Phy. Scr. **8**, 70 (1984).

[74] H. Kerkhoff, M. Schmidt, P. Zimmermann, "Lifetimes and oscillator strengths in the triplet system of Zn I", Z. Phys. A **298**, 249 (1980).

[75] K. Ueda, H. Iimura, M. Karasawa, K. Fukuda, "Measurement of oscillator strengths for three lines among the 4s4p $^3P^o$- $4p^2$ ^3P multiplet of Zn I", J. Phys. Soc. Jpn. **50**, 3545 (1981).

[76] K. Ueda, M. Karasawa, K. Fukuda, "Absorption and dispersion studies of the 4s4p $^3P^o$- $4p^2$ ^3P multiplet of Zn I", J. Phys. Soc. Jpn. **51**, 1941 (1947).

[77] N.V. Afanaseva, "Calculation of oscillator strengths of the principal series of zinc by the two-channel quantum defect method", Opt. Spektrosk. **52**, 776 (1982).

[78] N.V. Afanaseva, "Oscillator strengths of atomic Zn 4p $^1P^0_1 \rightarrow 4snd$ $^1D_2$ transitions", Opt. Spektrosk. **59**, 475 (1985).

[79] B. Warner, "Atomic Oscillator Strengths IV transitions of the type $s^2 \rightarrow sp$ and $ss \rightarrow sp$", Mon. Not. R. astr. Soc. **140**, 53 (1968).

[80] V.A. Zilitis, "Oscillator strengths for resonance lines of atoms of the group II elements", Opt. Spektrosk. **36**, 630 (1974).

[81] E. Luc-Koenig, "Relativistic effects on transition probabilities $^3P^o_1 \rightarrow {}^1S_0$ for group-II elements", J. Phys. B: At. Mol. Phys. **7**, 1052 (1974).

[82] L. Glowacki, J. Migdalek, "Relativistic configuration-interaction oscillator strength calculations with ab initio model potential wave functions", J. Phys. B: At. Mol. Phys. **36**, 3629 (2003).

[83] L. Glowacki, J. Migdalek, "Relativistic configuration–interaction oscillator strengths calculations with ab initio screened model-potential wave functions", J. Phys. B: At. Mol. Phys. **39**, 1721 (2006).

[84] T. Brage; C.F. Fischer, "Core polarization effects on oscillator strengths in neutral zinc" Phys. Scr. **45**, 43 (1992).

[85] M.H. Chen, K.T. Cheng, "A large-scale relativistic configuration-interaction approach: application to the $4s^2 - 4s4p$ transition energies and E_1 rates for Zn-like ions", J. Phys. B: At. Mol. Phys. **43**, 074019 (2010).

[86] Vidolova-Angelova; C. Bharis, G. Roupakas, M. Kompitsas, "Observations and theoretical analysis of highly excited singlet and triplet states of cadmium", J. Phys. B: At. Mol. Opt. Phys. **29**, 2453 (1996).

[87] W. Mende, M. Kock, "Oscillators strengths of BaI and SrI Rydberg transitions", J. Phys. B: At. Mol. Opt. Phys. **29**, 655 (1996).

[88] Y.P. Liu, C. Gao, J.L. Zeng, J.R. Shi, "Atomic data of Zn I for the investigation of element abundances", A&A **536**, A51 (2011).

[89] K. Niemax, "Investigation on the thermionic diode: the ionization probability of Rb n^2P_J atoms by noble gas collisions" Appl. Phys. B **32**, 59 (1983).

Annexure

Spectrochimica Acta Part B 142 (2018) 85–90

Contents lists available at ScienceDirect

Spectrochimica Acta Part B

journal homepage: www.elsevier.com/locate/sab

Technical note

Investigation of the 4s*nf* $^1F_3$ Rydberg states of zinc and determination of the dipole polarizability of the Zn^+ ion

G. Aisha [a], M. Shah [b], Shaista Shahzada [a], S.U. Haq [b], H. Shakeel [c], Ali Nadeem [b,*]

[a] Department of Physics, International Islamic University, Sector- H-10, Islamabad 44000, Pakistan
[b] National Institute of Lasers and Optronics (NILOP), P O Box Nilore 45650, Islamabad, Pakistan
[c] Department of Physics and Applied Mathematics, Pakistan Institute of Engineering and Applied Sciences (PIEAS), PO Nilore 45650, Islamabad, Pakistan

ARTICLE INFO

Article history:
Received 26 August 2017
Received in revised form 24 December 2017
Accepted 1 February 2018
Available online 10 February 2018

Keywords:
zinc
Rydberg states
odd-parity states
dipole polarizability
core polarization model

ABSTRACT

We report term energies and effective quantum numbers of the odd-parity 4s*nf* $^1F_3$ Rydberg series of zinc from 75,480 to 75,750 cm^{-1} energy range. The experiment was performed using three dye lasers simultaneously pumped by the second (532 nm) and third (355 nm) harmonics of a Q-switched Nd-YAG laser in conjunction with an atomic beam set-up. The new observation include the 4s*nf* $^1F_3$ ($20 \le n \le 50$) series excited from the 4s4d $^1D_2$ intermediate level. In addition, the dipole polarizability of the zinc core is determined as $\alpha_d = 18.33 \pm 0.95\ a_o^3$ using the core polarization model, which is in consistence with the earlier reported experimental and theoretical results.

1. Introduction

The spectroscopic studies of atomic Rydberg states are in many ways a mature field. However, there are number of situations in which experimental data are still missing. These situations generally involve atoms having resonance levels in the ultra-violet region with high ionization potentials or elements having high vaporization temperatures. The Rydberg states of Group IIB (Zn, Cd, and Hg) elements belong to same category having resonance levels in the ultra-violet region and ionization potentials are also very high.

According to the literature review, most of the laser based work on the highly excited states of zinc is reported from the 4s4p $^3P_1$ inter-combination level. Because the 4s4p $^3P_1$ level, located at 32501.399 cm^{-1} [1], can be populated comparatively easily using the frequency doubled dye laser at 307.67 nm. Earlier, Nadeem et al. [2] reported the term energies and quantum defects of the 4s*np* $^3P_2$ ($12 \le n \le 60$), 4s*np* $^1P_1$ ($16 \le n \le 30$) and 4s*ns* $^3S_1$ ($19 \le n \le 44$) series and the first ionization potential of zinc as 75,769.31 ± 0.05 cm^{-1}. Nawaz et al. [3] observed the even parity 4s*nd* $^3D_{1,2,3}$ ($14 \le n \le 55$) and 4s*ns* $^3S_1$ ($15 \le n \le 35$) series from the 4s4p $^3P_{0,1,2}$ intermediate level using the two-step laser excitation scheme. Eshkobilov [4] reported the term energies and quantum defects of the $^3P_{0,1,2}$ series of Zn, Cd and Hg along with the first ionization potentials. Tukhlibaev and Alimov [5] used the three-step laser excitation scheme for the investigation of the 4s*np* $^3P_1$ ($5 \le n \le 50$) Rydberg states of zinc using the pulsed electric field and determined the first ionization potential as 75,769.328 ± 0.018 cm^{-1}. However, The only laser based work on zinc from the 4s4p $^{1,3}P_1$ intermediate states were reported by Kompitsas et al. [6], their observations include 4s*nf* $^{1,3}F_j$ ($8 \le n \le 26$), 4s*ns* $^1S_0$ ($14 \le n \le 31$), 4s*nd* $^1D_2$ ($12 \le n \le 35$) and 4s*np* ^3P ($10 \le n \le 40$) series, using the multi-step and multi photon laser excitation. In addition, the dipole polarizability of zinc core was determined as $\alpha_d = 15.54\ a_o^3$ from the quantum defects of 4s*nf* $^{1,3}F_j$ series using the core polarization model. The 4s4p $^1P_1$ level located at 46745.404 cm^{-1} [1] requires 213.9 nm light, which is comparatively difficult to generate by frequency doubling the dye laser.

Although, the first systematic studies on the bound states of Zn and Cd were performed by Brown et al. [7], in zinc their observations include the 4s*np* $^1P_1$ ($4 \le n \le 66$), 4s*nd* $^1D_2$ ($4 \le n \le 20$) and 4s*np* $^3P_1$ ($4 \le n \le 12$) series. The first ionization limit of zinc was determined as 75,769.33 ± 0.18 cm^{-1} from the 4s*np* $^1P_1$ Rydberg series. Sugar and Musgrove [8] compiled all the available atomic energy levels of zinc for all stages of ionization form Zn I through Zn XXX. Gullberg and Litzen [1] accurately measured the wavelengths of Zn I and Zn II lines of astrophysical interest using a Fourier transform spectrometer and a hollow cathode lamp.

In the present experimental work, the three step laser excitation scheme was used for the investigation of odd parity 4s*nf* $^1F_3$ ($20 \le n \le 50$) Rydberg states of zinc. In addition, the dipole polarizability of the zinc core is measured as $\alpha_d = 18.33 \pm 0.95\ a_o^3$ using the core polarization model.

* Corresponding author.
E-mail address: drali_nadeem@yahoo.com (A. Nadeem).

https://doi.org/10.1016/j.sab.2018.02.001
0584-8547/

2. Experimental Detail

The schematic diagram of the experimental set-up is shown in Fig. 1. Briefly, our laser system is a Q-switched Nd-YAG laser operating at a 10 Hz repetition rate having pulse duration of 7 ns. The second (532 nm) and third (355 nm) harmonics were used to pump the three Hanna type (Hanna et al. [9]) dye lasers. The line width of the dye lasers was typically ≤ 0.3 cm^{-1}. The first dye laser was pumped by the third harmonic of the Nd-YAG laser using the Stilbene 420 dye and the beam was focused into a BBO type-1 crystal (6 mm long, cut 40° with respect to the optical axis) for the second harmonic generation. After separating the fundamental from second harmonic using a fused silica prism, the second harmonic was fed into the atomic beam apparatus, to excite the 4s4p $^1P_1$ level of zinc at 213.9 nm. The second dye laser was pumped by the second harmonic (532 nm) of the Nd-YAG laser, charged with Rhodamine-640 dye dissolved in methanol and, was fixed at 636.4 nm to populate the 4s4d $^1D_2$ level Gulberg and Litzen [1]. The third dye laser was charged with LDS 750 dye and scanned up to the first ionization threshold. The wavelengths of the dye lasers were measured with a spectrometer (Ocean Optics, HR-4000, 200–1100 nm and 0.75 nm resolution) equipped with a 600 lines/mm grating. The laser energy of the first dye laser was 0.5 mJ and the energy of the second and third dye laser were ~2 mJ. The energy of the dye lasers were measured using the energy meter (Top Max II, Coherent).

The collimated atomic beam of zinc atoms was produced by an oven heated to about 460 °C; the beam source consists of a tantalum crucible enclosed by a 0.05 mm thick tantalum foil to heat the crucible by radiation. The detail of the atomic beam apparatus particularly the oven assembly is described in our previous paper [10]. The collimated atomic beam of neutral zinc was then crossed between two stainless steel plates 50 × 50 mm^2 in dimension and 10 mm apart, which were both grounded to provide the field-free interaction. The atomic density in

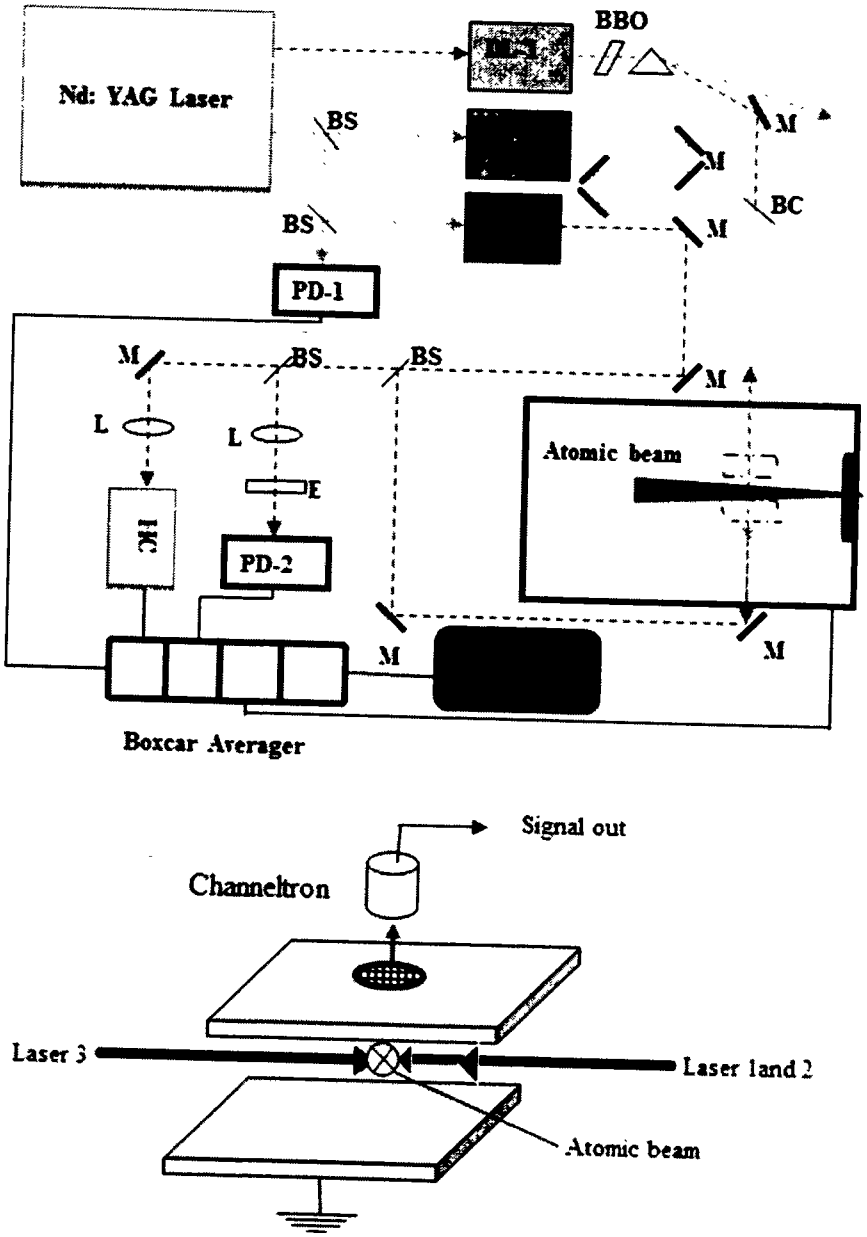

Fig. 1. Schematic diagram of the experimental set-up (BS beam splitter, DL dye laser, M mirror, BBO β barium borate, BC beam combiner, L lens, E etalon, PD photodiode, HC hallow cathode).

the interaction region is of the order of 10^{10} atoms/cm^3. The atomic beam chamber was evacuated down to 10^{-6} Torr. An electron multiplier (channeltron), configured to collect the ions, was mounted on the upper plate. The three Nd-YAG pumped dye laser beams intersect the atomic beam and the photoelectrons produced in an ionization process were detected orthogonal to the atomic and laser beams. The excited atoms were ionized either by absorbing another photon from the same laser pulse or due to the Rydberg-Rydberg and blackbody radiations or even due to the collisional ionization with the ground state zinc atoms [11-15].

The wavelength calibration was achieved by recording the optogalvanic spectra of neon as wavelength reference which are known with an accuracy of ≈0.0007 cm^{-1} NIST atomic database [17], the neon reference and photoionization signals are almost symmetric having line widths of the order of ~1 cm^{-1}, therefore line center are marked very accurately. The interference fringes from the etalon (FSR 3.5 ± 0.05 cm^{-1}) having a constant number of data points between the successive peaks interpolate between the neon reference lines and yields the laser excitation energies of the unknown ionization signals using a computer code within the accuracy of 0.25 cm^{-1}, also adding the contributions from the uncertainty in the intermediate level 0.005 cm^{-1} [1], the laser line width is 0.3 cm^{-1}, a single step in the dye laser stepper motor is 0.1 cm^{-1}. The term energies of the unknown zinc lines were determined by adding the intermediate level energies 4s4d $^1D_2$ 62,458.533 cm^{-1} [1] in the laser excitation energies of the 4s*nf* $^1F_3$ series.

The three signals from channeltron, hollow cathode and photodiode were simultaneously sampled using three gated integrator boxcar (SR-250) averagers. The SR-245 computer interface module was used for data acquisition. The spectra were recorded and stored on a computer for analysis.

3. Results and discussion

A three step laser excitation scheme for the investigation of highly excited states is shown in Fig. 2. The first frequency doubled dye laser was fixed at 46745.404 cm^{-1} and the second dye was at 62458.533 cm^{-1} [1] to populate the 4s4p $^1P_1$ and the 4s4d $^1D_2$ state respectively. The third dye laser was scanned from 768 to 750 nm to record the highly excited states. The lifetime of the 4s4d $^1D_2$ level is 20.5 ± 1.5 ns as reported by Martinson et al. [16]. Therefore, the time delay between the dye lasers pulses was not very critical. An optimum signal was registered when the third dye laser was delayed with respect to the second dye laser by a few ns. The selective excitation process at each step was verified by blocking anyone of the excitation dye laser beams and observing the photo-ionization signal.

$$4s^2\,{}^1S_0 \xrightarrow{213.9nm} 4s4p\,{}^1P_1 \xrightarrow{636.4nm} 4s4d\,{}^1D_2 \xrightarrow{768-750nm} 4snf\,{}^1F_3$$

The photo-ionization signals observed using the three-step laser excitation scheme are shown in Fig. 3 from 75,480–75,750 cm^{-1} energy range excited from the 4s4d $^1D_2$ level. The top trace is the optogalvanic spectra of neon for wavelength calibration and the middle one show the interference fringes from a 1-mm thick solid etalon and the bottom trace is the ionization signals of zinc. According to the LS-coupling scheme the accessible series from the 4s4d $^1D_2$ intermediate state are 4s*np* $^1P_1$ and 4s*nf* $^1F_3$. However, in the present experimental work only one series was observed that is assign as 4s*nf* $^1F_3$ and the *np* transition remain too weak to be detected. The 4s*nf* $^1F_3$ series is observed from $n = 20$ to 50, the identification of the 4s*nf* $^1F_3$ series is based on the values of the effective quantum numbers extrapolated from the lower member of the series reported in NIST atomic database [17] and by Kompitsas et al. [6]. Furthermore, according to the electric dipole selection rules, a transition is more favorable if $\Delta\ell = \Delta L = \Delta J = +1$ therefore, from the 4s4d $^1D_2$ level the most probable transitions are 4s*nf* $^1F_3$. The quantum defect of the 4s*nf* $^1F_3$ series was calculated using the following Rydberg relation:

$$n^* = n - \delta_\ell = \sqrt{\frac{R_{yd}}{IP - E_n}} \tag{1}$$

here E_n is the transition energy, *IP* is first ionization limit of zinc 75,769.31 ± 0.05 cm^{-1} [2], R_{yd} is the mass corrected Rydberg constant for zinc 109,736.404 cm^{-1}, and δ_l is the quantum defect. The Table 1 consists of the term energies, principal quantum number *n* and effective

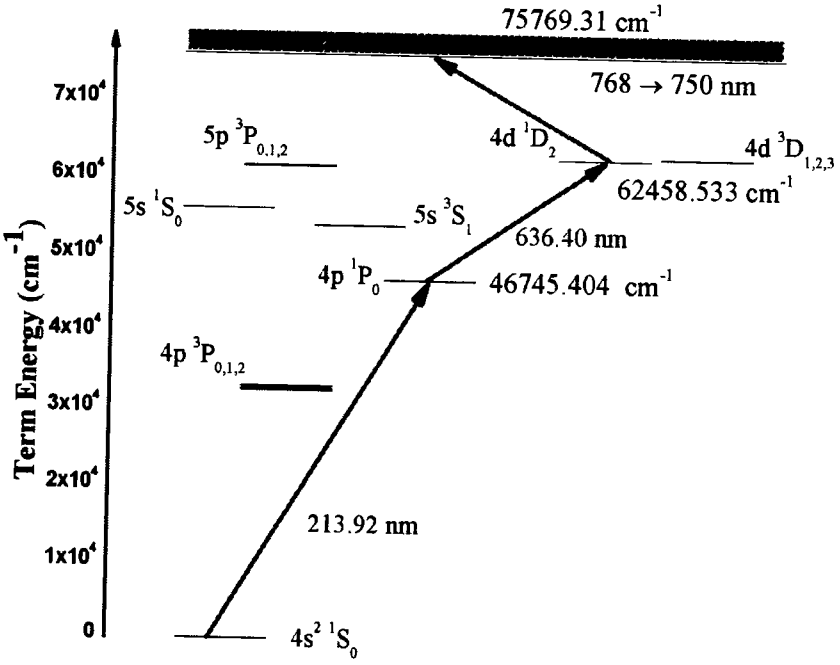

Fig. 2. Three-step laser excitation scheme to investigate Rydberg states of zinc.

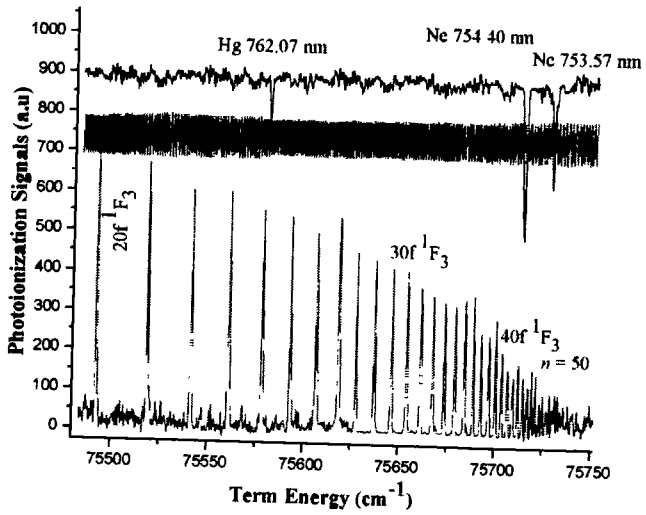

Fig. 3. The spectrum of zinc covering the energy region 75,480–75,750 cm^{-1} showing the 4s4d $^1D_1 \rightarrow$ 4snf $^1F_3$ Rydberg series from $n = 20$ to 50.

quantum number n^* of the 4snf $^1F_3$ Rydberg series. It also contains the term energies of the previously reported work [6,7]. The term energies determined in the present work are in good agreement with Kompitsas et al. [6] from $n = 20$ to 26 within reported uncertainty. The peak intensities of the Rydberg series clearly show a decreasing trend towards the series limit. The intensity variations reveal a $1/n^{*1.82}$ inclinations in the peak intensity, this is due to the pulse to pulse variations in the laser beam and also depends on the experimental parameters. The line widths of the Rydberg resonances were almost three times larger (~1 cm^{-1}) than the line width of our dye laser, ≈0.3 cm^{-1} and, it remain almost constant throughout the spectrum. This enhanced line widths of the observed series may be attributed to the Doppler, power and collision broadening. In addition, at higher principal quantum number n due to the merging of 4snf $^{1,3}F_J$ series the Rydberg series gets more broadened.

Fig. 4 is a plot of principal quantum number n versus the quantum defects δ_l of the 4snf $^1F_3$ series. The quantum defects determined from the higher member series are also consistent with those calculated from the lower members $n = 26$–32 of the series [6,7]. However, at higher $n \geq 45$ the small variations in quantum defect is due to the fluctuations in the photoionization spectrum and errors in the

Table 1
Term energies (±0.25 cm^{-1}) and effective quantum numbers of the nf $^1F_3$ series in zinc.

n	This work $4s4d\,^1D_2 \xrightarrow{\hbar\omega} 4snf\,^1F_3$		Kompitsas et al. [6] $4s4p\,^1P_1 \xrightarrow{2\hbar\omega} 4snf\,^{1,3}F_J$		Brown et al. [7] $4s^2\,^1S_0 \rightarrow 4snf\,^1F_3$	
	Term energy (cm^{-1})	n^*	Term energy (cm^{-1})	n^*	Term energy (cm^{-1})	n^*
4					68,835.00	3.978
5					71,336.15	4.975
8						
9			74,044.1	7.975		
10			74,407.3	8.976		
11			74,666.7	9.976		
12			74,858.5	10.976		
13			75,004.2	11.976		
14			75,117.7	12.977		
15			75,207.6	13.977		
16			75,280.1	14.977		
17			75,339.4	15.976		
18			75,388.6	16.977		
19			75,429.7	17.975		
20	75,494.1	19.968	75,464.6	18.977		
21	75,519.7	20.967	75,494.3	19.975		
22	75,542.0	21.972	75,519.9	20.975		
23	75,561.3	22.969	75,542.1	21.976		
24	75,578.3	23.969	75,561.5	22.978		
25	75,593.3	24.969	75,578.4	23.974		
26	75,606.6	25.970	75,593.4	24.975		
27	75,618.5	26.975	75,606.7	25.976		
28	75,629.1	27.976				
29	75,638.6	28.975				
30	75,647.2	29.978				
31	75,654.9	30.970				
32	75,661.9	31.963				
33	75,668.4	32.977				
34	75,674.2	33.967				
35	75,679.6	34.975				
36	75,684.5	35.971				
37	75,689.0	36.965				
38	75,693.2	37.971				
39	75,697.0	38.956				
40	75,700.6	39.964				
41	75,703.9	40.959				
42	75,707.0	41.966				
43	75,709.9	42.978				
44	75,712.6	43.989				
45	75,715.0	44.951				
46	75,717.4	45.978				
47	75,719.6	46.984				
48	75,721.6	47.959				
49	75,723.6	48.997				
50	75,725.4	49.991				

rearranging;

$$\frac{IP-E_{(n,\ell)}-T_{(n,\ell)}}{R_{yd}a_o\langle r^{-4}\rangle_{(n,\ell)}} = \alpha_d + \alpha_q\left(\frac{\langle r^{-6}\rangle_{(n,\ell)}}{\langle r^{-4}\rangle_{(n,\ell)}}\right), \quad (5)$$

The accurate values of the term energies of the 4s*nf* $^1F_3$ series (present work) and incorporating the n^1G_4 values as reported in [22], are used for the measurement of the dipole polarizability of Zn^+ core. The *n*G states having $\ell > 3$, provides more reliable value of the dipole polarizability as reported by many authors [23–26]. The plot of the left side of Eq. (5) versus $\langle r^{-6}\rangle_{(n,\ell)}/\langle r^{-4}\rangle_{(n,\ell)}$ is a polarization graph as shown in Fig. 5. Here, the y-intercept gives the value of dipole polarizability as $\alpha_d = 18.33 \pm 0.95\ a_o^3$. The inset in Fig. 5 represents our data of the 4s*nf* $^1F_3$ series from $n = 20$–50. The uncertainty in the dipole õpolarizability is due to the uncertainty in term energies and in the ionization potential. Recently, Kutsenko et al. [22] estimated the dipole polarizability using the quantum defects of the F and G states of zinc as $18.36 \pm 0.4\ a_o^3$. Ilias and Neogrady [21] reported the dipole polarizability of Zn^+ core as 18.84 a_o^3 using the correlation model and relativistic effects. Laughlin [20] developed a ℓ-electron model of Zn^+ to evaluate the long-range asymptotic form of the polarization potential for the electron interacting with Zn^+ core, and deduce the dipole polarizability as 16.7 a_o^3 and 20.8 a_o^3. Whereas, Kompitsas et al. [6] estimated the dipole polarizability as $\alpha_d = 15.54 \pm 0.81\ a_o^3$ from the quantum defect of the 4s*nf* series, using the Vleck and Whitelaw [27] model. In this model all the polarizability arises due to the 4 s electron, neglecting the contribution from the $3d^{10}$ closed shell. Subsequently, Curtis and Theodosiou [19] used the results of Kompitsas [6] for the 4s*nf* series and theoretically determined the dipole polarizability as $\alpha_d = 15.5 \pm 0.5\ a_o^3$ with reduced uncertainty incorporating the quadruple polarization. Both Kompitsas [6] and Curtis and Theodosiou [19] ignore the closed inner-shell core, whereas this closed inner-shell core contributes further 2.296 a_o^3 in the dipole polarizability as reported by Johnson et al. [28] using the relativistic random phase calculations. Therefore, the dipole polarizability measured in the present work is in good agreement with above mentioned experimental and computational values within uncertainty.

4. Conclusion

In conclusion, we report new experimental results on the term energies and effective quantum numbers of the 4s*nf* $^1F_3$ Rydberg states of zinc from $n = 20$ to 50 using the three step laser excitation scheme, excited from the 4s4d $^1D_2$ intermediate level. The dipole polarizability of the Zn^+ core has been determined as $\alpha_d = 18.33 \pm 0.95\ a_o^3$ using the core polarization model which is in good agreement with previously reported experimental and theoretical values.

Acknowledgements

We are grateful to the Pakistan Atomic Energy Commission (PAEC) for the technical support for this work.

References

[1] D. Gullberg, U. Litzen, Accurately measured wavelengths of Zn I and Zn II lines of astrophysical interest, Phys. Scr. 61 (2000) 652–656.
[2] A. Nadeem, M. Nawaz, S.A. Bhatti, M.A. Baig, Multi-step laser excitation of the highly excited states of zinc, Opt. Commun 259 (2006) 834–839.
[3] M. Nawaz, A. Nadeem, S.A. Bhatti, M.A. Baig, Two-step laser excitation of 4s*nd* $^3D_{1,2,3}$ and 4s*ns* $^3S_1$ states from the 4s4p ^3P levels in zinc, J. Phys. B Atomic Mol. Phys. 39 (2006) 871–881.
[4] N.B. Eshkobilov, Laser spectroscopy of the Rydberg states of atoms group II B (Zn, Cd, Hg), J. Appl. Spectrosc. 67 (2000) 343–345.
[5] O. Tukhlibaev, U.Z. Alimov, Laser photoionization spectroscopy of the zinc atom and the study of zinc sulfide evaporation, Opt. Spectrosc. 88 (2000) 506–509.
[6] M. Kompitsas, C. Baharis, Z. Pan, Rydberg states of zinc and measurement of the dipole polarizability of the Zn^+ ion, J. Opt. Soc. Am. B 11 (1994) 697–702.
[7] C.M. Brown, S.G. Tilford, M.L. Ginter, Absorption spectra of Zn I and Cd I in the 1300–1750 Å region, J. Opt. Soc. Am. 65 (1975) 1404–1409.
[8] J. Sugar, A. Musgrove, Energy levels of zinc, Zn I through ZnXXX, J. Phys. Chem. Ref Data 24 (1995) 1803–1872.
[9] D.C. Hanna, P. Karkainen, R.A. Wyatt, Simple beam expander for frequency narrowing of dye lasers, Opt. Quant. Electron. 7 (1975) 115–119.
[10] N. Ahmed, A. Nadeem, M. Nawaz, S.A. Bhatti, M. Iqbal, M.A. Baig, Resistively heated high temperature atomic beam source, Rev. Sci. Instrum. 76 (2005), 063105. .
[11] W.P. Spencer, A.G. Vaidyanathan, D. Kleppner, T.W. Ducas, Photoionization by blackbody radiation, Phys. Rev. A 26 (1982) 1490–1493.
[12] K. Miculis, I.I. Beterov, N.N. Bezuglov, I.I. Ryabtsev, D.B. Tretyakov, A. Ekers, A.N. Klucharev, Collisional and thermal ionization of sodium Rydberg atoms: II. Theory for *n*S, *n*P and *n*D states with $n = 5$–25, J. Phys. B Atomic Mol. Phys. 38 (2005) 1811–1831.
[13] I.I. Beterov, D.B. Tretyakov, I.I. Ryabtsev, N.N. Bezuglov, K. Miculis, A. Ekers, A.N. Klucharev, Collisional and thermal ionization of sodium Rydberg atoms III. Experiment and theory for *n*S and *n*D states woth $n = 8$–20 in crossed atomic beams, J. Phys. B Atomic Mol. Phys. 38 (2005) 4349–4361.
[14] S.B. Zagrebin, A.V. Samson, Collisional ionization of selectively excited sodium in an atomic beam, J. Phys B: At. Mol. Phys. 18 (1985) 1217–1220.
[15] P.P. Herrmann, J. Hoffnagle, N. Schlumpf, D. Taqqu, V.L. Telegdi, A. Weis, Collisonal ionization probabilities of highly excited $S_{1/2}$, $D_{3,2}$ and $D_{5,2}$ states of cesium, J. Phys. B: At. Mol. Phys. 19 (1986) 5949–5952.
[16] I. Martinson, L.J. Curtis, S. Huldt, U. Litzen, L. Lileby, S. Mannervik, B. Jelenkovic, Lifetimes for low-lying levels in Zn I and Zn II, Phys. Scr. 19 (1979) 17–21.
[17] NIST, Atomic spectra database, version 3.0, http://www.physics.nist.gov.
[18] P. Esherick, J.A. Armstrong, R.W. Dreyfus, J.J. Wynne, Multiphoton ionization spectroscopy of high-lying, even-parity states of calcium, Phys. Rev. Lett. 36 (1976) 1296–1299.
[19] L.J. Curtis, C.E. Theodosiou, Comment on the dipole polarizability of the Zn^+ ion, J. Opt. Soc. Am. 12 (1995) 175–177.
[20] C. Laughlin, The dipole polarizability of Zn+ and the high-ℓ Rydberg levels of Zn, Z. Phys. D 39 (1997) 201–207.
[21] M. Ilias, P. Neogrady, Ionization potentials of Zn, Cd, Hg a dipole polarizabilities of Zn^+, Cd^+, Hg^+: correlation and relativistic effects, Chem. Phys Lett. 309 (1999) 441–449.
[22] A.S. Kutsenko, K.B. MacAdam, S.F. Dyubko, N.L. Pogrebnyak, Millimeter-wave spectroscopy of Zn I in $^1D_2$, $^1F_3$ and $^1G_4$ Rydberg states, J. Phys. B Atomic Mol. Phys. 48 (2015) 245005–245010.
[23] R.R. Freeman, D. Kleppner, Core polarization and quantum defects in high-angular-momentum states of alkali atoms, Phys. Rev. A 14 (1975) 1614–1619.
[24] J. Han, Y. Jamil, D.V.L. Norum, P.J. Tanner, T.F. Gallagher, Rb *nf* quantum defects from millimeter-wave spectroscopy of cold ^{85}Rb Rydberg atoms, Phys. Rev. 74 (2006), 054502. .
[25] C.J. Sansonetti, K.L. Andrew, Polarization, penetration, and exchange effects in the hydrogenlike *nf* and ng terms of cesium, J. Opt. Soc. Am. 71 (1981) 423.
[26] E.G. Kim, J. Nunkaew, T.F. Gallagher, Detection of barium 6s*ng* → 6s*nh*, 6s*ni*, and 6s*nk* microwave transitions using selective excitation to autoionizing states, Phys. Rev. 58 (2014), 06250. .
[27] J.H. Van Vleck, N.G. Whtelaw, The quantum defect of non-penetration orbits, with special application to Al II, Phys. Rev. 44 (1933) 551–569
[28] W.R. Johson, D. Kolb, K.-N Huang, Electric-dipole, quadrupole, and magnetic-dipole susceptibilities and shielding factors for closed-Shell ions of the He, Ne, Ar, Ni(Cu^-), Kr, Pb, and Xe isoelectronic sequences, At. Data Nucl Data Tables 28 (1983) 333.

SPECTROSCOPY LETTERS
2018, VOL. 51, NO. 1, 1–6
https://doi.org/10.1080/00387010.2017.1357636

Taylor & Francis
Taylor & Francis Group

Step-wise laser excitation of the 4s*nf* ^{3}F Rydberg states of neutral zinc

Mehmood Shah[a], Ghulam Aisha[b], Shaista Shahzada[b], Sami-ul-Haq[a], and Ali Nadeem[a]

[a]National Institute of Lasers and Optronics (NILOP), Islamabad, Pakistan; [b]Department of Physics, International Islamic University, Islamabad, Pakistan

ABSTRACT

The new experimental results on the effective quantum numbers and term energies of the highly excited odd-parity 4s4d $^3D_{1,2,3}$ →4s*nf* $^3F_{2,3,4}$ Rydberg transitions of zinc have been presented. The experiment was performed using the three dye lasers simultaneously pumped by the second harmonic (532 nm) of the Q-switched Nd:YAG laser. The new observation includes the 4s*nf* $^3F_3$ ($12 \leq n \leq 50$) series excited from the 4s4d $^3D_2$ intermediate level. In addition, the 4s*nf* $^3F_2$ ($12 \leq n \leq 28$) and 4s*nf* $^3F_4$ ($12 \leq n \leq 33$) series are observed from the thermally populated 4s4d $^3D_{1,3}$ fine structure components. The ionization potential of zinc has been determined from the unperturbed 4s*nf* $^3F_3$ series as $75769.31 \pm 0.15\ cm^{-1}$, which is in excellent agreement with the previously reported value.

ARTICLE HISTORY
Received 5 April 2017
Accepted 17 July 2017

KEYWORDS
Ionization potential; odd-parity states; Rydberg states; zinc

Introduction

Zinc is the lightest group II-B element, having atomic number 30. The electronic configuration of zinc consists of completely filled 4s sub shell, similar in configuration with alkaline earth atom calcium. The resonance level 4s4p $^1P_1$ of zinc lie at $46745.413\ cm^{-1}$, the ultraviolet laser at 213.9 nm is required to populate the level. However, the inter-combination 4s4p^{3}P$_1$ level at $32501.421\ cm^{-1}$ ($\lambda = 307.68$ nm) can be populated comparatively easily by frequency doubling the dye laser for the investigation of highly excited states.

The aim of the present investigation was to investigate the high orbital angular momentum ($\ell = 3$) states of zinc using multi-step laser excitation scheme from the 4s4p^{3}P multiplet. To our knowledge, the only laser based work on the bound states 4s*nf* $^{1,3}F_J$ of zinc was reported by Kompitsas et al.[1] from $n = 8$ to $n = 26$ using the multi-photon laser excitation scheme. In addition, the authors also reported the 4s*ns* $^1S_0$ ($14 \leq n \leq 31$), 4s*nd* ($12 \leq n \leq 35$), and 4s*np* ^3P ($10 \leq n \leq 40$) Rydberg series. In this paper, the detail measurements of the odd-parity spectra of zinc using the three-step laser excitation technique have been presented. The new investigation includes the term energies and effective quantum numbers of the odd parity 4s*nf* $^3F_3$ ($12 \leq n \leq 50$), 4s*nf* $^3F_2$ ($12 \leq n \leq 28$), and 4s*nf* $^3F_4$ ($12 \leq n \leq 33$) Rydberg states. The first ionization potential of zinc has been determined from the much extended 4s*nf* $^3F_3$ Rydberg series as $75769.31 \pm 0.15\ cm^{-1}$ using the extended Rydberg–Ritz relation.

Earlier, most of the papers on the investigation of highly excited states of zinc are based on the triplet p and d states. Nadeem et al.[2] reported the term energies and quantum defect of the 4s*np* $^3P_2$ ($12 \leq n \leq 60$), 4s*np* $^1P_1$ ($16 \leq n \leq 30$), and parity forbidden transitions 4s*ns* $^3S_1$ ($19 \leq n \leq 44$) and the first ionization potential of zinc as $75769.31 \pm 0.05\ cm^{-1}$. Later, Nawaz et al.[3] reported the 4s*nd* $^3D_2$ ($14 \leq n \leq 55$) and 4s*ns* $^3S_1$ ($15 \leq n \leq 35$) series from the 4s4p $^3P_1$ level. In addition, the 4s*nd* $^3D_3$ ($13 \leq n \leq 49$) and 4s*nd* $^3D_1$ ($10 \leq n \leq 20$) series were observed from the 4s4p $^3P_{2,0}$ intermediate levels, respectively. Recently, Haq et al.[4] reported the oscillator strengths of the 4s4p $^3P_1 \rightarrow$ 4s*nd* $^3D_2$ ($23 \leq n \leq 55$) Rydberg transitions of zinc along with the measurement of photoionzation cross section of the 4s4p^{3}P$_1$ state as (54 ± 8) Magabarn at the first ionization limit using the saturation absorption technique. Eshkobilov[5] reported the term energies and quantum defects of the $^3P_{0,1,2}$ series of zinc, cadmium, and mercury using three-step photoionizaion along with the first ionization potentials. Tukhlibaev and Alimov[6] reported the 4s*np* $^3P_1$ ($5 \leq n \leq 50$) Rydberg series of zinc using three-step laser excitation scheme with subsequent ionization by the pulsed electric field.

Although the first systematic studies on the bound state of Zn I and Cd I were reported by Brown et al.[7]. In zinc, they reported the principal series 4s^2 $^1S_0 \rightarrow$ 4s*np* $^1P_1$ ($4 \leq n \leq 66$), the electric quadrupole transitions 4s^2 $^1S_0 \rightarrow$ 4s*nd* $^1D_2$ ($4 \leq n \leq 20$) and the inter-combination transitions 4s^2 $^1S_0 \rightarrow$ 4s*np* $^3P_1$ ($4 \leq n \leq 12$). The first ionization limit of zinc was reported as $75769.33 \pm 0.18\ cm^{-1}$ from the much extended 4s*np* $^1P_1$ Rydberg series. Martinson et al.[8] reported the lifetimes for the low-lying levels of Zn I and Zn II using the beam-foil technique. Sugar and Musgrove[9] have compiled all the available data of the atomic energy levels of zinc form Zn I through Zn xxx. Gullberg and Litzen[10] reported the accurately measured wavelengths of Zn I and Zn II lines of astrophysical interest with a Fourier transform spectrometer using a hollow cathode as a light source. On the basis of the solar data and multi-configuration Hartree Fock (MCHF) calculation the abundance of zinc has been reassess for astrophysical interest.[11] Subsequently, the trends in copper and zinc abundance for disk and halo stars have been investigated by Senden et al.[12]

CONTACT Ali Nadeem drali_nadeem@yahoo.com National Institute of Lasers and Optronics (NILOP), P.O. Box Nilore, Islamabad 45650, Pakistan.
Color versions of one or more of the figures in the article can be found online at www.tandfonline.com/lstl.
Supplemental data for this article can be accessed on the publisher's website.

Experimental details

A schematic diagram of the experimental setup is shown in our previous paper.[13] The laser system is an injection seeded Q-switched Nd:YAG laser (Spectra Physics, PRO 230) operating at 30 Hz repetition rate and 7 ns pulse duration. The second harmonics (532 nm) was used to pump three pulsed dye lasers Hanna et al.[14] The line-width of the dye lasers was $\leq 0.3\ cm^{-1}$ and pulse energies are ≈ 10–$50\ \mu J$ depending on the wavelength. The first frequency doubled dye laser was fixed at 307.38 nm, operated with Rhodamine-610 dye dissolved in methanol to populate the 4s4p $^3P_1$ level. The second dye laser was charged with DCM dye dissolved in methanol and frequency doubled to populate the 4s4d $^3D_2$ level at 330.35 nm. Frequency doubling of both the dye lasers were achieved by focusing the laser into Beta Barium Borate (BBO) type-I crystals (6 mm long, cut at 40° with respect to optic axis). The third dye laser was operated with LDS-798 dye dissolved in methanol and was scanned to cover the wavelength region (867–825 nm) up to the ionization potential of zinc. The dye lasers wavelengths were measured with a spectrometer (Ocean Optics, HR-4000, 200–1100 nm and 0.75 nm resolution) equipped with a 600 lines mm^{-1} grating. All the three dye laser beams were linearly polarized and spatially overlapped in the middle of the thermionic diode ion detector.

The zinc vapors were confined in a cylindrical heat pipe, operating as a thermionic diode ion detector working in the space charge limited mode.[15,16] The thermionic diode detector consists of a 35 cm long stainless-steel pipe of 3 cm outer diameter and 2 mm wall thickness. Thermo-coax wire was non-inductively wound onto a heat pipe for heating and an active zone in the middle was 10 cm long. The temperature was kept at about $820 \pm 2\%$ K and it was maintained through nickel–chromium–nickel (Ni–Cr–Ni) thermocouple using a temperature controller. Both ends of the pipe were water cooled and sealed with 25 mm diameter quartz windows. A single molybdenum wire, 25 cm in length and 0.25 mm diameter, extending along the axis of the pipe was used as a cathode which was heated by a separate direct current power supply operated at 2 A to enhance the ionization signal. About 5 g of zinc sample along with a small amount of potassium (to reduce the work function of the cathode) was loaded in a stainless-steel boat that was placed in the middle of the heat pipe which after evacuation was filled with argon gas at a pressure of 3 and 10 mbar. The change in the thermionic diode current due to the photoionization was measured as a voltage drop across a 100 kΩ load resistor. The spectra were recorded by tuning the third dye laser, and for the wavelength calibration a portion of the dye laser was sent into a argon filled hollow cathode lamp to record the well distributed spectra of argon and another small fraction onto the 1-mm thick solid etalon and interference fringes (free spectral range $3.333\ cm^{-1}$) were recorded using a photodiode. The optogalvanic signals serve as wavelength standards and the interference fringes from etalon were used to interpolate between the argon lines. These three signals were simultaneously sampled using three independent gated integrator boxcar (SR-250) averagers. The SR-245 computer interface module was used for data acquisition; which provides analog to digital interface through a GPIB-PC IIA NI 488 card. The spectra were recorded and stored on a computer for analysis.

Results and discussion

Three-step laser excitation scheme to investigate the odd-parity states of zinc is shown in Figure 1. The first dye laser was fixed at $32501.399\ cm^{-1}$ to populate the 4s4p $^3P_1$ intermediate level, the second dye laser was fixed at $62772.014\ cm^{-1}$ to populate the 4s4d $^3D_2$ level and the third laser was scanned from 867 to 825 nm range up to the first ionization threshold. The life time of the 4s4d $^3D_2$ level is 5.4 ± 0.6 ns[8] therefore; the third dye laser was fed into the thermionic diode without any delay. The selective excitation process at each step was ensured by blocking any of the excitation beams and monitoring the corresponding ion signal.

$$4s^2\,{}^1S_0 \xrightarrow{307.38nm} 4s4p\,{}^3P_1 \xrightarrow{330.35nm} 4s4d\,{}^3D \xrightarrow{867-825nm} 4snf\,{}^3F$$

Since the first dye laser is linearly polarized, the populated state in the 4s4p $^3P_1$ level is mj = 0. The second dye laser is also linearly polarized with the polarization vector parallel to that of the first step laser and it was tuned to populate the 4s4d $^3D_2$ level with mj = 0. In the third excitation step, the atoms from the 4s4d $^3D_{1,2,3}$ levels have been promoted to the 4s*nf* $^3F_{2,3,4}$ levels. Interestingly, the transitions were observed from all the three fine structure components; 4s4d $^3D_{1,2,3}$ despite the third laser was tuned from the 4s4d $^3D_2$ level.

In Figure 2, a portion of zinc spectrum is shown covering the term energy range from 75,240 to 75,506 cm^{-1} excited from the 4s4d ^3D multiplet. The top trace is the optogalvanic spectra of argon for wavelength calibration and the middle one shows the interference fringes from a 1-mm thick solid etalon and the bottom trace is the ionization signals of zinc from the thermionic diode ion detector. This portion of the spectrum looks a bit complicated due to the presence of all the possible excitations from the 4s4d $^3D_{1,2,3}$ intermediate levels. The thermal energy of the zinc atoms in the thermionic diode is $\sim 570\ cm^{-1}$ corresponding to the 820 K temperature, therefore, all the fine structure components 4s4d $^3D_{1,2,3}$ also got populated. Consequently, observed all the allowed transitions from

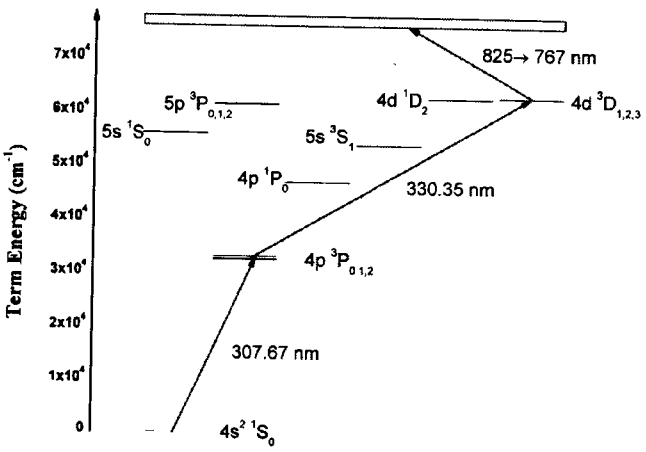

Figure 1. Three-step laser excitation scheme to investigate the odd-parity 4s*nf* ^3F Rydberg states of zinc.

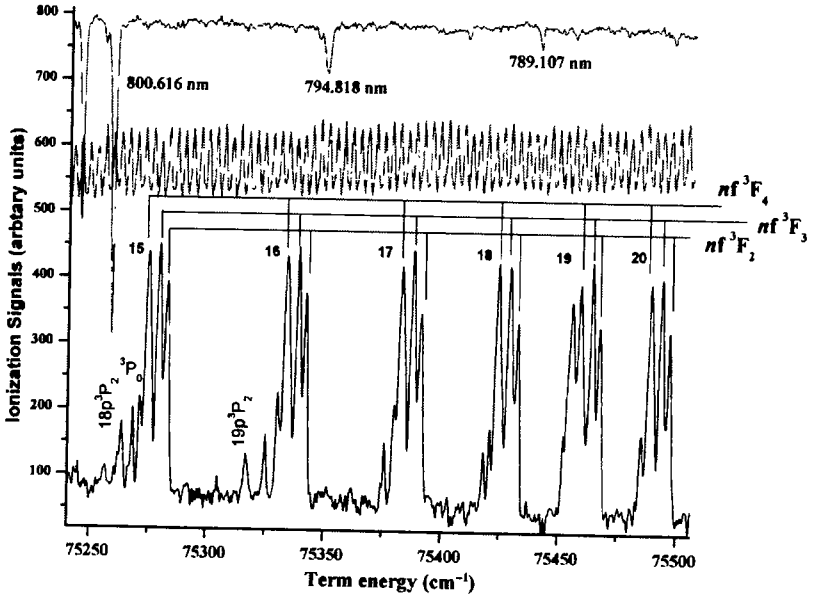

Figure 2. The spectrum of zinc covering the energy region 75240–75506 cm^{-1} showing the 4s4d $^3D_{1,2,3}$ → 4s*nf* $^3F_{2,3,4}$ Rydberg series from n = 15 to 20.

the 4s4d ^3D multiplet to the 4s*nf* $^3F_{2,3,4}$ levels in the present work. The accessible series from the 4s4d $^3D_{1,2,3}$ intermediate levels are 4s*nf* $^3F_{2,3,4}$ and 4s*np* $^3P_{0,1,2}$ according to the electric dipole selection rules ($\Delta\ell = \pm 1$, $\Delta J = 0 \pm 1$, $0 \leftrightarrow 0$ forbidden). The 4s*nf* $^3F_{2,3,4}$ Rydberg levels were observed with good intensity, whereas, the 4s*np* $^3P_{0,1,2}$ adjacent Rydberg series possessing lower intensities. The 4s18p $^3P_{1,2}$ and 19p levels are resolved and the 4s4p $^3P_0$ series appears as shoulder to the main 4s15f $^3F_4$ series and almost merge at 17f. The relatively high intensity series is assigned as 4s*nf* $^3F_3$ ($15 \leq n \leq 20$) excited from the 4s4d $^3D_2$ intermediate level. The adjacent series at the lower energy side of the main series is identified as 4s*nf* $^3F_4$ ($15 \leq n \leq 20$) excited from the 4s4d $^3D_3$ level and the lines on the higher energy side are identified as 4s*nf* $^3F_2$ series ($15 \leq n \leq 20$) excited from the 4s4d $^3D_1$ level. The assignments of these series are in accordance to the electric dipole selection rules, following the electric dipole intensity selection rules the more favorable transitions are that which follow the $\Delta\ell = \Delta L = \Delta J = +1$ selection rules. Therefore, from the 4s4d $^3D_2$ intermediate level the most probable transitions are 4s*nf* $^3F_3$. Similar arguments are valid for the 4s*nf* $^3F_4$ and 4s*nf* $^3F_2$ series. The relative intensities of the 4s*nf* $^3F_{2,4}$ series also imitate the relative populations of the 4s4d $^3D_3$ and 4s4d $^3D_1$ intermediate levels as these were thermally or collisionally populated. Furthermore, it is noticed that the energy separation among the main 4s*nf* $^3F_3$ series and the adjacent

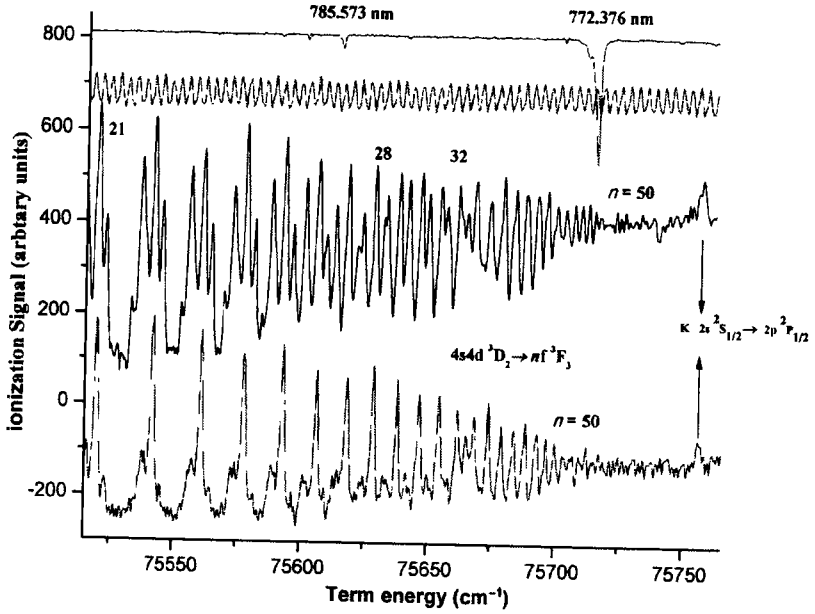

Figure 3. The higher members of the 4s*nf* $^3F_{2,3,4}$ series converging to the first ionization limit covering the energy range 75450–75800 cm^{-1}. The top spectrum are the photoionization signals recorded at higher vapor pressure ≈10 mbar in which all the fine structure components of 4s4d $^3D_{1,2,3}$ are populated and lower spectrum was recorded at low pressure showing the 4s*nf* $^3F_3$ transitions excited from the 4s4d $^3D_2$.

Table 1. The term energies (± 0.25 cm^{-1}) and effective quantum number (n^*) of the 4s*nf* $^3F_{2,3,4}$ Rydberg series observed in the present work. The previously reported data of the term energies and the n^* from $n = 8$–26 reported by Kompitsas et al.[1] and by Sugur and Musgore[9] from $n = 4$–7 are also listed. The term energy calculated using Rydberg–Ritz relation and in the last column difference between calculated and experimental values.

	4s4d $^3D_1 \rightarrow$ 4s*nf* $^3F_2$		4s4d $^3D_2 \rightarrow$ 4s*nf* $^3F_3$		4s4d $^3D_3 \rightarrow$ 4s*nf* $^3F_4$		Kompitsas et al.[1] 4s4p $^1P_1 \rightarrow$ 4s*nf*$^{1,3}F_J$		Sugur and Musgore[9] 4s4p $^3P \rightarrow$ 4s*nf* $^3F_{2,3,4}$		Calculated Term energy	
n	Term energy cm^{-1}	n^*	Term energy cm^{-1}	n^*	Term energy cm^{-1}	n^*	Term energy cm^{-1}	n^*	Term energy cm^{-1}	n^*	cm^{-1} 4s4d $^3D_2 \rightarrow$ 4s*nf* $^3F_3$	Expt–Calc.
4	–	–	–	–	–	–		–	68833.79	3.978		
5	–	–	–	–	–	–	–	–	68833.93	4.975		
6	–	–	–	–	–	–	–	–	68834.04	5.970		
7	–	–	–	–	–	–	–	–	71335.6	6.953		
8	–	–	–	–	–	–	74044.1	7.975	72690.8			
9	–	–	–	–	–	–	74407.3	8.976	73499.5			
10	–	–	–	–	–	–	74666.7	9.976				
11	–	–	–	–	–	–	74858.5	10.976				
12	75003.84	11.973	75003.84	11.973	75003.73	11.972	75004.2	11.976				
13	75117.06	12.971	75117.07	12.971	75117.1	12.971	75117.7	12.977				
14	75206.97	13.969	75207.00	13.969	75206.98	13.969	75207.6	13.977				
15	75279.73	14.971	75279.53	14.968	75279.83	14.973	75280.1	14.977				
16	75338.9	15.967	75338.95	15.968	75339.08	15.970	75339.4	15.976				
17	75388.06	16.965	75387.97	16.963	75388.18	16.968	75388.6	16.977				
18	75429.48	17.969	75429.33	17.965	75429.44	17.968	75429.7	17.975				
19	75464.19	18.964	75464.29	18.967	75464.27	18.966	75464.6	18.977				
20	75494.25	19.973	75494.16	19.970	75494.21	19.972	75494.3	19.975				
21	75519.69	20.966	75519.8	20.971	75519.72	20.967	75519.9	20.975				
22	75541.82	21.962	75542.93	22.016	75542.05	21.973	75542.1	21.976				
23	75561.34	22.970	75561.4	22.973	75561.39	22.972	75561.5	22.978				
24	75578.31	23.968	75578.26	23.965	75578.39	23.973	75578.4	23.974				
25	75593.29	24.967	75593.3	24.968	75593.23	24.963	75593.4	24.975				
26	75606.59	25.967	75606.59	25.967	75606.53	25.963	75606.7	25.976				
27	75618.64	26.986	75618.41	26.965	75618.48	26.971						
28	75629.06	27.970	75629.06	27.970	75629.06	27.970						
29			75638.5	28.962	75638.57	28.969						
30			75647.11	29.964	75647.1	29.963						
31			75654.84	30.959	75654.96	30.976						
32			75661.84	31.952	75661.96	31.969						
33			75668.37	32.969	75668.24	32.947						
34			75674.21	33.966								
35			75679.52	34.955								
36			75684.4	35.946								
37			75688.09	36.753								
38			75693.18	37.961								
39			75697.06	38.967								
40			75700.6	39.96								
41			75703.8	40.95								
42			75707.1	41.99								
43			75709.8	42.96								
44			75712.6	43.99								
45			75715.1	44.97								
46			75717.4	45.97								
47			75719.6	46.99								
48			75721.7	47.99								
49			75723.6	48.97								
50			75725.4	49.98								
											75003.85	−0.01
											75117.06	0.01
											75206.97	0.03
											75279.53	−0.00
											75338.92	0.03
											75388.14	−0.15
											75429.39	−0.06
											75464.28	0.01
											75494.07	0.09
											75519.70	0.10
											75541.91	0.02
											75561.29	0.11
											75578.28	−0.02
											75593.28	0.02
											75606.58	0.01
											75618.43	−0.02
											75629.03	0.03
											75638.55	−0.05
											75647.13	−0.02
											75654.90	−0.06
											75661.94	−0.10
											75668.36	0.01
											75674.22	−0.01
											75679.58	−0.06
											75684.50	−0.10
											75689.03	0.06
											75693.20	−0.02
											75697.06	0.00
											75700.63	−0.02
											75703.94	−0.06
											75707.02	0.08
											75709.89	−0.01
											75712.56	0.06
											75715.06	0.00
											75717.39	0.03
											75719.58	0.04
											75721.64	0.05
											75723.56	0.01
											75725.38	0.01

series on the lower as well as higher energy side remain constant. These spacing are in accordance with the energy separation between the fine structure components of the 4s4d ^{3}D multiplets; $^3D_3 - {}^3D_2 = 4.967\ cm^{-1}$ and $^3D_2 - {}^3D_1 = 3.267\ cm^{-1}$ as reported by Gullberg and Litzen.[10] The constant energy separations among the observed series enabled us to assign these series unambiguously.

In Figure 3 the higher members of the Rydberg series of zinc in the 75,450–75,800 cm^{-1} energy range up to the first ionization threshold have been presented. The upper spectra were recorded at a relatively higher buffer gas pressure ≈10 mbar, in this case all the fine structure components of 4s*n*d $^3D_{1,2,3}$ got populated due to the collisional energy transfer. The bottom trace was recorded at a reduced pressure ≈3 mbar, in this case the excitation spectra are observed only from the 4s*n*d $^3D_2$ intermediate state. The 4s*n*f $^3F_3$ series has been followed up to $n = 50$. The 4s*n*f $^3F_4$ and 4s*n*f $^3F_2$ series appears as shoulders to the dominating 4s*n*f $^3F_3$ series and have been resolved up to $n = 28$ and $n = 32$ respectively. Analysis of the 4s*n*f $^3F_{2,3,4}$ series have been performed using subroutine that takes into account the argon reference wavelengths and the interference fringes from the etalon and yields the laser excitation energies of all the unknown levels. The term energies were calculated by adding the intermediate level energies 4s4d $^3D_1$ 62768.747 cm^{-1}, 4s4d $^3D_2$ 62772.014cm^{-1}, and 4s4d $^3D_3$ 62776. 981 cm^{-1} in the laser excitation energies of the 4s*n*f $^3F_{2,3,4}$ series, respectively.

The 4s*n*f $^3F_3$ series has been observed up to $n = 50$, therefore, Rydberg–Ritz formula was used on the experimentally determined term energies to determine the first ionization potential of zinc and the corresponding quantum defects:

$$E_n = E_i - \frac{\text{Ryd}}{\left[n - a\frac{b}{(n-a)^2} - \frac{c}{(n-a)^4} - \cdots\right]^2} \quad (1)$$

The mass corrected Rydberg constant Ryd is determined as:

$$\text{Ryd} = R_\infty(1 + m/M_{Zn})^{-1} = 109736.404\ cm^{-1}$$

The δ_ℓ is the quantum defect and *a*, *b*, and *c* are the Rydberg–Ritz coefficients:

$$\delta_\ell = a + \frac{b}{(n-a)^2} + \frac{c}{(n-a)^4} \quad (2)$$

A least square fit on the transition energies of the 4s*n*f $^3F_3$ series yields the series convergence limit as $12997.29 \pm 0.02\ cm^{-1}$, and the Ritz coefficients $a = 0.0317$, $b = 1.3324$, and $c = -290.4811$. By adding the series convergence limit (binding energy) of the 4s4d $^3D_2$ level as determined above to the energy of 4s4d $^3D_2$ level 62772.014 cm^{-1} as reported by Sugar and Musgrove.[9] The first ionization potential of zinc is determined as $75769.31 \pm 0.15\ cm^{-1}$, this is in excellent agreement with the previously reported value.[3] The Ritz coefficients *a*, *b*, and *c* were substituted in Eq. (2) and quantum defect was determined as 0.029 ± 0.005. For the verification of the experimentally determined term energies, the term energies were also calculated using the Rydberg–Ritz coefficients using Eq. (1) as listed in the 12th column of Table 1. Table 1 consists of the term energies, principal quantum number *n* and effective quantum number n^* of the 4s*n*f $^3F_{2,3,4}$ Rydberg series. It also contains the term energies of the previously reported work,[1,9] and the difference in $E_{(experimental)} - E_{(calculated)}$ term energies of the 4s*n*f $^3F_3$ series. Figure 4 shows the plot of the $E_{(experimental)} - E_{(calculated)}$ versus the principle quantum number *n*, the energy difference is well within the quoted uncertainty in the present work.

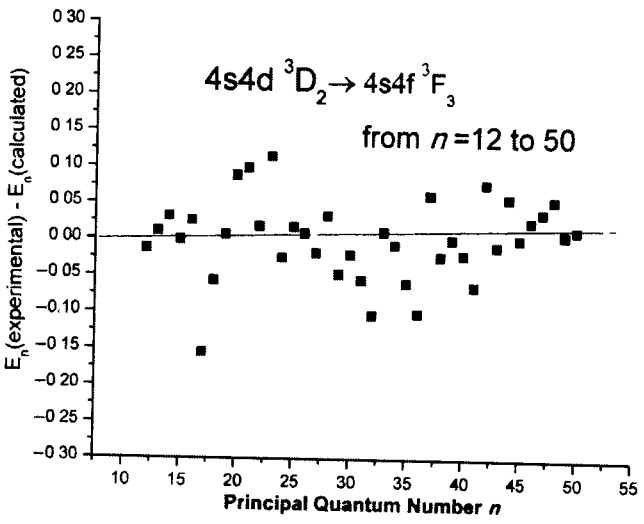

Figure 4. The plot of the term energies difference between the experimental values of 4s*n*f $^3F_3$ from $n = 12$ to 50 and the calculated term energies using the Rydberg Ritz relation Eq. (1). The difference in term energies is plotted versus principal quantum number *n*. The energy difference $E_{(experimental)} - E_{(calculated)}$ is within the quoted uncertainty in term energy (±0.25 cm^{-1}) versus principal quantum number *n*.

The last member of the 4s*n*f $^3F_3$ series was observed up to $n = 50$, and lies only 30 cm^{-1} below the ionization limit. The Rydberg states can be further extended close to the ionization limit by minimizing the electric field in the detector and using a narrow line width dye laser. Furthermore, it is observed that the line widths of the 4s4d $^3D_2$→ 4s*n*f $^3F_3$ transitions of zinc are approximately 1.8 (2) cm^{-1}, which is larger than the line width of our dye laser, ≈0.3 cm^{-1}. This enhanced line widths are due to many factors in the experimental work, such as the Doppler broadening, collisional broadening, pressure broadening and Stark broadening. In addition, at higher *n* all the components of 4s*n*f $^3F_{2,3,4}$ multiplet starts merging and consequently the transitions are broadened.

The analysis of the observed 4s*n*f $^3F_{2,3,4}$ series reveals that the quantum defects are almost constant as a function of principal quantum number *n*. The levels that might perturb the triplet discrete structure are either attached to the double excitation or inner-shell excitations. In zinc, all the doubly excited states based on the $4p^2$ configuration or due to the 3d-subshell excitation that lie above the first ionization threshold consequently, the series perturbations are negligible. Whereas, in the homologous element calcium the doubly excited configurations 3d5s and $3d^2$ $^1D_2$ lie below the threshold which perturb the principle series Esherick et al.[17] Therefore, it is suggested that the unperturbed *n*f-series in zinc, cadmium and mercury are the best candidates for the determination of the first ionization potential of these elements.

The estimated uncertainties in the term energies are ±0.25 over the whole spectral range. The intermediate level is known to 0.02 cm^{-1},[9] the laser line width is ≤0.3 cm^{-1}, and the

reference wavelengths are known within 0.0001 nm[18] and in the measurement of FSR 100 ± 0.01 GHz and a single step in the scanning dye laser stepper motor is $0.04 cm^{-1}$, therefore, from the location of the peak signal positions the term energies have been determined within the above mentioned accuracy.

Conclusion

The high orbital angular momentum ($\ell = 3$) states of zinc $4snf\ ^3F_3$ have been investigated for the first time up to much higher principal quantum number $n = 50$. Furthermore, the $4snf\ ^3F_2$ and $4snf\ ^3F_4$ series were observed up to $n = 28$ and $n = 33$, respectively, from the $4snd\ ^3D_{1,3}$ thermally populated states in thermionic diode ion detector. Having observed the transitions from all the fine structure components of the 4s4d ^3D multiplet the J-values assignment has been made explicitly. Prior to this studies the only available data on the high orbital angular momentum studies ($\ell = 3$) states of $4snf\ ^{1,3}F_3$ states from the $n = 8$ to $n = 26$. Therefore, the present experimental work has extended the previous investigations of the $4snf\ ^3F_{2,3,4}$ states of zinc. The accurate wavelengths of the above-mentioned results of zinc are valuable for the investigation of the dynamics of stellar atmosphere. Moreover, using the accurate laboratory scale data of zinc the signature of zinc in solar and stellar atmosphere can be determined.

Funding

We are grateful to the Pakistan Atomic Energy Commission (PAEC) for the financial support for this work.

References

[1] Kompitsas, M.; Baharis, C.; Pan, Z. Rydberg states of zinc and measurement of the dipole polarizability of the Zn^+ ion. *Journal of the Optical Society of America B* **1994**, *11*, 697–702.

[2] Nadeem, A.; Nawaz, M.; Bhatti, S. A.; Baig, M. A. Multi-step laser excitation of the highly excited states of zinc. *Optics Communications* **2006**, *259*, 834–839.

[3] Nawaz, M.; Nadeem, A.; Bhatti, S. A.; Baig, M. A. Two-step laser excitation of $4snd\ ^3D_{1,2,3}$ and $4sns\ ^3S_1$ states from the 4s4p ^3P levels in zinc. *Journal of Physics B: Atomic, Molecular and Optical Physics* **2006**, *39*, 871–881.

[4] Haq, S. U.; Nadeem, A.; Nawaz, M.; Baig, M. A. Oscillator strength measurements of the highly excited 4s4p $^3P_1 \rightarrow$ $4snd\ ^3D_2$ transitions of zinc. *Journal of the Optical Society of America B* **2010**, *27*, 402–407.

[5] Eshkobilov, N. B. Laser spectroscopy of the Rydberg states of atoms group II B (Zn, Cd, Hg). *Journal of Applied Spectroscopy* **2000**, *67*, 343–345.

[6] Tukhlibaev, O.; Alimov, U. Z. Laser photoionization spectroscopy of the zinc atom and the study of zinc sulfide evaporation. *Optics and Spectroscopy* **2000**, *88*, 506–509.

[7] Brown, C. M.; Tilford, S. G.; Ginter, M. L. Absorption spectra of Zn I and Cd I in the 1300–1750 Å region. *Journal of the Optical Society of America* **1975**, *65*, 1404–1409.

[8] Martinson, I.; Curtis, L. J.; Huldt, S.; Litzen, U.; Lileby, L.; Mannervik, S.; Jelenkovic, B. Lifetimes for low-lying levels in Zn I and Zn II. *Physica Scripta* **1979**, *19*, 17–21.

[9] Sugar, J.; Musgrove, A. Energy levels of zinc, Zn I through Zn xxx. *Journal of Physical and Chemical Reference Data* **1995**, *24*, 1803–1872.

[10] Gullberg, D.; Litzen, U. Accurately measured wavelengths of Zn I and Zn II lines of astrophysical interest. *Physica Scripta* **2000**, *61*, 652–656.

[11] Biemont, E.; Godefroid, M. A reassessment of the zinc solar abundance. *Astronomy and Astrophysics* **1980**, *84*, 361–363.

[12] Senden, C.; Gratton, R. G.; Croker, D. A. Trends in copper and zinc abundance for disk and halo stars. *Astronomy and Astrophysics* **1991**, *246*, 354–367.

[13] Nadeem, A.; Shah, M.; Haq, S. U.; Shahzada, S.; Mumtaz, M.; Waheed, A.; Nawaz, M.; Ahmed, M.; Baig, M. A. Three-step laser excitation of the odd-parity 5s5d $^3D \rightarrow 5\ snf\ ^3F$ states of cadmium. *The European Physical Journal D* **2014**, *68*, 192.

[14] Hanna, D. C.; Karkainen, P.; Wyatt, R. A simple beam expander for frequency narrowing of dye lasers. *Optical and Quantum Electronics* **1975**, *7*, 115–119.

[15] Thompson, D. C.; Stoicheff, B. P. Study of the charteristics of thermionic ionization detector. *Review of Scientific Instruments* **1982**, *53*, 822–828.

[16] Niemax, K. Spectroscopy using thermionic diode detectors. *Applied Physics B* **1985**, *38*, 147–157.

[17] Esherick, P.; Armstrong, J. A.; Dreyfus, R. W.; Wynne, J. J. Multiphoton ionization spectroscopy of high-lying, even-parity states of calcium. *Physical Review Letters* **1976**, *36*, 1296–1299.

[18] Kramida, A.; Ralchenko, Yu.; Reader, J.; NIST ASD Team. (2017). NIST Atomic Spectra Database (ver.5.5.1) [Online]. Available: https://physics.nist.gov/asd [2017, March 15]. National Institute of Standard and Technology, Gaithersburg, MD.

SPECTROSCOPY LETTERS
2019, VOL. 52, NO. 2, 143–149
https://doi.org/10.1080/00387010.2019.1593195

Oscillator strength measurements of the 4s5s $^3S_1 \rightarrow$ 4s*n*p $^3P^o_2$ Rydberg transitions of zinc

Ghulam Aisha[a], Mehmood Shah[b], Ali Nadeem[b], Sami-Ul Haq[b], and Shaista Shahzada[a]

[a]Department of Physics, International Islamic University, Islamabad, Pakistan; [b]National Institute of Lasers and Optronics (NILOP), Islamabad, Pakistan

ABSTRACT

In the present experimental work, oscillator strengths of the 4s5s $^3S_1 \rightarrow$ 4s*n*p $^3P^o_2$ ($18 \leq n \leq 53$) Rydberg transitions of zinc are reported. The stepwise laser excitation from the ground state $4s^2$ $^1S_0$ was achieved using three dye laser beams simultaneously pumped by the second (532 nm) and third (355 nm) harmonics of a Q-switched Nd: YAG (Neodymium-doped yttrium aluminum garnet) laser. The vapor containment and detection system was a single wire thermionic diode ion detector operating in space charge limited mode. A trend of the above-mentioned *f*-values from $n = 18$ to 53 versus the principle quantum number *n* has been presented. Furthermore, continuity has been verified between the discrete *f*-values and the oscillator strength density at the threshold.

ARTICLE HISTORY
Received 3 June 2018
Accepted 6 March 2019

KEYWORDS
Oscillator strength; Rydberg states; step-wise excitation; zinc

Introduction

In atomic physics, energy levels, oscillator strengths, lifetimes and photoionization cross-sections are the fundamental atomic parameters. The energy levels of zinc (Zn I) were extensively investigated using the conventional and laser excitation schemes.[1–7] However, the detailed investigation of the oscillator strength of the Rydberg transitions of zinc is still missing in the literature. Therefore, the aim of the present investigation was to experimentally determine the oscillator strengths of the 4s5s $^3S_1 \rightarrow$ 4s*n*p $^3P^o_2$ ($18 \leq n \leq 53$) Rydberg transitions of Zn I. Oscillator strengths are important in astrophysics as they play a vital role in the determination of the atomic abundance. They are also very important in thermonuclear research where the atomic radiation is the major loss mechanism.

Over the past few decades, almost all the theoretical as well as experimental investigations on the oscillator strengths of zinc were based on the low-lying principal series of zinc using several techniques.[8–10] Kerkhoff et al.[11] reported the radiative lifetimes of the 4s*n*s $^3S_1$ ($n = 5$–7) and 4s*n*d $^3D_3$, $^3D_2$ and $^3D_1$ ($n = 4 - 6$) states excited from the 4s4p^{3}P^o states and also reported the oscillator strengths of the 4s*n*s $^3S_1$ ($n = 5$–7) $\rightarrow$ 4p*m*p ^3P ($m = 4$, 5) and 4s*n*d ^3D ($n = 4$–6) $\rightarrow$ 4p*m*p ^3P ($m = 4,5$) low-lying transitions. Ueda et al. [12] applied the hook method to measure the oscillator strengths of the 4s4p $^3P^o_{0,1,2} \rightarrow$ 4p^2 $^3P_{0,1,2}$ auto-ionizing resonances. Subsequently, Ueda et al.[13] reported the absorption and dispersion studies of the 4s4p $^3P^o \rightarrow$ 4p^2 ^3P multiplet of Zn I. Afanaseva[14,15] reported the oscillator strengths of the 4s4p $^1P^o_1 \rightarrow$ 4s*n*d $^1D_2$ ($4 \leq n \leq 20$) transitions and the 4s4p $^1P^o_1 \rightarrow$ 4p^2 $^1D_2$ auto-ionizing resonance using the two-channel quantum defect theory. Recently, Haq et al.[16] reported the oscillator strengths for the 4s4p $^3P^o_1 \rightarrow$ 4s*n*d $^3D_2$ Rydberg transitions of zinc from $n = 23$ to 55 and a smooth connection between discrete oscillator strengths and oscillator strength density at threshold has been established.

Theoretically, Brian Warner[17] first time determined the oscillator strengths of the few elements including zinc for the $s^2 \rightarrow$ sp and ss $\rightarrow$ sp transitions using the Thomas-Fermi-Dirac wavefunctions. Zilitis[18] computed the oscillator strengths of the resonance transitions of group-II elements using Hartree-Fock wavefunctions. Luc-Koenig[19] calculated the transition probabilities of the $^3P^o_1 \rightarrow {}^1S_0$ transitions of group II elements. Glowacki and Migdalek[20,21] reported the oscillator strengths of the spin-allowed and spin forbidden ns^2 $^1S_0 \rightarrow$ *ns*n*p* $^{1,3}P^o_1$ transitions of (Zn, Sr, Ba, Cd, Hg, and Yb) using the relativistic configuration interaction method. Brage and Fischer[22] reported the core polarization effects on the oscillator strength of the resonance transitions of Zn I using the multi-configuration Hartree-Fock approach. Later, Chen and Cheng[23] computed the excitation energies of the $4s^2 \rightarrow$ 4s4p transitions using the relativistic configuration interaction (CI) calculations.

In the present contribution, oscillator strengths of the 4s5s $^3S_1 \rightarrow$ 4s*n*p $^3P^o_2$ highly excited transitions from $n = 18$–53 are reported. In addition, a smooth connection between the oscillator strengths distribution in the discrete region and the oscillator strength density at threshold have been verified.

CONTACT Shaista Shahzada shaista.shahzada@iiu.edu.pk Department of Physics, International Islamic University, Sector- H-10, Islamabad, 44000, Pakistan
Color versions of one or more of the figures in the article can be found online at www.tandfonline.com/lstl.

Experimental details

A schematic diagram of the experimental set-up is shown in Fig. 1. Briefly, the laser system is an injection seeded Q-switched Nd: YAG (PRO-230 Spectra Physics) laser having 30 Hz repetition and 7 ns pulse duration. The second (532 nm) and third (355 nm) harmonics of the laser were used to pump three Hanna type[24] dye lasers. The pulse energy of the dye lasers was approximately in the range of 0.4–0.6 mJ. The energy of the dye lasers was measured using the energy meter (Top Max II, Coherent). The line width of the dye lasers was typically $\leq 0.3\,cm^{-1}$. The first step dye laser was pumped by the second harmonic of the Nd: YAG laser using the R-610 dye and its output was frequency doubled using BBO type-I crystal ($6 \times 4 \times 7$ mm, 40° cut along the optical axis). It was adjusted to excite the 4s4p $^3P^o_1$ level of zinc at 307.7 nm.[6] The second step dye laser was pumped by the third harmonic using the LD-466 dye to populate 4s5s $^3S_1$ level at 472.4 nm.[6] The third dye laser was scanned from 478–452 nm range to investigate the highly excited states of zinc adapting the following laser excitation scheme:

$$4s^2\ {}^1S_0 \xrightarrow{307.7\,nm} 4s4p\ {}^3P^o_1 \xrightarrow{472.4\,nm} 4s5s\ {}^3S_1 \xrightarrow{478-452\,nm} 4snp\ {}^3P^o_2$$

The step-wise laser excitation process was verified by blocking any of the excitation laser beam and observing the photo-ionization signal. The lifetime of the 4s4p $^3P_1$ level was not reported in the literature, therefore, to ensure the two-step excitation, the second dye laser was delayed by few nanosecond. However, the lifetime of the 4s5s $^3S_1$ intermediate level is reported as 8.0 ns.[25,26] Therefore, the third scanning dye laser was sent almost simultaneously with second dye laser. The wavelengths of the dye lasers were measured with a spectrometer (Ocean Optics, HR-4000, spectral range 200–1100 nm and resolution 0.75 nm) equipped with a 600 lines/mm grating. The dye laser beams were fed into the thermionic diode from opposite sides and their spatial overlap was ensured in the central region.

The zinc vapors were produced in a thermionic diode ion detector, its working principle was described in detail by Niemax et al.[27]. The heat pipe was a stainless steel pipe of 35 cm long and 3 cm internal diameter. A thermocoax wire was wrapped around the central region of the pipe and heated with a DC power supply. Both the ends of heat pipe were water cooled and sealed with 3 cm diameter quartz windows. The central heating zone was 20 cm long, was kept at a temperature of ≈450–500 °C monitored by a Ni–Cr–Ni thermocouple. A thick tungsten wire of 0.25 mm diameter was stretched axially along the cylindrical anode acts as a cathode. Small amount of zinc ingots (≈5g) along with a small amount of potassium (to reduce the work function of the tungsten cathode) was placed in the central heating region. The heat pipe was initially evacuated down to 10^{-6} mbar using a combination rotary and diffusion pumps. Then, heat pipe was filled with argon gas at a pressure of ≈10 mbar to reduce the vapor diffusion. The cathode wire was heated by a separate regulated power supply capable of delivering 1–5 A. Due to the low work function of the cathode wire, thermionic emission takes place and space charge is built around the wire, and the diode current is restricted by the electron space charge, and it operates in space charge limited mode. When the dye lasers pass through the space charge region and excites the zinc atoms into Rydberg states which are further ionized by collisions with buffer gas atoms or by electron impact. The change in the diode current due to the photo-ion production was measured as a voltage drop across a 100 kΩ resistor.

The wavelength calibration was achieved by simultaneously recording the optogalvanic spectra of neon by inserting a small portion (≈10%) of the scanning dye laser beam into the commercial hollow cathode lamp filled with neon gas at a low pressure. In a gas discharge, most of the lower excited states gets populated by electron impact excitation. As the small portion of the scanning dye laser beam passes through the discharge and its wavelength matches between levels of atoms, the population densities are changed, this population change will result in a change in the discharge current and is detected as a voltage change across the load resistor R. The etalon fringes were recorded by directing the 10% of the scanning dye laser beam towards diverging lens followed by a 1 mm thick solid etalon and fringe pattern was recorded by a photodiode (PBX 65) which provides absolute frequency marker. Finally, three signals from thermionic diode ion detector, hollow cathode lamp, and photodiode were sampled simultaneously using three Box Car Averagers (*SR*-250) interfaced through a GPIB card. The data were recorded on a personal computer for further analysis. The wavelengths of the unknown zinc spectra were determined using a subroutine that takes into account the neon reference wavelengths and the interference fringes from the etalon and yields the energies of all the unknown levels. The term energies were determined by adding the laser excitation energies of the 4s*n*p $^3P^o_2$ series and the intermediate level energy 4s5s $^3S_1$ as $53672.240\,cm^{-1}$[6] with the estimated uncertainties of $\pm\ 0.3\,cm^{-1}$.

Results and discussion

The photo-excitation spectrum of Zn I from 75590–75770 cm^{-1} energy range is shown in Fig. 2 excited from the 4s5s $^3S_1$ intermediate state. According to the Russell-Saunders or LS Coupling scheme, the accessible series from the intermediate level (4s5s $^3S_1$) are 4s4p $^3P^o_{0,1,2}$. However, if the $\Delta S = 0$ selection rule is relaxed, the spin forbidden 4s4p $^1P^o_1$ transition can be observed confirming the departure from LS coupling for high Z elements. In the observed spectrum, the dominating series is assigned as 4s*n*p $^3P^o_2$ based on the electric dipole selection rules, a transition is more favorable if $\Delta\ell = \Delta L = \Delta J = +1$, therefore, from the 4s5s $^3S_1$ level, the most probable transitions are 4s*n*p $^3P^o_2$. Furthermore, the 4s4p $^3P^o$ multiplet cannot be resolved in the present work due to the line width of the dye lasers $\leq 0.3\,cm^{-1}$. As the energy separation between the 4s16p $^3P^o_{0,1,2}$ fine structure multiplets is 4s16p $^3P^o_2$ – 4s16p $^3P^o_1$ is $0.4\,cm^{-1}$ and for 4s16p $^3P^o_3$ – 4s16p $^3P^o_2$ is $0.3\,cm^{-1}$ as reported by Kompitsas et al.[2] and the fine structure splitting decreases as $1/n^3$. In addition, few lines of the 4s*n*p

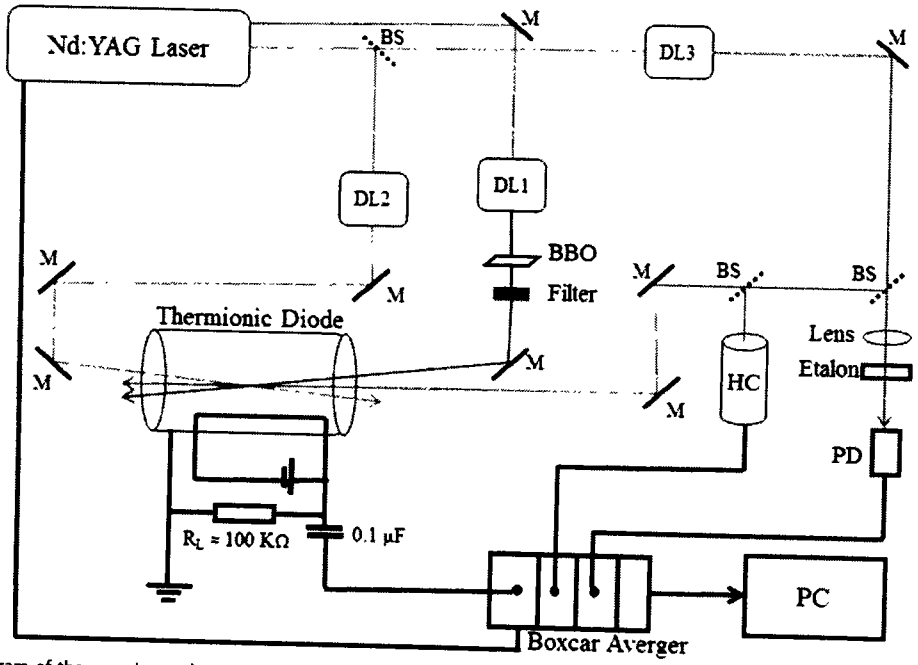

Figure 1. Schematic diagram of the experimental set-up (BS: beam splitter; DL: dye laser; M: mirror; BBO: barium borate crystal, PD: photodiode; HC: hollow cathode; PC: personal computer).

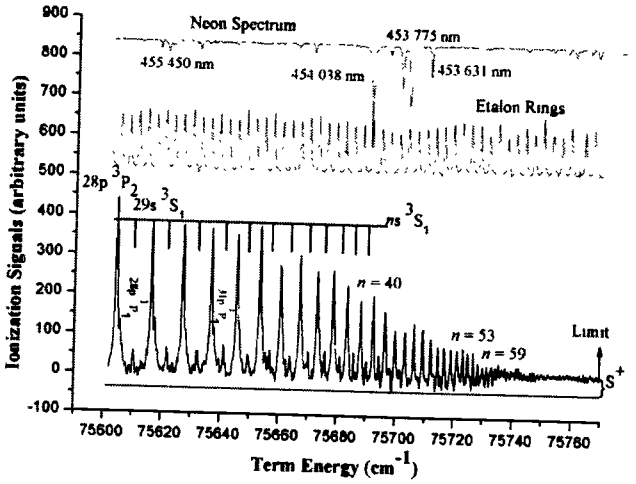

Figure 2. A portion of the zinc spectrum showing the dominant $4s5s\ ^3S_1 \rightarrow 4snp\ ^3P^o_2$ Rydberg series from $n = 28$–59. The upper trace is the reference lines of neon, the middle trace is the interference fringes from 1 mm thick solid etalon and S^+ is the ionization signal at the ionization threshold.

$^1P^o_1$ series were also identified as a shoulder to the dominating $4snp\ ^3P^o_2$ series, appearance of the $4snp\ ^1P^o_1$ series is due to the relaxation of $\Delta S = 0$ selection rule. The term energies and quantum defects of the $4snp\ ^1P^o_1$ series are in good agreement with the reported results of Brown et al.[1] up to $n = 66$. The weakest series is identified as $4sns\ ^3S_1$, the emergence of this series is due to the collisional induced angular momentum mixing or ℓ mixing induced by the bias voltage of the thermionic detector which breaks down the electric dipole selection rules $\Delta\ell = \pm 1$. The parity forbidden $4sns\ ^3S_1$ transitions were observed from $n = 29$ to 40 and after that it loses its signal intensity. Similarly, parity forbidden transitions were reported by Vidolova-Angelova et al.[28] in the spectra of cadmium. They reported the $5sns\ ^3S_1$ $(31 \leq n \leq 39)$ and $5snd\ ^3D_3$ $(17 \leq n \leq 22)$ series emerging due to the ℓ mixing from the DC Stark effect. The identification of these series were further supplemented by calculating the quantum defects using the following Rydberg relation:

$$n* = n - \delta_\ell = \sqrt{\frac{R_{Zn}}{IP - E_n}} \qquad (1)$$

where E_n are the term energies, IP is the ionization energy of zinc $75769.31 \pm 0.05\ cm^{-1}$ NIST atomic database[29] and $R_{Zn} = 109736.404\ cm^{-1}$ is the mass corrected Rydberg constant of zinc. The n, n^*, and δ_l are the principal quantum number, effective quantum number, and quantum defect, respectively. The quantum defects of the $4snp^3P^o_2$, $4snp\ ^1P^o_1$, and $5sns\ ^3S_1$ series are determined as $\delta_l = 2.198$, 2.101, and 2.715, respectively, the quantum defects are in good agreement with the previously reported work.[1,2]

Figure 3 shows the plot of principal quantum number n versus the quantum defects (δ_l) of the $4snp\ ^3P^o_2$ series. The quantum defects determined in the present work are represented as squares, triangles ($n = 10$ - 40) and circles ($n = 4$ - 9) represents the previously reported work of Kompitsas et al.[2] and Sugar and Masgrove [7], respectively. The quantum defects at lower n values are almost consistent up to $n = 40$ within reported uncertainty. However, at higher $n \geq 40$, the uncertainty in the quantum defects increases as the relative accuracy of the small energy difference $IP - E_n$ decreases for the high Rydberg states and this is represented as larger error bars in the determination of δ_l.

Finally, oscillator strengths of the dominating $4s5s\ ^3S_1 \rightarrow 4snp\ ^3P^o_2$ Rydberg transitions were determined using the technique described by Mende and Kock,[30] with the assumption that ionization probability of the transitions that lie within k_BT is unity (i.e. $\Delta E \leq k_BT$). Where, k_B is the

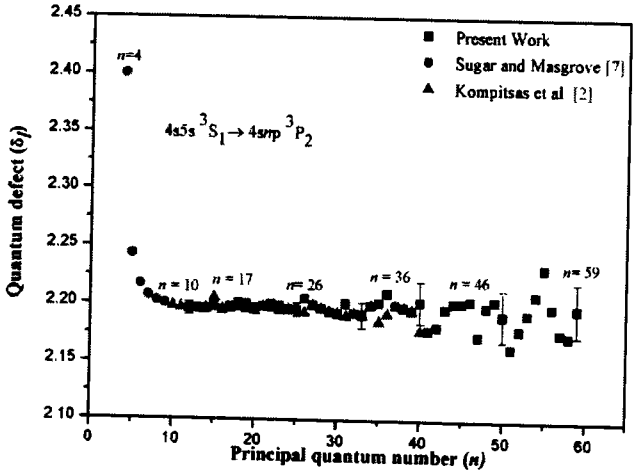

Figure 3. Quantum defect plot versus the principal quantum number n, black squares represent the present work, red circles are the results of Sugar and Masgrove [7] and the blue triangles are reported by Kompitsas et al. [2] The error bars are according to the experimental uncertainty 0.3 cm^{-1} in term energies.

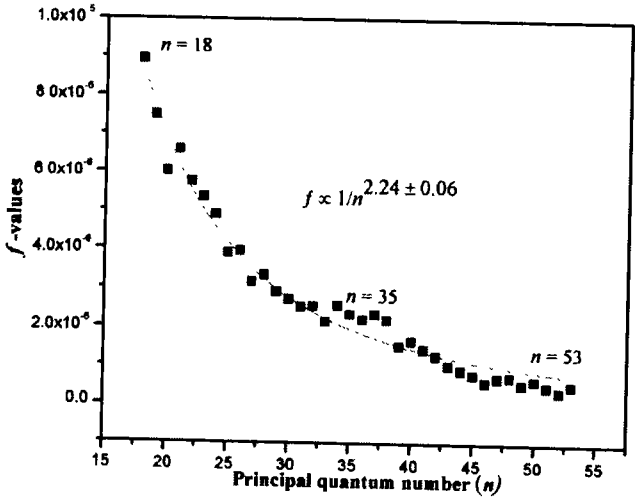

Figure 4. Oscillator strengths versus the principal quantum number n, black squares represent the oscillator strengths of the 4s5s $^3S_1 \rightarrow$ 4snp $^3P^o_2$ ($18 \leq n \leq 53$) Rydberg transitions of zinc (Zn I) and solid line is the liner fit of $f_n = K/n^m$ to the experimental data indicating a smooth decreasing as $1/n^{2.24 \pm 0.06}$ of the 4s5s $^3S_1 \rightarrow$ 4snp $^3P^o_2$ series.

Boltzmann constant, T is the temperature in Kelvin, and ΔE is the energy difference between the ionizing potential and the energy of the Rydberg level. As long as the above condition is fulfilled, the oscillator strengths of the Rydberg transitions can be determined from the following relation:[30]

$$f_n = \left(\frac{mc}{\pi}\right)\left(\frac{4\pi\varepsilon_o}{e^2}\right)\left(\frac{S^n}{S^+}\right)\left(\frac{\lambda^+}{\lambda^n}\right)\sigma(\lambda^+) \qquad (2)$$

Here, f_n is the oscillator strength of the nth transition of Rydberg series, which is directly proportional to the photoionization cross-section $\sigma(\lambda^+)$ at ionization threshold. $S^+$is the ion signal at the ionization threshold (see Fig. 2) and S^n is the integrated ion signal intensity for the nth transition at a wavelength λ^n. The integrated signal intensity is equal to the peak value times the half-width, that is S^n= signal intensity × $c\Delta k$, where c is the speed of light and Δk is the full width and half maximum of the signals (FWHM) in cm^{-1}. The constants e, m, c, and ε_o are the charge of electron, mass of the electron, speed of light, and the permittivity of free space, respectively.

Oscillator strengths of the 4s5s $^3S_1 \rightarrow$ 4snp $^3P^o_2$ Rydberg transitions from $n = 18$ to 53 have been determined using the Eq. 2. The parameters λ^n, λ^+, S^+, and S^n were extracted from the photoionization spectrum (see Fig. 2). The value of the photoionization cross-section of the 4s5s $^3S_1$ intermediate state at the first ionization threshold $\sigma(\lambda^+)$ was reported as 0.724±0.087 Mb by Liu et al.[31] computed using a close coupling R-matrix method.

The lower limit on the principal quantum number $n \geq 18$ is due to the condition that ionization probabilities of the Rydberg transitions must be unity. In the present work, the energy difference between the $n \geq 18$ states and the first ionization threshold is 439 cm^{-1}, which is clearly less than the thermal energy in the present experimental work k_BT ≈521 cm^{-1}. Therefore, it is assumed that all the transitions higher than $n \geq 18$ are thermally ionized and their ionization probabilities are assumed to be unity. In a thermionic diode ion detector, this condition can be achieved comparatively easily by optimizing the temperature and buffer gas pressures. Although in the present experimental work, we have not performed any systematic studies on the ionization probabilities of the highly excited transitions at different temperatures and buffer gas pressures. However, Niemax[32] reported the ionization probabilities of the principal series of rubidium as unity for $n \geq 25$ in a thermionic diode ion detector at ≈16 mbar. On the higher side, we have limit to the $n \leq 53$, since beyond this, it was not possible to accurately determine the integrated signal intensity and full width and half maximum (FWHM). Although the Rydberg series have been observed up to $n = 59$. In Fig. 4, oscillator strengths of the Rydberg transitions are plotted versus the principal quantum number n. The solid line is the fit of $f_n = K/n^m$ to the experimental data point indicating a smooth decreasing trend in f-values as $m = 2.24 \pm 0.06$ for the 4s5s $^3S_1 \rightarrow$ 4snp $^3P^o_2$ series. Ideally, f-values decreases as $1/n^3$, however, the lower exponent value is due to the intensity variation in the photoionization spectra, due to experimental conditions such as temperature, pressure, and pulse to pulse variation in the energy. Table 1 consists of oscillator strengths of the 4s5s $^3S_1 \rightarrow$ 4snp $^3P^o_2$ transitions, principal quantum number n, wavelengths, and term energies of the present and previous work. The error bar in the oscillator strengths are due to uncertainty in the measurement of the photoionization cross section which is ≈ 12%. Additional uncertainties are in the measurement of the signal height and width (FWHM) of the spectral lines. Therefore, the overall uncertainty in the calibration of the oscillator strength is less than 20%, for the lower $n \leq 28$ values and >25% for the higher members of the Rydberg series due to the fluctuation in the photoionization spectrum.

In order to investigate the connection between the oscillator strengths distribution in the bound region and oscillator strength density df/dE at threshold, the following relations are used[33];

Table 1. The principal quantum number n, measured wavelengths (nm), term energies (±0.3 cm^{-1}) of the $4s^np\ ^3P^o_2$ Rydberg series from $n = 18–53$ have been presented along with the previously reported term energies by Kompitsas et al.[2] from $n = 18–40$. In the fourth column measured oscillator strengths of the $4s5s\ ^3S_1 \rightarrow 4snp\ ^3P^o_2$ $(18 \leq n \leq 53)$ Rydberg transitions are listed.

n	Wavelength (nm)	Term energies (cm^{-1}) ± 0.3	Term energies (cm^{-1}) Kompitsas et al.[2]	f-values ($\times 10^{-6}$)
18	461.736	75329.7	75329.9	8.94 ± 1.79
19	460.655	75380.5	75380.7	7.48 ± 1.50
20	459.753	75423.1	75423.2	6.02 ± 1.20
21	458.997	75458.9	75458.9	6.58 ± 1.32
22	458.356	75489.4	75489.5	5.74 ± 1.15
23	457.804	75515.7	75515.8	5.35 ± 1.07
24	457.326	75538.5	75538.5	4.89 ± 0.98
25	456.913	75558.3	75558.3	3.90 ± 0.78
26	456.554	75575.5	75575.7	3.96 ± 0.79
27	456.233	75590.9	75590.9	3.16 ± 0.63
28	455.950	75604.5	75604.5	3.34 ± 0.67
29	455.699	75616.6	75616.6	2.91 ± 0.73
30	455.475	75627.4	75627.4	2.72 ± 0.68
31	455.276	75637	75637.1	2.53 ± 0.63
32	455.093	75645.8	75645.8	2.54 ± 0.64
33	454.930	75653.7	75653.7	2.15 ± 0.54
34	454.783	75660.8	75660.8	2.57 ± 0.64
35	454.648	75667.3	75667.4	2.34 ± 0.59
36	454.526	75673.2	75673.3	2.21 ± 0.55
37	454.413	75678.7	75678.7	2.34 ± 0.59
38	454.310	75683.7	75683.7	2.19 ± 0.55
39	454.215	75688.3	75688.3	1.53 ± 0.38
40	454.128	75692.5	75629.6	1.66 ± 0.42
41	454.046	75696.5		1.44 ± 0.36
42	453.971	75700.1		1.27 ± 0.32
43	453.903	75703.4		1.02 ± 0.26
44	453.840	75706.5		0.904 ± 0.23
45	453.780	75709.4		0.793 ± 0.20
46	453.724	75712.1		0.598 ± 0.15
47	453.671	75714.7		0.707 ± 0.18
48	453.623	75717		0.741 ± 0.19
49	453.578	75719.2		0.549 ± 0.14
50	453.535	75721.3		0.653 ± 0.16
51	453.494	75723.3		0.494 ± 0.12
52	453.457	75725.1		0.369 ± 0.09
53	453.422	75726.8		0.532 ± 0.13

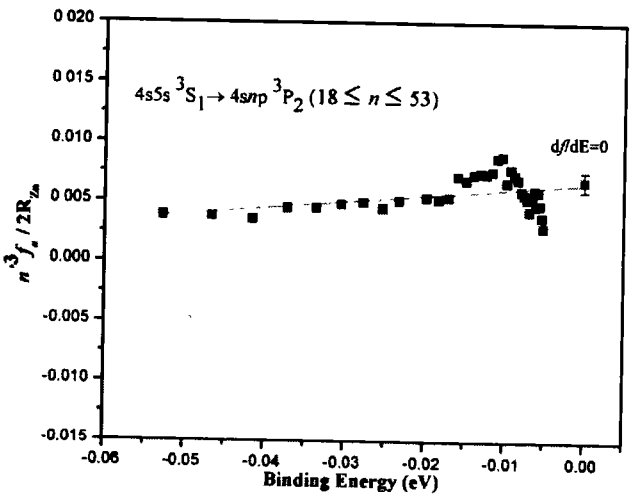

Figure 5. Plot of the $(n^{*3}f_n)/2R_{Zn}$ versus the binding energy (eV) corresponding to the $4s5s\ ^3S_1 \rightarrow 4snp\ ^3P^o_2$ $(18 \leq n \leq 53)$ transitions of zinc. Black squares represents the oscillator strength distribution in the bound region and red square is the differential oscillator strength at ionization threshold.

$$\lim_{n\to\infty} \frac{(n^*)^3}{2R_{Zn}} f_n = \left.\frac{df}{dE}\right]_{E=E_{ion}} \tag{3}$$

Here, n^* is the effective quantum number, R_{Zn} is the mass corrected Rydberg constant of zinc, and E is the binding energy. The oscillator strength density df/dE is also related with the photoionization cross-section at the threshold.[33]

$$\frac{df}{dE} = 9.11 \times 10^{15} \sigma(E) \mathrm{cm}^{-2} (\mathrm{eV})^{-1} \tag{4}$$

Figure 5 is a plot of the $(n^{*3}f_n)/2R_{Zn}$ versus the binding energy (eV). It is obvious from this figure that the oscillator strength distribution in the discrete region, corresponding to the $4s4p\ ^3S_1 \rightarrow 4snp\ ^3P^o_2$ $(18 \leq n \leq 53)$ transitions and oscillator strength density at threshold connects each other within experimental uncertainty. The oscillator strength density df/dE is calculated as 0.006/eV using the Eq. 4 by substituting the value of photoionization cross section of the $4s5s\ ^3S_1$ state at the threshold as 0.724×10^{-18} cm^2. The solid line is the linear fit to the data points indicating that the discrete oscillator strength coincides with the oscillator strength density at the threshold. However, if the f-values of the highly excited transitions beyond $n \geq 53$ are known, a connection can be confirmed at the first ionization. This continuity across the threshold is a fundamental principle of

the quantum defect theory, which originates from the continuity in the wave function across the threshold.[33]

Conclusion

Oscillator strengths for the 4s5s $^3S_1 \rightarrow$ 4s*n*p $^3P^o_2$ Rydberg transitions of zinc from $n = 18$ to 53 have been determined. A good agreement between the discrete *f*-values and the oscillator strengths distribution at threshold has been established to verify the fundamental condition of quantum defect theory which satisfies the continuity of the wavefunctions across the threshold. These studies provide useful information in various fields of science, such as astrophysics, plasma physics, radiation physics, in the dynamics of stellar atmosphere for the determination of atomic abundance and it is also important in thermonuclear research.

Acknowledgments

We are thankful to the Pakistan Atomic Energy Commission (PAEC) for the technical support. We are also very grateful to the Prof. Dr. Zeng Jiaolong and Dr. Yanpeng Liu from National University of Defense Technology (Changsha, China) for providing the data files of the photo-ionization cross section.

References

[1] Brown, C. M.; Tilford, S. G.; Ginter, M. L. Absorption Spectra of Zn I and Cd I in the 1300–1750 Å Region. *Journal of Optical Society of America* **1975**, *65*, 1404–1409. DOI: 10.1364/JOSA.65.001404

[2] Kompitsas, M.; Baharis, C.; Pan, Z. Rydberg States of Zinc and Measurement of the Dipole Polarizability of the Zn^+ Ion. *Journal of Optical Society of America B* **1994**, *11*, 697–702. DOI: 10.1364/JOSAB.11.000697

[3] Nawaz, M.; Nadeem, A.; Bhatti, S. A.; Baig, M. A. Two-Step Laser Excitation of 4s*n*d $^3D_{1,2,3}$ and 4s*n*s $^3S_1$states from the 4s4p ^3P Levels in Zinc. *Journal of Physics B: Atomic and Molecular Optical Physics.* **2006**, *39*, 871–881. DOI: 10.1088/0953-4075/39/4/011

[4] Nadeem, A.; Nawaz, M.; Bhatti, S. A.; Baig, M. A. Multi-Step Laser Excitation of the Highly Excited States of Zinc. *Optics Communications* **2006**, *259*, 834–839. DOI: 10.1016/j.optcom.2005.08.075

[5] Shah, M.; Aisha, G.; Shahzada, S.; Haq, S. U.; Nadeem, A. Step-Wise Laser Excitation of the 4s*n*f ^3F Rydberg States of Neutral Zinc. *Spectroscopy Letters* **2018**, *51*, 1–6.

[6] Gullberg, D.; Litzen, U. Accurately Measured Wavelengths of Zn I and Zn II Lines of Astrophysical Interest. *Physica Scripta* **2000**, *61*, 652–656. DOI: 10.1238/Physica.Regular.061a00652

[7] Sugar, J.; Musgrove, A. Energy Levels of Zinc. Zn I through Zn XXX. *Journal of Physical and Chemical Reference Data* **1995**, *24*, 1803–1872. DOI: 10.1063/1.555971

[8] Curtis, L. J. Precision Oscillator Strength and Lifetime Measurements. In *Handbook Springer of Atomic, Molecular, and Optical Physics*; Drake, G. W. F., Ed; AIP Press: New York, **2005**, 262–268.

[9] Huber, M. C. E.; Sandeman, R. J. The Measurement of Oscillator Strengths. *Reports on Progress in Physics.* **1986**, *49*, 397–490. DOI: 10.1088/0034-4885/49/4/002

[10] Richter, J. Measurements of Lifetimes and Oscillator Strengths of Neutral and Singly Ionized Atoms. Experimental Results of the Last Five Years. *Physica Scripta* **1984**, *T8*, 70–76. DOI: 10.1088/0031-8949/1984/T8/011

[11] Kerkhoff, H.; Schmidt, M.; Zimmermann, P. Lifetimes and Oscillator Strengths in the Triplet System of Zn I. *Zeitschrift für Physik* **1980**, *298*, 249–252. DOI: 10.1007/BF01425154

[12] Ueda, K.; Iimura, H.; Karasawa, M.; Fukuda, K. Measurement of Oscillator Strengths for Three Lines among the 4s4p $^3P^o$- 4p^2 ^3P Multiplet of Zn I. *Journal of the Physical Society of Japan* **1981**, *50*, 3545–3546. DOI: 10.1143/JPSJ.50.3545

[13] Ueda, K.; Karasawa, M.; Fukuda, K. Absorption and Dispersion Studies of the 4s4p $^3P^o$-4p^2 ^3P Multiplet of Zn I. *Journal of the Physical Society of Japan.* **1982**, *51*, 1941–1947. DOI: 10.1143/JPSJ.51.1941

[14] Afanaseva, N. V. Calculation of Oscillator Strengths of the Principal Series of Zinc by the Two-Channel Quantum Defect Method. *Optics and Spectroscopy* **1982**, *52*, 776–780.

[15] Afanaseva, N. V. Oscillator Strengths of Atomic Zn 4p $^1P^0_1 \rightarrow$ 4s*n*d $^1D_2$ Transitions. *Optics and Spectroscopy* **1985**, *59*, 475–476.

[16] Haq, S. U.; Nadeem, A.; Nawaz, M.; Baig, M. A. Oscillator Strength Measurements of the Highly Excited 4s4d$^3P_1 \rightarrow$ 4s*n*d $^3D_2$ Transtions of Zinc. *Journal of the Optical Society of America B* **2010**, *27*, 402–407. DOI: 10.1364/JOSAB.27.000402

[17] Warner, B. Atomic Oscillator Strengths IV Transitions of the Type $s^2 \rightarrow$ sp and ss $\rightarrow$ sp. *Monthly Notices of the Royal Astronomical Society* **1968**, *140*, 53–59. DOI: 10.1093/mnras/140.1.53

[18] Zilitis, V. A. Oscillator Strengths for Resonance Lines of Atoms of the Group II Elements. *Optics and Spectroscopy* **1974**, *36*, 630–634.

[19] Luc-Koenig, E. Relativistic Effects on Transition Probabilities $^3P^o_1 \rightarrow {}^1S_0$ for group-II Elements. *Journal of Physics B: Atomic and Molecular Physics* **1974**, *7*, 1052–1058. DOI: 10.1088/0022-3700/7/9/016

[20] Glowacki, L.; Migdalek, J. Relativistic Configuration-Interaction Oscillator Strength Calculations with ab Initio Model Potential Wave Functions. *Journal of Physics B: Atomic, Molecular and Optical Physics.* **2003**, *36*, 3629–3636. DOI: 10.1088/0953-4075/36/17/306

[21] Glowacki, L.; Migdalek, J. Relativistic Configuration–Interaction Oscillator Strengths Calculations with *ab Initio* Screened Model-Potential Wave Functions. *Journal of Physics B: Atomic and Molecular Physics* **2006**, *39*, 1721–1729.

[22] Brage, T.; Fischer, C. F. Core Polarization Effects on Oscillator Strengths in Neutral Zinc. *Physica Scripta* **1992**, *45*, 43–48. DOI: 10.1088/0031-8949/45/1/007

[23] Chen, M. H.; Cheng, K. T. A Large-Scale Relativistic Configuration-Interaction Approach: application to the 4s^2 – 4s4p Transition Energies and E1 Rates for Zn-like Ions. *Journal of Physics B: Atomic, Molecular and Optical Physics* **2010**, *43*, 074019. DOI: 10.1088/0953-4075/43/7/074019

[24] Hanna, D. C.; Kärkkäinen, P. A.; Wyatt, R. A Simple Beam Expander for Frequency Narrowing of Dye Lasers. *Optiucal and Quantum Electronics* **1975**, *7*, 115–119. DOI: 10.1007/BF00631592

[25] Martinson, I.; Curtis, L. J.; Huldt, S.; Litzén, U.; Liljeby, L.; Mannervik, S.; Jelenkovic, B. Lifetimes for Low-Lying Levels in Zn I and Zn II. *Physica Scripta* **1979**, *19*, 17–21. DOI: 10.1088/0031-8949/19/1/004

[26] Liang, L.; Zhou, C. Radiative Lifetimes of Zn I Highly Excited States. *Journal of Quantitative Spectroscopy and Radiative Transfer* **2008**, *109*, 1995–1999. DOI: 10.1016/j.jqsrt.2008.01.022

[27] Niemax, K. Spectroscopy Using Thermionic Diode Detectors. *Applied Physics B* **1985**, *38*, 147–157. DOI: 10.1007/BF00697477

[28] Vidolova-Angelova, E.; Baharis, C.; Roupakas, G.; Kompitsas, M. Observations and Theoretical Analysis of Highly Excited Singlet and Triplet States of Cadmium. *Journal of Physics B: Atomic, Molecular and Optical Physics* **1996**, *29*, 2453–2472. DOI: 10.1088/0953-4075/29/12/010

[29] Ralchenko, K. A.; Reader, Y. J; NIST ASD Team. NIST Atomic Spectra Database (Ver. 5,5.6), [Online], National Institute of

Standards and Technology, Gaithersburg, MD. **2018**. https://physics.nist.gov/asd [accessed May 24, 2018].

[30] Mende, W.; Kock, M. Oscillators Strengths of Ba I and Sr I Rydberg Transitions. *Journal of Physics B: Atomic, Molecular and Optical Physics* **1996**, *29*, 655–663. DOI: 10.1088/0953-4075/29/4/008

[31] Liu, Y. P.; Gao, C.; Zeng, J. L.; Shi, J. R. Atomic Data of Zn I for the Investigation of Element Abundances. *Astronomy & Astrophysics*. **2011**, *536*, A51. DOI: 10.1051/0004-6361/201117348

[32] Niemax, K. Investigation on the Thermionic Diode: The Ionization Probability of Rb n^2P_J Atoms by Noble Gas Collisions. *Applied Physics B* **1983**, *32*, 59–62. DOI: 10.1007/BF00688544

[33] Connerade, J. P. *Highly Excited Atoms*; Cambridge University Press: New York, **1998**.